2019

I3: Isomerization of Isomer Ions

Krisztián Gabor Torma
University of the Pacific, krisz.torma@gmail.com

Recommended Citation

Torma, Krisztián Gabor. (2019). *I3: Isomerization of Isomer Ions*. University of the Pacific, Dissertation.
https://scholarlycommons.pacific.edu/uop_etds/3649

I^3: ISOMERIZATION OF ISOMER IONS

By

Krisztián Gábor Torma

A Dissertation Submitted to the

Graduate School

In Partial Fulfillment of the

Requirements for the Degree of

DOCTOR OF PHILOSOPHY

Thomas J. Long School of Pharmacy and Health Sciences
Pharmaceutical and Chemical Sciences

University of the Pacific
Stockton, California

2019

I^3: ISOMERIZATION OF ISOMER IONS

By

Krisztián Gábor Torma

APPROVED BY:

Dissertation Advisor: Bálint Sztáray, Ph.D.

Committee Member: Skylar Carlson, Ph.D.

Committee Member: Liang Xue, Ph.D.

Committee Member: Joseph Harrison, Ph.D.

Committee Member: Kieran Holland, Ph.D.

Department Co-Chair: Jianhua Ren, Ph.D.

Department Co-Chair: Jerry Tsai, Ph.D.

I^3: ISOMERIZATION OF ISOMER IONS

By

Krisztián Gábor Torma

DEDICATION

This dissertation is dedicated to my amazing girlfriend, Krisztina. I am inspired by the hard work and dedication you apply to your career every day. The patience you have shown, as I have worked through my studies, has given me the confidence to move forward believing in myself with each and every step. Without your endless support I could not have done this.

ACKNOWLEDGEMENTS

I have deep gratitude for the many people who have helped me in this journey. First and foremost, I would like to thank Professor Bálint Sztáray, my research advisor, for his immense support, guidance, and encouragement during my time at UoP. His advice and counsel have been instrumental in the completion of my studies.

I want to thank our postdocs, Dr. Krisztina Voronova and Dr. Amelia Ray, and my labmates Chrissa Mozaffari-Easter, Kyle Covert, Peter Weidner, and Jessica De La Cruz. Not only for their help and valuable discussion, but also for their friendship. They are as helpful and as good of friends as anyone could ask for. I'm grateful to have gone through my graduate studies with them.

I will forever be thankful to Dr. Andras Bodi for his scientific advice, knowledge, and many insightful discussions and suggestions. He allowed me to spend my internship at the Swiss Light Source, which coincidentally but significantly sped up the publication of my first project. I am grateful for Dr. Patrick Hemberger for his help with our measurements at the SLS.

I would also like to thank Dr. Skylar Carlson, Dr. Liang Xue, Dr. Joseph Harrison, and Dr. Kieran Holland for agreeing to serve on my dissertation committee. They have been nothing but supportive during my preparation.

I would like to extend special thanks to Susan McCann and Faith Keith for their help on the administrative side of things. This department would not be able to run without them.

I want to thank to the members of the Chemistry Department faculty who offered insight, and feedback on my research. Finally, I am grateful for my family and friends who've been patient, understanding, and accommodating during my dissertation journey.

I^3: ISOMERIZATION OF ISOMER IONS

Abstract

By Krisztián Gábor Torma

University of the Pacific
2019

Photoelectron Photoion Coincidence (PEPICO) spectroscopy is a robust tool for elucidating complex unimolecular dissociation mechanisms and for determining thermochemical and kinetic data of gas-phase ion dissociations with high accuracy. In this work, the dissociative photoionization of two sets of isomeric systems were analyzed with PEPICO: 1) $C_7H_7^+$ ions of toluene (Tol) and 1,3,5-cycloheptatriene (CHT), and 2) two butyl alcohol isomers, 1-butanol and isobutanol. Threshold dissociative photoionization data on these four molecules of interest were collected on the imaging PEPICO apparatus at the VUV beamline of the Swiss Light Source. Data analysis was aided by *ab initio* calculations and Rice-Ramsperger-Kassel-Marcus (RRKM) statistical rate theory was employed to model the complex dissociation pathways of each system. Finally, thermochemical, reaction mechanism, and dissociation kinetics data were extracted from the modeled data and are reported here.

In the first project, the dissociation of energy-selected 1,3,5-cycloheptatriene (CHT) and toluene (Tol) cations was investigated by imaging photoelectron photoion coincidence spectroscopy. In the measured energy ranges of 10.30−11.75 eV for CHT and 11.45−12.55 eV for Tol, only the hydrogen atom loss channels open up, leading to $C_7H_7^+$ from both molecular ions, which are both metastable at the H-loss threshold. Our quantum chemical calculations showed that these ions can interconvert below their dissociation thresholds. Therefore, we

constructed a single statistical model to describe both systems simultaneously. We determined 0 K appearance energies (E_0) for the tropylium and benzyl fragment ions from CHT to be 9.520 ± 0.060 eV and 9.738 ± 0.082 eV, and from Tol to be 10.978 ± 0.063 eV and 11.196 ± 0.080 eV, respectively. Using the experimentally determined benzyl ion appearance energy, its 0 K heat of formation was calculated to be 937.9 ± 7.7 kJ mol^{-1}. On the basis of this value and the recently determined benzyl ionization energy, we point out discrepancies concerning the benzyl radical thermochemistry.

For the second project, the fragmentation processes of two internal energy-selected $C_4H_{10}O^{+\bullet}$ cations, 1-butanol and isobutanol, were investigated. For both isomers, the first dissociation channel leads to the formation of $C_4H_8^{+\bullet}$ ions (*m/z* = 56) by a water loss. Using statistical energy distribution and rate models, which include isomerization of the molecular ions, the 0 K appearance energies (E_0) were determined to be 10.347 ± 0.015 eV and 10.566 ± 0.050 eV, for 1-butanol and isobutanol, respectively. The second dissociation channel, the formation of $CH_3OH_2^+$, quickly overtakes the water-loss channel in isobutanol, with an E_0 of 10.612 ± 0.020 eV, but appears only as a minor channel in 1-butanol with an E_0 of 10.738 ± 0.080 eV. The methanol-loss channel, forming propylene ion, opens up at E_0 = 10.942 ± 0.040 eV and 10.723 ± 0.020 eV in 1-butanol and isobutanol, respectively. The next two fragmentation pathways correspond to a complementary pair of $C_3H_7^+$ through the loss of CH_2OH, and CH_2OH^+ through the loss of C_3H_7. From both isomers, $C_3H_7^+$ is the isopropyl ion, which is readily formed in isobutanol *via* a simple bond cleavage at E_0 = 10.970 ± 0.050 eV and its pair, CH_2OH^+, at E_0 = 11.11 ± 0.20 eV. However, there is an internal hydrogen shift necessary in 1-butanol and, therefore, the complementary ions appear at the same E_0 of 11.104 ± 0.030 eV, which most likely corresponds to their common transition state. Finally, $C_3H_5^+$, a product of sequential dissociation from *m/z* = 56, appears above 11.6 eV as a minor channel for both isomers.

TABLE OF CONTENTS

LIST OF TABLES

Table

LIST OF FIGURES

Figure

LIST OF SCHEMES

Scheme

LIST OF ABBREVIATIONS

AIE	Adiabatic Ionization Energy
ATcT	Active Thermochemical Tables
B3LYP	Becke–3-parameter–Lee–Yang–Parr exchange-correlation functional
BDE	Bond Dissociation Energy
Bz^+	Benzyl ion
CBS	Complete Basis Set method
CCSD	Coupled Cluster Single-Double method
CHT	1,3,5-cycloheptatriene
CRF-PEPICO	Combustion Reaction Followed by Photoelectron Photoion Coincidence Spectroscopy
DFT	Density Functional Theory
FWHM	Full Width at Half Maximum
iPEPICO	imaging Photoelectron Photoion Coincidence Spectroscopy
IRC	Intrinsic Reaction Coordinate
IVR	Internal Vibrational energy Redistribution
KE	Kinetic Energy
KIE	Kinetic Isotope Effect
MCP	MicroChannel Plate detector
MM	Multiple-start/Mulitple-stop data acquisition
ms-TPES	mass-selected Threshold PhotoElectron Spectrum
PEPICO	Photoelectron Photoion Coincidence Spectroscopy
PES	PhotoElectron Spectroscopy or Potential Energy Surface

PI	PhotoIonization
PIE	PhotoIonization Efficiency
PIMS	PhotoIonization Mass Spectrometry
PST	Phase Space Theory
QCISD	Quadratic Configuration Interaction Size-Consistency method
QET	Quasi-Equilibrium Theory
RRKM	Rice–Ramsperger–Kassel–Marcus theory
SM	Single-start/Mulitple-stop data acquisition
SS	Single-start/Single-stop data acquisition
SSACM	Simplified Statistical Adiabatic Channel Model
STQN	Transit-Guided Quasi-Newton method
TOF	Time-of-Flight
Tol	Toluene
TPEPICO	Threshold Photoelectron Photoion Coincidence Spectroscopy
TPES	Threshold PhotoElectron Spectrum
Tr^+	Tropylium ion
TS	Transition State
VMI	Velocity Map Imaging
VUV	Vacuum UltraViolet radiation

CHAPTER 1: INTRODUCTION

Photoelectron Photoion Coincidence Spectroscopy (PEPICO) is a robust tool to elucidate complex dissociation mechanisms and to determine thermochemical and kinetics data with high accuracy by inducing the unimolecular dissociation of gas phase cations. Although decades of research, both experimental and theoretical, has provided some understanding of the dissociation mechanism of both the butanol and C_7H_8 isomer systems,[1-8] insights into their respective fragmentation processes still remain elusive. Recent improvements to statistical thermodynamics modeling and game-changing instrumental upgrades to the PEPICO technique, spearheaded by our research group – including improvements to electron and ion optics and the use of a high intensity synchrotron light source – has motived us to revisit these projects and offer additional insight. As such, this thesis is divided into two main projects: 1) the dissociative photoionization of toluene (Tol) and 1,3,5-cycloheptatriene (CHT), and 2) a comparison of the dissociative photoionization of 1-butanol and isobutanol.

For the first project, hydrogen abstraction from gaseous 1,3,5-cycloheptatriene (CHT) and toluene (Tol) cations ($C_7H_8^+$ isomers) leads to the formation of two almost isoenergetic $C_7H_7^+$ isomers: benzyl (Bz^+) and tropylium (Tr^+). The driving forces guiding the reactive flux to the benzyl or the tropylium cation and their rearrangement reaction holds unanswered questions even after 60 years of research.[9-16] The iPEPICO setup allows for accurate energy selection of the photoions. This experimental data (the fractional ion abundance plotted as a function of the photon energy) is customarily represented in the breakdown diagram, which then modeled together with the dissociation rate information extracted from the time-of-flight (TOF) mass spectra, using statistical rate theories. Our goal was to use careful modeling of energy distributions and dissociation rates to construct a single statistical model which describes hydrogen abstraction from both CHT and Tol cations. We uncovered evidence for the coexisting H-loss channels and explored the isomerization processes as well as large kinetic and competitive shifts.

The aim of the second project presented here is to advance our understanding of statistical rate and energy distribution theories, and to determine highly accurate experimental thermodynamic data on neutral and ionic species related to combustion and atmospheric processes. Alcohols are the most prominent biofuels to date, with ethanol already being used as a fuel additive. Butanol isomers, and 1-butanol in particular, have better mixing with common fuels, and better compatibility with traditional engines. Hence, the second project involves the study of fragmentation processes of two internal energy selected $C_4H_{10}O^+$ cations, 1-butanol and isobutanol.

Interestingly, both butanol isomer cations produce six fragment ions with same mass-to-charge ratios (*m/z*), but widely different branching ratios, by numerous parallel and consecutive dissociation channels in a narrow, 3 eV photon energy range. Although many of these species and elementary reactions involved have been fairly well characterized, thermochemical input parameters are one of the major sources of uncertainty in the combustion models. Hence, to understand the reaction mechanisms and to obtain reliable energetics data, the breakdown diagrams of 1-butanol and isobutanol cations were modeled using statistical energy distributions and rate theory. The interpretation and analysis of these fairly complex dissociation mechanisms were aided by high-level quantum chemical calculations. The accurate determination of energetics data of these small oxygenated species supports the ever-increasing need to improve the accuracy of predictive combustion models.

CHAPTER 2: THEORY AND TECHNIQUES

2.1. Photoelectron Photoion Coincidence Spectroscopy (PEPICO)

2.1.1. Background and Applications

Photoelectron photoion coincidence spectroscopy is the combination of photoionization mass spectrometry (PIMS) and photoelectron spectroscopy (PES). Monochromatic vacuum ultraviolet (VUV) light is used to irradiate a sample in gas phase that, if the absorbed photon had sufficient energy, causes the ejection of an electron:

$$\mathrm{AB} + h\upsilon \rightarrow \mathrm{AB}^+ + \mathrm{e}^- \rightarrow \mathrm{A}^+ + \mathrm{B} + \mathrm{e}^- \tag{1}$$

where AB is a neutral molecule, $h\upsilon$ represents the absorbed photon, AB^+ is the formed ion, and e^- is the ejected electron.[17] Then, if AB^+ has enough internal energy, it might dissociate into a fragment ion A^+ and a neutral leaving group B. The photoions are mass analyzed in a time-of-flight (TOF) mass analyzer, where the start signal is provided by the electron (*vide infra*). In the early years of PEPICO, a monochromatic VUV light source was used to ionize a neutral sample (e.g. He, Ne), but later light sources were implemented that provided a broadband VUV light. The most common type was the hydrogen gas discharge lamp connected to a VUV monochromator to filter out the unwanted wavelengths.[18-20] With this setup, dissociation reactions of the photoion as a function of its internal energy can be studied by varying the photon energy. To know the exact internal energy of the formed ion, the kinetic energy of the corresponding electron must be determined. The energetics of an ionization process can be given as:

$$E_\mathrm{i} = h\upsilon + E_\mathrm{thermal} + KE_\mathrm{e^-} + KE_\mathrm{i} - AIE \tag{2}$$

where E_i is the internal energy of the ion, $h\upsilon$ is the photon energy, $E_{thermal}$ is the thermal energy of the neutral molecule, KE_{e^-} and KE_i are the kinetic energies of the electron and the ion, respectively, and AIE is the adiabatic ionization energy. Because of momentum conservation, KE_i is close to zero and can be omitted from the equation. Threshold PEPICO (TPEPICO) is a technique where only the zero kinetic energy electrons are considered.[21-28] Therefore, the energy of the photon is entirely partitioned into the internal energy of the ion and equation (2) above can be simplified for TPEPICO as:

$$E_i = h\upsilon + E_{thermal} - AIE \qquad (3)$$

The AIE is known, $h\upsilon$ is controlled by the monochromator, the thermal energy of the neutral can be modeled (knowing the sample temperature) and, therefore, the internal energy of the ion is well-defined.

As mentioned earlier, the photoions in a PEPICO experiment are mass analyzed in a Wiley-McLaren time-of-flight setup and the undissociated molecular ion AB^+ (see Eq. 2) and fragment ion A^+ are separated by their time-of-flight. If the dissociation is slow, then unimolecular rate constants can also be extracted from the mass spectra by fitting the quasi-exponential shape of the metastable fragment ion peak. The fractional abundances of the ions as a function of photon energy is plotted in a breakdown diagram to derive 0 K appearance energies (E_0) of the fragment ions. The 0 K heat of formation of the neutral molecule, the fragment ion, and the neutral fragment is connected through a thermochemical cycle with E_0 where:

$$E_0 = \Delta_f H^{\circ}_{0\,K}[A^+] + \Delta_f H^{\circ}_{0\,K}[B] - \Delta_f H^{\circ}_{0\,K}[AB] \qquad (4)$$

If the 0 K heats of formation of two species are known, then the $\Delta_f H^{\circ}_{0\,K}$ of the third can be calculated utilizing the experimental E_0. The PEPICO technique can also be employed to investigate both sequential and parallel dissociations.[29]

Experiments presented herein on the dissociative photoionization of toluene, 1,3,5-cycloheptatriene, 1-butanol, and isobutanol were carried out on the imaging PEPICO instrument at the Swiss Light Source of Paul Scherrer Intitut in Switzerland.

2.1.2. Imaging PEPICO Apparatus at the Swiss Light Source

As it has been mentioned in the previous section, a tunable VUV light source with high photon flux is necessary for TPEPICO measurements in order to ionize and fragment neutral molecules. Briefly, tunable synchrotron radiation is produced when electrons moving at close to the speed of light are forced to change trajectory by a bending magnet, wiggler, or undulator. Unlike bending magnets, wigglers and undulators are periodic structures of alternating dipole magnets, so electrons traveling through them are forced to oscillate. Every oscillation produces VUV radiation, therefore wigglers and undulators provide more intense light in a narrow energy range.[30] Bending magnets generate a broad spectrum of wavelengths, therefore a grazing-incidence grating monochromator is used at the VUV beamline of the Swiss Light Source to filter out unwanted photon energies. Gratings with 300, 600, and 1200 mm^{-1} line density can be selected, depending on the energy resolution and the photon intensity required. Measurements can be carried out in the 5–21 eV photon energy range with a photon flux of 10^{12}–10^{14} s^{-1}. Ideal resolving power using the 600 mm^{-1} grating is $\Delta E/E \approx 10^{-4}$, corresponding to 1 meV resolution at 10 eV. The ionization rate therefore easily surpasses the commonly used hydrogen discharge lamp, at which point the coincidence data acquisition normally would be impossible due to the high count rates.[31] Utilizing a multiple-start/multiple-stop data acquisition scheme (*see Chapter 2.1.4.*) ionization event rates of over 100 kHz can be recorded with correlating all electron and ion signals. Electron counts and positions and ion counts are recorded with a time to digital converter card in triggerless mode, allowing the multiple-start/multiple-stop acquisition scheme.[32]

The collimated synchrotron radiation beam is focused onto a vertical slit in the 0.8 m long gas filter, located 26 m from the light source, which has eight differentially pumped chambers. To filter out higher harmonics a low-pressure mixture of noble gases can be introduced to the sixth chamber of the gas filter. Typically, a 3:1 ratio of Ne:Ar or pure Neon is used at around 10 mbar pressure below 15.759 eV or below 21.565 eV photon energies, respectively. If a measurement is done under 10 eV, a MgF_2 window can be inserted in front of the gas filter that absorbs nearly all light above 11 eV. The photon energy is calibrated using the first and second order Ar 11 s' – 14 s' autoionization lines.[33]

Samples can be introduced into the spectrometer *via* an effusive inlet or through a molecular beam. For samples with low volatility, a heated inlet may be used. The gas phase sample is intersected and ionized by the monochromatic VUV synchrotron radiation. Photoelectrons and photoions are accelerated to opposite directions with a constant 40–120 V cm^{-1} electric field. The electron flight tube is 265 mm long with a 20 mm wide opening to velocity map image the beam at a Roentdek DLD40 position sensitive delay-line detector.[34-36] The kinetic energy resolution is better than 1 meV at threshold. Upon ionization, photoions first enter a 5.5 cm long first extraction region, then a 1 cm long second acceleration region, then a 55 cm long drift region before space-focused onto a Jordan TOF C-726 microchannel plate detector.

2.1.3. The "hot electron" problem

Historically, PEPICO has suffered from the so-called "hot electron" contamination. This term is used for energetic electrons that have a non-zero kinetic energy. If electron initial velocity vectors are in the direction of the detector, then “hot” electrons are detected together with the threshold electrons. Therefore, by partitioning some of the available photon energy into the photoelectron instead, an ion will have less internal energy and may not dissociate at photon energies where, in theory, it would have enough energy to do so. Therefore, the relative abundance of an ion approaches zero more gradually and at a higher than expected photon energy. This phenomenon is also referred to as the hot electron tail in a breakdown diagram.

There have been several attempts to reduce and/or eliminate the contribution of hot electrons. Tsai *et al.*[37] used a Wiley-McLaren TOF setup to extract electrons from the ionization region in a pulsed fashion at 3 MHz frequency and 1 V extraction field. The electron detector was set to accept only a narrow range of signals that corresponded to electrons with zero kinetic energy. This approach also eliminates hot electrons with in-plane kinetic momentum. The technique is not in use anymore as (1) it made it difficult to extract kinetic information from the data, and (2) it required to obtain a randomly triggered ion TOF spectrum to eliminate the contribution from false coincidences, making data acquisitions complicated. King *et al.*[38] used a different approach and put a cylindrical cage around the ionization region which was responsible for extracting electrons with a weak penetrating field. Electrons with about 3 meV or less kinetic energy were extracted and focused onto the exit hole of the cylinder, while hot electrons drifted to the walls. Unfortunately, only using a weak field caused the broadening of the TOF peaks, hence significantly reducing the mass resolution of the spectrometer.

Both of the aforementioned techniques used low electric fields to extract only near zero kinetic energy electrons. Chandler and Houston[39] developed a versatile ion imaging technique in a form of velocity map imaging (VMI). They utilized a simple aperture lens to disperse charged particles with all energies by their velocity perpendicular to the axis of extraction. These particles were focused onto and detected on imaging plates. Particles with similar kinetic energy were detected as rings around the center spot. The radii of these rings are proportional to the initial velocities perpendicular to the extraction axis. Baer and Li[40] were the first ones to implement VMI in a PEPICO spectrometer. Although hot electrons are greatly reduced by this technique they are not eliminated completely as electrons with a kinetic energy vector parallel with the extraction axis will be detected in the center spot along with the near zero kinetic energy electrons. Sztáray and Baer[41] resolved this issue by using multichannel plate detectors with two separate anodes. One anode is responsible for collecting only hot electrons (ring), whereas the other anode detected both threshold electrons and hot electrons (center). Subtracting the former from the latter, while scaling for differences in area, a pure threshold spectrum can be obtained. In the modern implementation, the use of imaging detectors allows the user to select the size and position of the center and ring to be optimized for best resolution. In practice, this method works because all hot electrons (above a certain kinetic energy) contribute to a small portion of the center signal, resulting in a close to uniform unstructured hot electron signal over the entire detector, even near the center where the threshold electron signal is. By sampling the hot electron signal around the center, the contamination can be subtracted from the center while accounting for the difference in the center and ring areas with factor *F*:

$$F \cong \frac{r_1^2}{r_2^2 - r_1^2} \tag{5}$$

where r_1 and r_2 are the radii of the center and the ring, respectively. Since the electron count rate is far from infinite, the calculated *F* factor is just an approximation and usually needs to be slightly adjusted to completely account for the total hot electron contamination.

2.1.4. Coincidence Statistics

As discussed in the previous chapter, every ionization event in PEPICO creates an electron and an ion, unless there is unwanted electron emission from the surface of the instrument caused by photons. Depending on the photon energy, photoelectron yield, and the electron resolution, the threshold electron collection efficiency can be anything between 0.01 and 100%. The electron and ion signals can be defined by the total ionization rate, N, assuming that the collected electrons and ions are from the identical volume in the ionization region:

$$N_e = \eta_e N \quad (6) \quad and \quad N_i = \eta_i N \quad (7)$$

where η_e and η_i are the collection efficiencies for the electrons and the ions, respectively. The number coincidences, N_c, can be expressed in two ways: (1) using the ion rate, N_i, and electron collection efficiency: $N_c = \eta_e N_i$; or (2) using the electron rate, N_e, and ion efficiency: $N_c = \eta_i N_e$. From these equations the electron and ion collection efficiencies can be given in terms of observed count rates:

$$\eta_e = \frac{N_c}{N_i} \quad (8) \quad and \quad \eta_i = \frac{N_c}{N_e} \quad (9)$$

Above threshold energies imaging plates or microchannel plate detectors (MCP) can be used to determine the electron collection efficiency. Determining η_e and η_i are valuable for diagnostic purposes and are used to optimize the performance of the spectrometer.

Electron and ion collection efficiencies are negatively impacted by coincidence statistics due to the presence of false coincidences. If the ionization rate is low, then events are well separated.[42] Therefore, using a single-start/single-stop (SS) detection scheme is sufficient where the detection of an electron provides the start signal for the TOF measurement and the detection of its ion is the stop signal. With increasing ionization rates, more and more events will overlap.

Therefore, true coincidence events are missed when a false ion stops the time measurement before the true event can be detected. A single-start/multi-stop (SM) configuration reacts to one start signal but detects multiple stop signals within a user selected time-frame. However, the main drawback of this approach that new start signals are lost within the set time window, which introduces artifacts into the ratio of coincidences and the false coincidence background. Therefore, this approach is not ideal with sources providing high ionization rates such as synchrotron radiation. Multi-start/multi-stop (MM) coincidence detection correlates all electron and ion signals, which are time stamped relative to a master clock.[32] False coincidences provide a flat background (with random noise on top of this) throughout the entire TOF spectra, whereas true coincidences appear as peaks on top of the background.

The signal-to-noise ratio (*S*/*N*) from the false coincidence background for a coincidence peak with a peak width of *w* can be given as:

$$\frac{S}{N} = r\sqrt{\frac{\eta_e \eta_i \tau}{w}} \tag{10}$$

where r is the fractional intensity of the peak, and τ is the collection time. The signal-to-noise ratio for true coincidences is defined as:

$$\frac{S}{N} = \sqrt{rN\eta_e \eta_i \tau} \tag{11}$$

It is evident from the equations above that the false coincidence contribution as noise to a coincidence peak is independent of *N*, whereas for a true coincidence peak the *S*/*N* ratio increases with the square root of *N*. Hence, it is wise to work with high photon fluxes. Having narrow peak widths, long collection times, and high electron and ion collection efficiencies will also boost the signal-to-noise ratio.

2.2. Combustion Reaction Followed by PEPICO

Herein, a brief overview is provided on the Combustion Reactions Followed by PEPICO (CRF-PEPICO) instrument. This project was a complex collaboration between multiple research groups located in the United States and Europe. Our research group led in designing and building the instrument, but a handful other scientists contributed to individual parts of the project. As part of my dissertation work, I took part in the construction and testing of the prototype CRF-PEPICO instrument at the VUV beamline of the Swiss Light Source in Switzerland. I built the ion and electron optics and installed it in the vacuum chamber. Together with other research groups and the beamline personnel, we put together the rest of the components to test the apparatus and, eventually, conduct our first experiments. First, these testing included energizing the ion–electron optics for the first time and optimizing the voltages to maximize electron and ion collection efficiencies as well as the energy and spatial resolutions. Then, we performed the first kinetic experiments with a flow tube reactor and laser in place, outlined in more details below. Although none of the projects in this dissertation were run on the CRF-PEPICO instrument, I have spent a significant amount of time on building, calibrating, and using this prototype over the span of several beamtimes.

As discussed earlier in this chapter, PEPICO is the combination of PIMS and PES. PIMS with tunable VUV radiation is extensively used to investigate reactive intermediates relevant in atmospheric and combustion chemistry at the Chemical Dynamics Beamline of the Advance Light Source (ALS).[43-48] PIMS is a universal analytical technique, which is sensitive and selective in a large dynamic range ($\sim 10^5$). It is a powerful tool for rapid resolution of a mixture of neutral species first by ion mass-to-charge (m/z) ratio using mass spectra, and second by photoionization (PI) spectrum within each m/z channel. The onset and shape of the PI spectrum is a spectral fingerprint used to distinguish different neutral isomers observed at the same parent *m*/*z* ratio. However, a more detailed spectral fingerprint can be measured with photoelectron spectroscopy, in which for each neutral species, the photoelectron intensity vs. electron binding energy yields the photoelectron (PE) spectrum. In contrast to the step-like thresholds that may be present in a PI spectrum, each quantum state of the photoion creates a peak in the photoelectron spectrum. Even similar isomers often yield distinct vibrational progressions. The lack of mass selection, however, renders it useless in analyzing complex mixtures as the resulting photoelectron spectrum is the sum of every neutral spectrum.

Since PEPICO analyzes and detects both the photoelectron and the photoion, it can record a photoelectron spectrum in which the photoelectrons were detected in coincidence with a certain photoion, essentially ion-mass slicing the otherwise much too complex photoelectron spectrum of a complex mixture. To test this idea, just before I joined, our research group carried out proof-of-concept experiments using the existing iPEPICO setup to analyze two separate static mixtures. One of them was 2-butyne and 1,3-butadiene, and the other one contained an additional four C_5H_8 isomers (1-pentyne; 1,4-pentadiene; cyclopentane; isoprene). Both TPES and mass selected TPES (ms-TPES) were plotted and are shown in Figure 1. The former contains the total threshold photoelectron signal regardless of the neutral molecule source, whereas the latter is selected for a specific ion time-of-flight window.

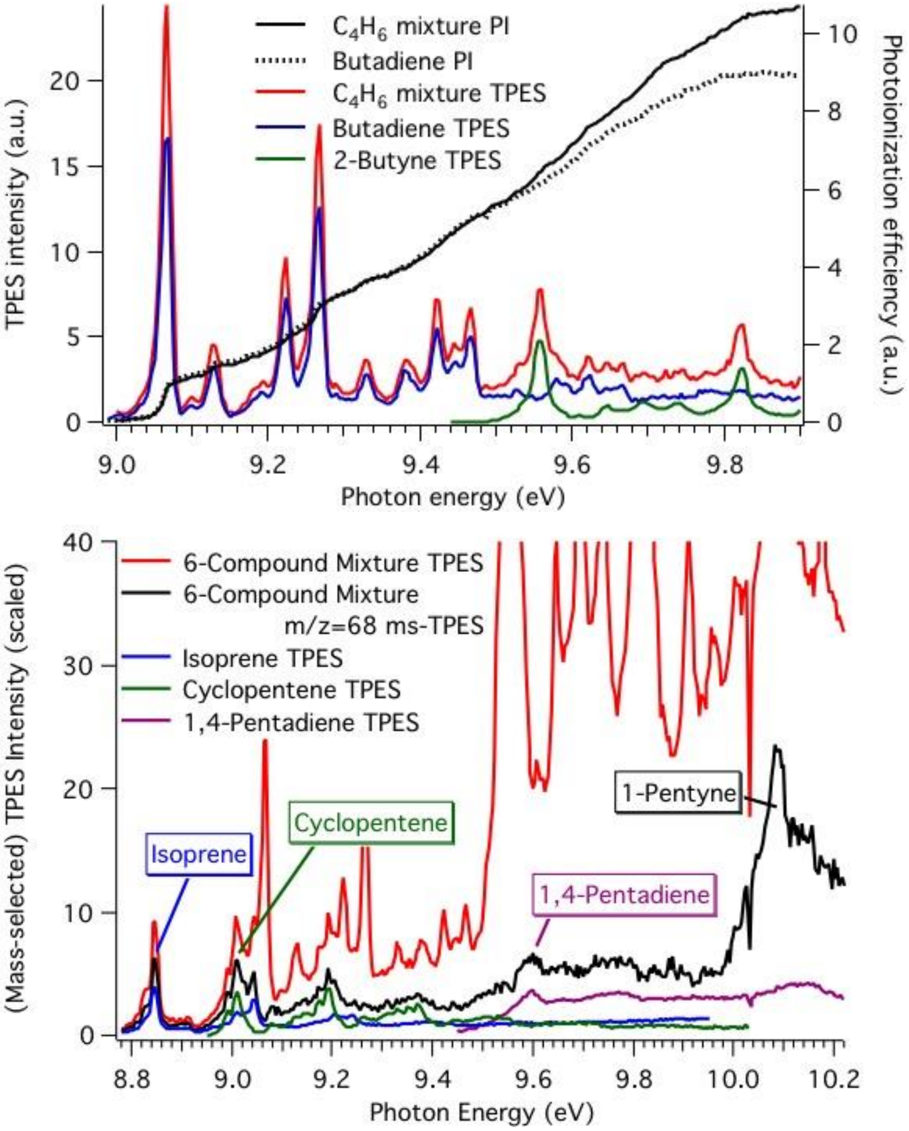

Figure 1. Threshold photoelectron spectrum of 2-butyne and 1,3-butadiene mixture and the individual components. The PI curves of the latter compound and the mixture is also shown for comparison (upper). Total and mass selected TPES are shown along with the TPES of four individual components (lower).

The top figure of Figure 1 shows the TPES and ms-TPES along with the PI curves of the first mixture containing ~95% 1,3-butadiene and ~5% 2-butyne. Although the PI spectrum (solid black line) detects the presence of 2-butyne in the mixture, its identification is more definitive with TPES. The bottom figure shows the TPES and ms-TPES for the more complex mixture.

The mass selection allows the separation of *m/z* = 68 and 54 signals, where the two *m/z* = 54 ions can be easily identified. The first peak in the ms-TPES of *m/z* = 68 isomers is from isoprene, which is closely followed by cyclopentane, only separated from the second peak of isoprene by 40 meV. The first peak of 1,4-pentadiene appears around 9.6 eV, then the strong first peak of 1-pentyne is detected at 10.08 eV. Based on these proof-of-concept experiments it is evident that the ms-TPES contains information superior to the thresholds observed in PI spectra for multi-component mixtures. Therefore, PEPICO could be employed to study reactive intermediates important in atmospheric and combustion chemistry and the prototype CRF-PEPICO experiment was built in collaboration between our group, the Swiss Light Source, and Sandia National Laboratory, for the SLS VUV beamline.

To understand the motivation behind building this new prototype instrument, first we need to recall what a good analytical technique is. The ideal analytical experiment is:

- universal: applicable to a broad spectrum of samples
- sensitive: detects intermediates with short lifetimes and/or concentrations
- selective: able to clearly identify similar species
- multiplexed: accomplishes every goal above simultaneously.

Of these criteria, PEPICO obviously fulfills most: any small molecule can be photoionized (universal), combining mass spectrometry and photoelectron spectroscopy offers unparalleled selectivity and, due to the continuous nature of coincidence detection, all species are detected at the same time (multiplexed). However, the sensitivity of PEPICO needed to be addressed.

As we discussed in previous chapters, PEPICO has overcome some major challenges in the past decades. One of the latest ones were the issue of signal paralysis at high count rates, which enabled its use with synchrotron radiation sources. False coincidences create a constant background in the TOF mass spectrum at high ionization rates with random noise around the average background value. Although the average false coincidence background can be subtracted from the spectrum, the random noise on this background still obscures minor peaks and limits the dynamic range to ~10^3. This poses a major issue in the detection of species in trace amounts. To solve this, ion deflection is used by applying a periodically changing electric field. The electric field is user controlled and is therefore known, so the detection position of an ion can be predicted at every nanosecond. The measured and predicted ion impact positions only agree for true coincidences, which allow the almost complete removal of false coincidences from the data set. Consequently, the dynamic range is also increased by 2-3 orders of magnitude. When cold argon clusters are ionized, false coincidence suppression allows the observation of species up to Ar_9^+, while Ar_4^+ is the largest observable cluster under traditional operation (Figure 2).

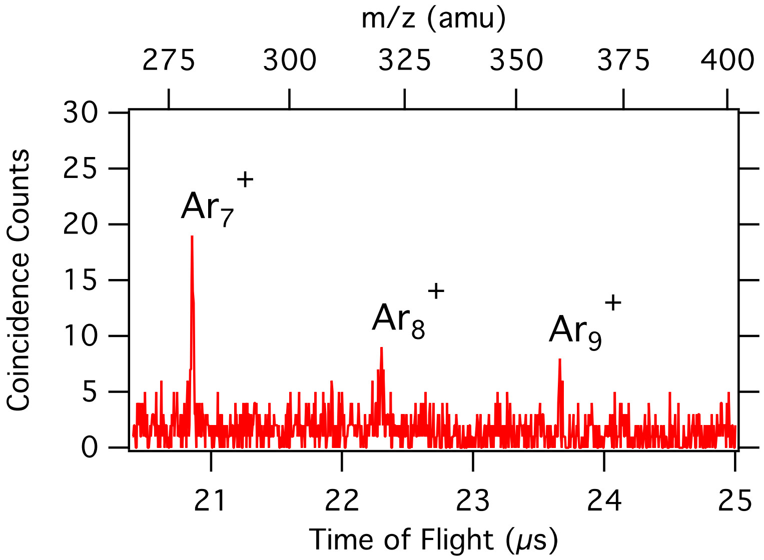

Figure 2. False-coincidence suppressed time-of-flight coincidence spectrum of the larger argon oligomer ions.

Eliminating false coincidences breaks down the major barrier to utilizing PEPICO as a sensitive and versatile analytical technique, offering photoelectron spectral fingerprints of even very minor and transient components of a time-evolving, reactive mixture.

The CRF-PEPICO design considerations included (1) tight ion focusing with a mass resolving power of at least 400–500, (2) high electron KE resolution and high multiplexing, (3) high sensitivity, and (4) to keep most of the existing setup. The sample introduction happens through a side-sampled, quartz flow tube reactor inlet, which, to achieve high sensitivity, is placed as close to the ionization spot as possible. Therefore, the ion and electron optics were designed to contain the flow tube. In order to maximize the adaptability of the ion and electron optics, 12 individually controlled electrode plates are used on the electron side and 14 on the ion side. Therefore, the length of the extraction and acceleration regions can be varied without the need to vent the instrument. Every plate has a 24 mm inner and 90 mm outer diameter with 0.5 mm thickness. The spacing between plates is 6.25 mm except for the last seven plates of the ion side, where it is increased to 9.00 mm. The total length of the optics is 75.5 and 105.7 mm on the electron and ion sides, respectively. The first plates on both sides were cut by 26 mm from their edge to house the flow tube. The electron flight tube is a 62 mm I.D. μ-metal cylinder that is field free. The ion flight tube has a 60 mm I.D. that holds the ion deflector used for false coincidence rejection. The electron and ion detectors are located at 750 and 1000 mm from the ionization point.

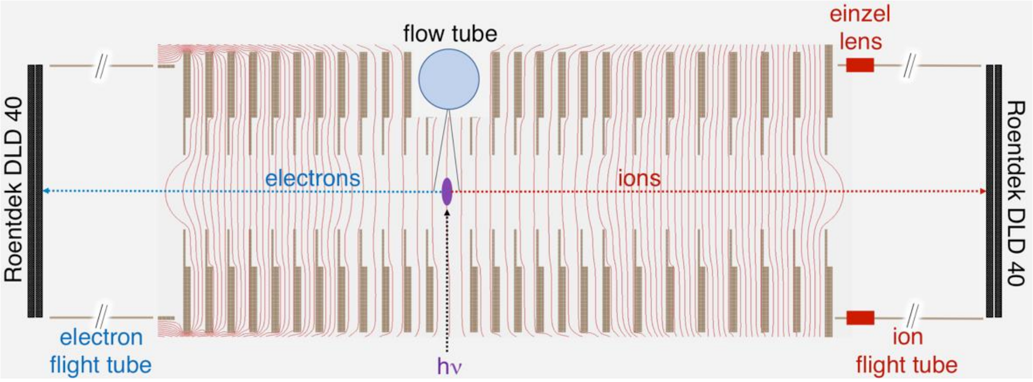

Figure 3. Section view of the CRF-PEPICO along the center line of the electrode plates with calculated equipotential lines.

The quartz flow tube is 57.4 cm long with 1.05 cm inner and 1.27 cm outer diameter. The gas flow is controlled by mass flow controllers and is mixed at the entrance of the flow tube in a glass yoke attachment. There is a 200–400 μm pinhole at the halfway point along the tube, which allows side-sampling and to control the pressure. The gas mixture reaches the ionization region through the pinhole, while the pressure in the instrument is kept below 6 x 10^{-6} mbar without the need of differential pumping. In early experiments a 20 Hz pulsed Nd-YAG laser beam was guided through the flow tube at 355 or 266 nm to create free radicals, which was replaced by a newer 10 Hz laser with higher pulse energy. The flow rate in the tube is sufficient to completely replace the gas mixture with a fresh sample between laser shots. The pressure inside the tube is kept low to avoid bimolecular reactions and the inside of the tube is coated with halocarbon wax to minimize radical loss on the wall. The distance between the pinhole and the ionization point is variable between 17–25 mm.

To test the capabilities of the CRF-PEPICO instrument, argon was introduced through a molecular beam and intersected by the synchrotron radiation at 16 eV. The mass resolving power was measured to be 780 and the ion spot on the detector had a 0.7–0.8 mm FWHM.

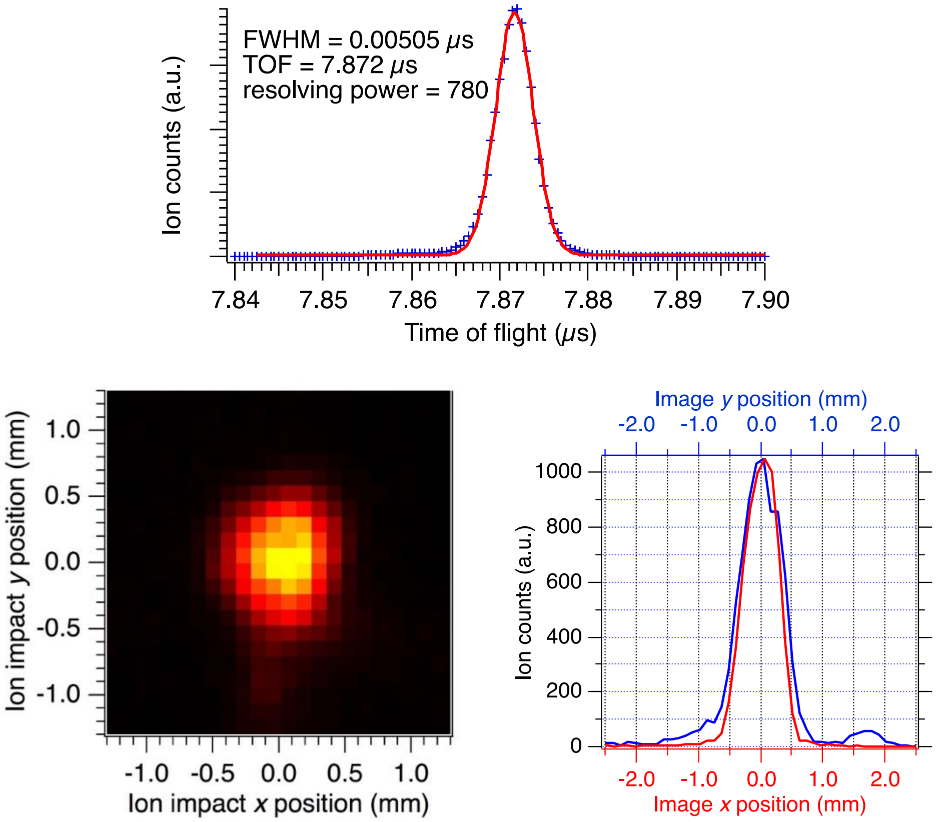

Figure 4. Argon TOF mass spectrum (top) and ion image using the molecular beam inlet (bottom left). The cross section of the ion spot shows typical FWHMs (bottom right).

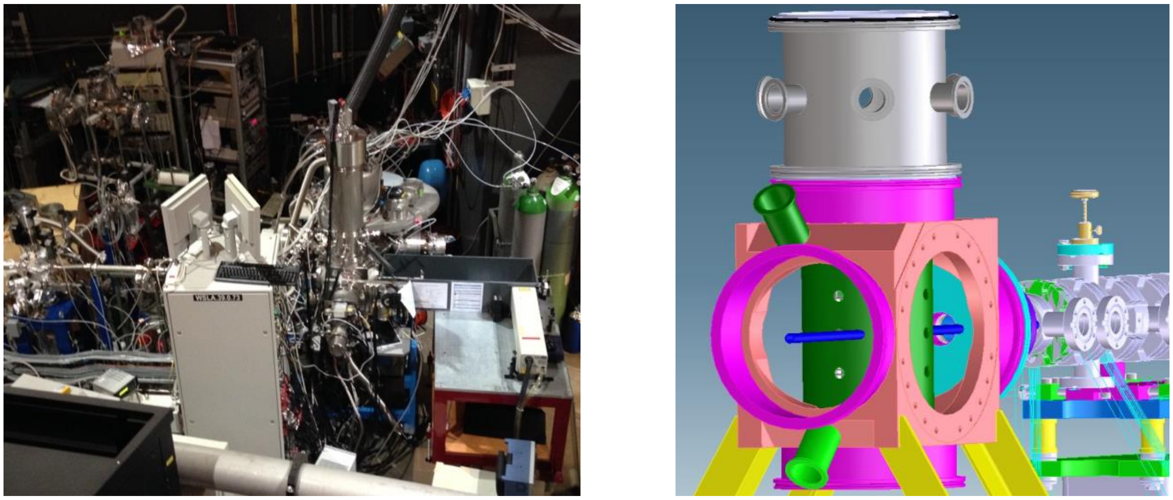

Figure 5. On the left: aerial view of the CRF-PEPICO setup at the SLS. The ion flight tube points up, the synchrotron beam enters from the left and the Nd-YAG laser in on the table on the right. On the right: CRF-PEPICO experimental setup. The μ-metal shielding cylinder around the charged particle optics colored in green and the flow tube in blue.

Aerial view of the setup on the left in Figure 5 shows the 1 m long ion flight tube pointing up, the synchrotron beam entering from the left and the Nd-YAG laser on the table on the right. The isometric view of the CRF-PEPICO experimental setup including the gas filter can be seen on the right. The colored chamber is part of the original iPEPICO setup. As it was mentioned before, the CRF-PEPICO experiment consists of a quartz flow tube, where a Nd-YAG laser photolytically generated radicals react with target molecules. A small portion of the gas-mixture exists the tube through a pinhole half-way down the tube and the plume of gases is intersected by the synchrotron photon beam in the center of the ionization region, creating photoelectrons and photoions that are analyzed in a double-imaging PEPICO scheme.

The first CRF-PEPICO experiments started in October, 2014 and the first successful flow-tube PEPICO data was recorded in March, 2015. In the first successful kinetic time resolved PEPICO experiments, CH_2I radical formation and its reaction with molecular oxygen were studied with the CRF-PEPICO setup. In short, the reaction was initiated by photolysis of CH_2I_2 at 355 nm, producing CH_2I radicals and I atoms using argon as a buffer gas. Decay of the CH_2I radical as function of O_2 concentration was monitored at 9.19 eV in time-resolved measurements (Figure 6).

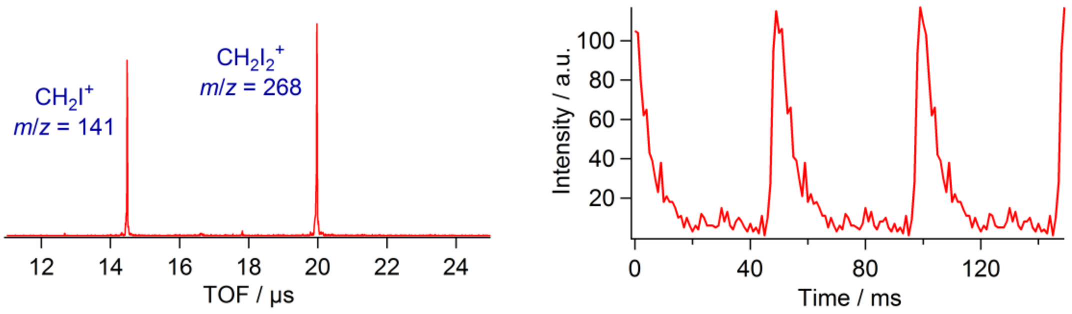

Figure 6. TOF mass spectra of the photolytically generated $CH_2I^\bullet$ can be seen on the left. On the right is the first time-resolved PEPICO signal showing the depletion of the $CH_2I^\bullet$ radical with 2.430×10^{14} cm^{-3} O_2.

Since its successful test, the CRF-PEPICO setup has been used to measure the TPES of the propargyl, CH_2I, and CH_3OO radicals and to investigate the reaction kinetics of iodomethyl radical,[49] allyl radical,[50] and methyl peroxy radical[51] with molecular oxygen.

2.3. PEPICO Data Analysis

As briefly discussed in previous chapters, ionic bond dissociation energies can be extracted from experimental PEPICO measurements but that requires detailed modeling of the dissociation processes. In the following section, we will explore the necessity of modeling, as well as present the underlying theories and their applications to the PEPICO experiments.

2.3.1. Measuring Unimolecular Reactions

The low pressure inside the PEPICO chamber (3–5 × 10^{-6} torr) provides approximately 5 to 10 m long mean free path for a small molecule with a diameter of about 5 Å at room temperature. The length of the acceleration region and the flight tube combined is significantly shorter (about 0.5 m), therefore only unimolecular reactions can take place between photoionization and detection. In this case, a single ion can either isomerize into another ion or dissociate into two or more products. Unimolecular reactions are often first-order reactions, meaning the reaction proceeds at a rate that depends linearly on one reactant concentration. In the case of a unimolecular decay, where the reaction species (A) dissociates into products (P), the change in concentration of A over time can be given by the following equation:

$$-\frac{d[A]}{dt} = k\,[A] \tag{12}$$

or in integral form:

$$[A] = [A]_0 e^{-kt} \tag{13}$$

where $[A]_0$ is the initial concentration of the reaction species A, $[A]$ is the concentration at a given time (t), and k is the unimolecular rate constant. The temperature dependence of the rate constant can be measured in the canonical ensemble.[52] The internal energy distribution of the canonical ensemble, $P(E,T)$, connects the canonical rate constant, $k(T)$, to the microcanonical rate constant, $k(E)$ by the following equation:

$$k(T) = \int_{E_0}^{\infty} P(E,T)k(E)dE \tag{14}$$

In this equation, E_0 is the activation energy showing that no reaction can occur till the internal energy exceeds this threshold value. E_0 corresponds to the dissociation bond energy for barrierless dissociation reactions, whereas it is the barrier height for reactions with real barriers. In TPEPICO measurements, the energy distribution of the parent ions formed upon ionization cannot be described with a single temperature value. Furthermore, energy distribution amongst the products of the photodissociation has to be considered for both parallel and consecutive reactions. Therefore, the internal energy distribution of the reactant has to be defined along with the microcanonical rate constant at every photon energy. In the case of a fast dissociation, E_0 corresponds to the energy, where the abundance of the parent ion reaches zero or near the onsets of parallel dissociations. In many cases the first appearance of a product shifts to higher photon energies because the time for the parent ion to fully dissociate is larger than the time-frame of the experiment. The excess energy required to observe dissociation is called kinetic shift.[53-54] For this reason, PEPICO is not suitable to determine rate constants below 10^3 s^{-1}.[55-56] Another phenomenon, called thermal shift, also had to be taken into account during the modeling process in the early days of PEPICO data analysis.[53,57] The non-zero thermal energy of the sample caused the observed appearance energy to shift to lower value. The elimination of the hot electron contamination from the threshold signal coincidentally solved the issue of thermal shift. In the case of competing parallel dissociation channels, an increased E_0 for the slower dissociation channel may be present due to a competitive shift from the lower energy channel.[58] By fitting the measured part of the $k(E)$ to the unimolecular rate theory and then extrapolating it over several orders of magnitude, E_0 can be determined correctly and accurately.

2.3.2. Rice-Ramsperger-Kassel-Marcus (RRKM) Theory

The purpose of a kinetic model is to describe the energy dependence of the rate constant with a minimal number of well-defined parameters that, ideally, can be measured experimentally. Since solving the time-dependent Schrödinger equation is close to impossible for even the smallest systems, some assumptions had to be made. Hinshelwood[52] was amongst the first to successfully explain the observed first-order kinetics of many unimolecular reactions. He proposed a mechanism that consists of a second-order bimolecular collisional activation step, followed by a rate-determining unimolecular step.

$$A + M \underset{k_{-1}}{\overset{k_1}{\rightleftharpoons}} A^* + M$$

$$A^* \overset{k_2}{\rightarrow} P$$

Hinshelwood described a system where *A* molecule consist of *s* number of equivalent harmonic oscillators with an energy of *hυ*. The number of ways to distribute a given number of quanta, *n*, among the *s* oscillators [i.e. the number of degenerate states at (*n* + ½)*hυ* energy]:

$$g_n = \frac{(n+s-1)!}{n!\,(s-1)!} \tag{15}$$

The Boltzmann distribution can be used to calculate the fraction of species in state *n*:

$$p_n = \frac{g_n e^{-nh\upsilon/_{kT}}}{\left(\dfrac{1}{1-e^{-h\upsilon/_{kT}}}\right)^3} \tag{16}$$

where *k* is the Boltzmann constant, and *T* is the temperature.

In this model, energy change between harmonic oscillators is forbidden, therefore it is transferred only by collisions. Because the collisions promote equilibrium, the probability of forming a state *n* in a collision is given by the Boltzmann distribution. The total rate of activation is described by the collision frequency (*Z*) and the critical energy (E_0):

$$k = \frac{Z}{(s-1)!}\left(\frac{E_0}{kT}\right)^{s-1} e^{-E_0/_{kT}} \tag{17}$$

The flaw in the model is that the unimolecular step fails to consider that a unimolecular reaction specifically involves one particular form of molecular motion. Rice, Ramsperger,[59-60] and Kassel[61] recognized that the shortcoming of Hinshelwood-mechanism can be addressed when a minimum amount of energy is localized in specific modes of molecular motion in order for the unimolecular step to take place. They introduced a new step to the mechanism, where the generally excited molecule is converted into an "activated complex" before forming the products. This conversion became the rate determining step.

$$A^* \xrightarrow{k_{2a}} A^\ddagger \xrightarrow{k^\ddagger} P$$

RRK theory assumes that energy can flow freely from one vibrational mode to another within the molecule, which is a reasonable assumption, since molecular vibrations are highly anharmonic at high energies and therefore are coupled. The probability, P_n^m, of locating at least *m* quanta out of *n* in the dissociation mode is

$$P_n^m = \frac{(n-m+s-1)!\,n!}{(n-m)!\,(n+s-1)!} \tag{18}$$

If the quantum numbers involved are very large ($n - m >> s$), then using $E = nh\upsilon$ and $E_0 = mh\upsilon$, the equation above can be written as

$$P_{E_0}^E = \left(1 - \frac{E_0}{E}\right)^{s-1} \tag{19}$$

where $P_{E_0}^E$ is the probability of locating the minimum energy E_0 in the dissociation mode out of the total energy of *E*. If the vibrational energy is distributed statistically then the rate constant can be given as

$$k = k^\ddagger \left(1 - \frac{E_0}{E}\right)^{s-1} \tag{20}$$

The RRK theory matches well with experimental observations showing that the rate constant rapidly decreases as the molecule becomes more complex but it is incapable of providing accurate rate constants. This is due to the fact that in most cases $n - m$ is not significantly larger than *s*.[62]

RRK theory was corrected by Marcus and Rice[63] (1951) and later by Rosenstock, Wahrhaftig, and Eyring[64] (1952). They realized that the vibrational and rotational degrees of freedom need to be explicitly treated. The new theory is now known in the literature as RRKM or QET (Quasi-Equilibrium Theory). The phase space of a molecule with m degrees of freedom can be described by the motion of m momentum (p) and m positions (q). The dimensionality of the phase space of a microcanonical system is $2m–1$. If the energy of the molecule, E, is greater than the minimum energy of the unimolecular reaction, E_0, then reactants and products are connected by a critical surface (transition state) with a dimensionality of $2m–2$. Once the trajectory of the system passes through the critical surface it cannot return. For reactions with distinct energy maximum along the reaction coordinate, the critical surface is usually located at the saddle point. Let’s assume that the reaction coordinate is perpendicular to the critical surface and that the phase space is populated statistically. By labeling the momentum and position coordinates of the critical surface as $p^‡$ and $q^‡$, respectively, the ratio of molecules near the critical region to the total molecules can be expressed as:

$$\frac{dN(q^‡,p^‡)}{N} = \frac{dq^‡dp^‡ \int_{H=E-\varepsilon_t-E_0} \int dq_1^‡ \cdots dq_{n-1}^‡ dp_1^‡ \cdots dp_{n-1}^‡}{\int_{H=E} \int dq_1 \cdots dq_n dp_1 \cdots dp_n} \tag{21}$$

where ε_t is the translational energy associated with momentum $p^‡$ in the reaction coordinate. The rate of the reaction is the time derivative of the number of molecules near the critical surface. Using the reduced mass of the separating fragments, $\mu^‡$, we have $dq^‡/dt = p^‡/\mu^‡$, and $d\varepsilon_t = p^‡dp^‡/\mu^‡$:

$$\frac{dN(q^‡,p^‡)}{dt} = \frac{Nd\varepsilon_t \int_{H=E-\varepsilon_t-E_0} \int dq_1^‡ \cdots dq_{n-1}^‡ dp_1^‡ \cdots dp_{n-1}^‡}{\int_{H=E} \int dq_1 \cdots dq_n dp_1 \cdots dp_n} \tag{22}$$

By dividing the equation above with the total number of molecules (N) we get the rate constant. The integration in the numerator equals to $\rho^{\ddagger}(E - \varepsilon_t - E_0)h^{n-1}$, whereas the denominator is $\rho(E)h^n$, where ρ is the density of states. Therefore, the rate constant can be given as a function of kinetic energy along the reaction coordinate and the energy of the system:

$$k(E, \varepsilon_t) = \sigma \frac{\rho^{\ddagger}(E - \varepsilon_t - E_0)}{h\rho(E)} \tag{23}$$

The symmetry factor (σ) is used to take the symmetry of the phase space into account. Integration over ε_t provides the microcanonical rate constant:

$$k(E) = \sigma \frac{N^{\ddagger}(E - E_0)}{h\rho(E)} \tag{24}$$

where $N^{\ddagger}$ is the sum of states at the transition state.

RRKM theory is based on three major assumptions that in part contradict each other. First, the intramolecular vibrational redistribution[65] (IVR) among different quantum states of the vibrationally excited molecule must be faster than the reaction. On the other hand, it was assumed that the reaction coordinate is separated from the other coordinates, which means that there is no energy change between these on the time scale of the experiment. The vibrational number and density of states is calculated using the harmonic oscillator model, which by nature does not permit IVR. Second, it assumes the existence of a critical surface which divides the reactants from the products, while being a one-time crossing. Trajectory simulations on small molecules showed that this assumption is often not valid.[66] However, the relative size of the phase space compared to the critical surface is rapidly increasing with larger molecular sizes, which means that this assumption probably holds for large molecules.[67] Third, assuming the separation of $dp^{\ddagger}$ and $dq^{\ddagger}$ from the other coordinates based on the fact that they are perpendicular to the rest. In cases where the vibrational modes can be treated as independent modes, e.g. reactions with distinct saddle points and at low energies, this assumption is valid.

Despite the aforementioned assumptions RRKM theory can be used to successfully model the kinetics of unimolecular reactions. One significant advantage of the RRKM model to trajectory simulations is that it requires less prior knowledge on the system of interest but still capable of providing reliable results.

2.3.3. Simplified Statistical Adiabatic Channel Model (SSACM)

SSACM[68-69] is a variation of the Phase Space Theory (PST),[70-72] which treats the transitional modes as free rotors. PST, and therefore SSACM as well, are limited to reactions that either do not involve a transition state or said transition state is very loose. The consequence of this limitation is that the potential energy surface of the reaction is not important in determining the unimolecular rate constant. PST has a strict restriction on the conservation of angular momentum and energy and assumes that the decomposition of the activated complex depends on the phase space available to each product. The equation of unimolecular rate constant shows some resemblance to the RRKM equation but noticeably missing the concept of the transition state. Another interesting difference is that although both equations contain densities of states but in PST it is refers to the initial molecule and products, not the transition state. If the true E_0 is implemented, PST tends to overestimate the reaction rates at high energies as it contains only a single variable, the E_0. SSACM introduces an additional adjustable energy dependent function, which prevents the rate constant to rise too rapidly as the internal energy is increasing. This is called rigidity factor, which reflects the anisotropy of the potential and, in addition, the subtle interplay between the anisotropic and attractive properties of the potential.[73]

The formula of the rigidity factor is dependent on the dissociation. If the dissociation involves mostly valence forces at short ranges therefore being strongly anisotropic, and relatively weak ion-induced dipole forces at long ranges, so being nearly isotropic, it is formulated as

$$f_{rigid}(E) = e^{-\left(\frac{E-E_0}{c}\right)} \tag{25}$$

This changing anisotropy character is generally associated with ionic fragmentation. In the case, e.g. dissociation of an ion and a permanent dipole this latter term is anisotropic, therefore the rigidity factor has to be modified.

$$f_{rigid}(E) = \left[1 + \left(\frac{E - E_0}{c}\right)^2\right]^{-\frac{2}{3}} \tag{26}$$

In both cases *c* is the fitting parameter, which shows the relative importance of the aforementioned long range forces comparatively to the short range ones. Despite the inclusion of the rigidity factor, SSACM eventually overestimates the rate constant at high energies but nevertheless it provides a useful upper limit to it.

2.3.4. Experimental Breakdown Diagram

TPEPICO measurement data are a collection of TOF spectra at varying photon energies. Integrating peaks in those spectra provide breakdown curves, which are fractional ion abundances plotted versus the photon energy. As the photon energy increases, the energy distribution is shifted to higher energies, thereby leading to more dissociation. Finally, when the photon energy equals the appearance energy of the fragment ion, E_0, the whole distribution is above the dissociation limit, and the ratio of the parent ion goes to zero.

TOF spectra are also used to gain direct kinetic information. Asymmetric fragment ion peaks are indicative of slow dissociations, where the rate constants are in the range of 10^3 s^{-1} < $k(E)$ < 10^7 s^{-1}. Conditions, such as threshold ionization cross sections, sample pressure, and photon intensity have no effect on the breakdown diagram, making it superior over a photoelectron spectrum (PES) or a photoionization efficiency (PIE) curve. The process of modeling a breakdown diagram is summarized in Figure 7.

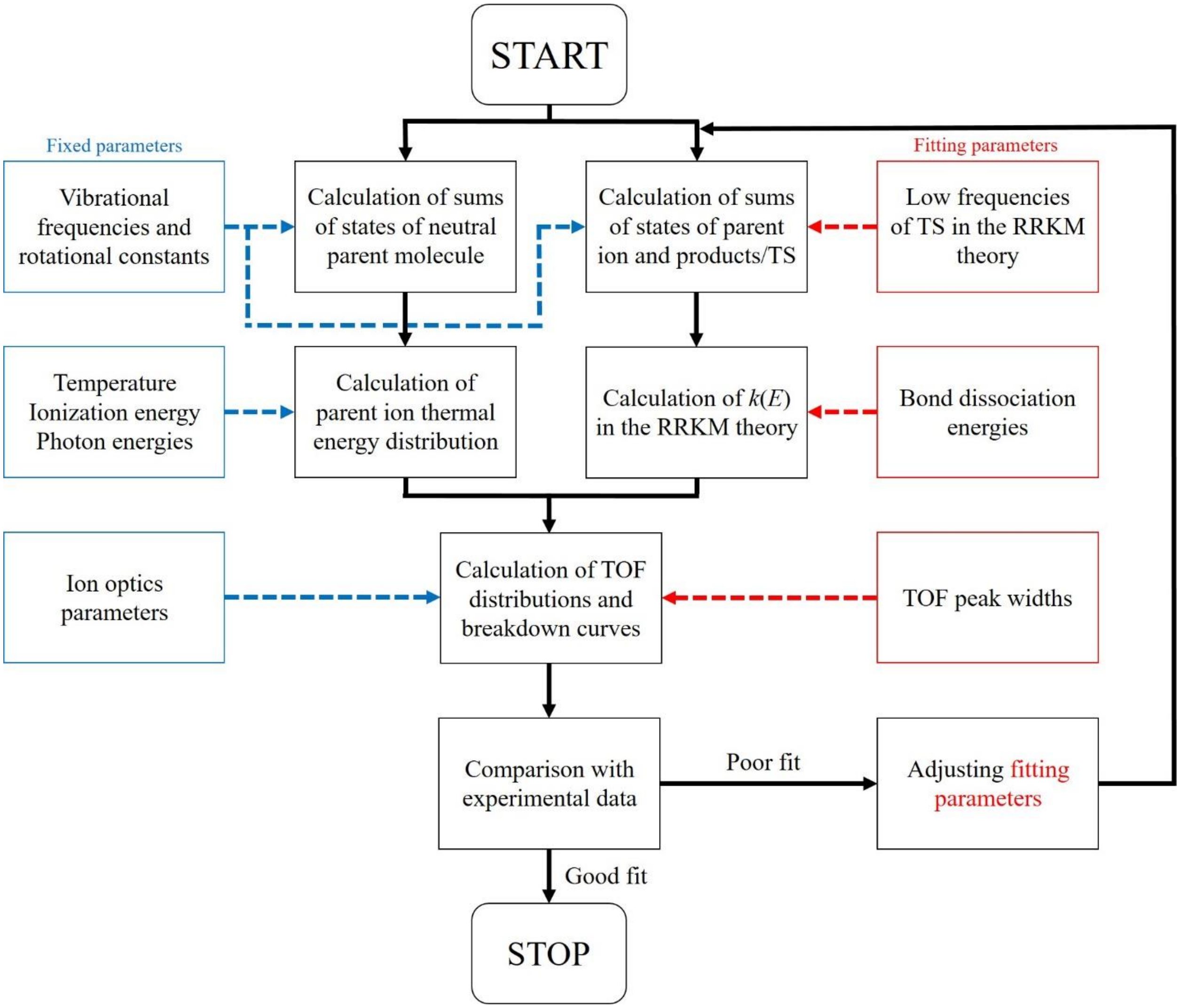

Figure 7. Block diagram of the PEPICO modeling process.

The energy resolution in a TPEPICO experiment is significantly narrower than the thermal energy distribution of the molecular ion produced in the photoionization process. Therefore, it is imperative to interpret the measured decay rates in terms of $k(E)$ distribution. The Boltzmann formula can be used to calculate the thermal energy distribution of a neutral sample at a given temperature:

$$P(E) = \frac{\rho(E) e^{-E/k_B T}}{\int_0^\infty \rho(E) e^{-E/k_B T}} \tag{27}$$

where $P(E)$ is the energy distribution, $\rho(E)$ is the ro-vibrational density of states, k_B is the Boltzmann constant. The energy distribution of a neutral molecule is transposed onto the ion manifold, and if the internal energy is larger than the dissociation energy, dissociation of the ion will happen. The energy distribution of the parent ion can be obtained by the internal energy of the neutral molecule, the photon energy, and the adiabatic ionization energy. In the case of fast dissociations, fragmentation of the parent ion occurs in the ionization region and therefore, the shape of breakdown curves represents the integrated thermal energy distribution. On the other hand, the time requirement for a parent ion to fully dissociate is practically infinite for slow dissociations just above the threshold energy. Thus, it causes a shift (kinetic shift; *see Chapter 2.3.1*) in the breakdown diagram towards higher photon energies.[53-54,74] The amplitude of this effect can be calculated by knowing the dissociation rate. Sequential dissociations require the knowledge of the energy distribution of the first fragment ion and its neutral fragment.[75] Klots' equation is used to calculate how much energy the leaving atom takes away from the fragment ion at a virtual temperature in a canonical formalism.[76-77] Microcanonical formalism can also be used to calculate the excess energy distribution between the fragment ion and the neutral fragment in the energy distribution function using densities of states of the translational degrees of freedom and that of the fragment ion:

$$p(E_i, E - E_0) = \frac{\rho_{A^+}(E_i)\rho_{tr}(E - E_0 - E_i)}{\int_0^{E-E_0} \rho_{A^+}(x)\, \rho_{tr}(E - E_0 - x)dx} \tag{28}$$

where $p(E_\mathrm{i}, E - E_0)$ is the probability of the fragment ion to retain E_i energy from the total excess energy of $E - E_0$, ρ_{A^+} and ρ_{tr} are the densities of states of the fragment ion and the translational degrees of freedom, respectively.

The source of the adiabatic ionization energy can be either photoelectron spectroscopic measurements or quantum chemical calculations and is used in the calculation of the internal energy of the parent ion upon ionization. In the modeling process, the bond dissociation energies (BDE) and vibrational frequencies are optimized to achieve the best possible fit of the breakdown diagram or, for slow dissociations, the TOF distributions as well. Dissociation processes that include tunneling (not discussed in this work) or isomerization of the parent ion (*see Chapter 2.3.6*) require the optimization of the reverse barrier height and critical frequency, or the reverse barrier height, isomer stabilization energy, and isomer TS frequencies, respectively. Depending on the leaving neutral fragment two, four, or five of the lowest vibrational frequencies are optimized for a spherically symmetric, a linear, or a nonlinear loss, respectively, as these turn into product translational and rotational modes. The fractional abundance of the parent ion can be given as:

$$BD(h\upsilon) = \int_0^{E_0 - IE} P_i(E, h\upsilon)dE \cong \int_0^{E_0 - h\upsilon} P_n(E)dE \tag{29}$$

where P_i is the normalized internal energy distribution of the ion as a function of internal energy at a given photon energy and P_n is the internal energy distribution of the neutral molecule. This latter term can be calculated by the Boltzmann formula:

$$P_n(E) = \rho_n(E)e^{-E/_{kT}} \tag{30}$$

where ρ_n is the density of states of the neutral molecule at energy E. The second integral above is zero, when the photon energy is equal to E_0, meaning that the entire distribution is above the dissociation limit. Therefore, the photon energy where the parent ion abundance reaches zero is the 0 K appearance energy but it was found that modeling the breakdown diagram provide a more reliable result.

On the other hand, slow dissociations result in a kinetic shift and therefore an extra term had to be included which accounts for the probability that the ion will not dissociate within the time frame of the experiment:

$$BD(h\upsilon) = \int_0^{E_0-IE} P_i(E,h\upsilon)dE + \int_{E_0-IE}^{\infty} P_i(E,h\upsilon) \times e^{-k(E)\tau_{max}dE} \tag{31}$$

where $k(E)$ is the RRKM rate constant and τ_max is the maximum time of flight within which a dissociating ion is detected as a fragment ion. The added term broadens and shifts the breakdown diagram to higher energies. Consequently, kinetic shifts are accounted for quantitatively as time-of-flight peak shapes yield absolute dissociation rates. It is noteworthy that by definition E_0 is referenced to the ground state neutral molecule, hence, it is the sum of the adiabatic ionization energy (AIE) and the bond dissociation energy (BDE). Therefore, the error of the AIE has a significantly less effect on E_0 than on BDE values.[78]

The error of the model is evaluated by a two-variable function. Its first part is to compare the experimental BD to the modeled one, whereas the second is to describe the differences in the

TOF distributions. Zero means there is a perfect match between the experimental and the modeled data. Every parameter is adjusted iteratively with a downhill simplex algorithm.[79]

2.3.5. Isomerization of the Molecular Ion

There are many cases where the molecular ion undergoes reversible isomerization prior to dissociation. The product ions can be formed from either the parent ion or from its isomer. The branching ratios and rate constants can be modeled with any number of parallel channels within the RRKM theory.

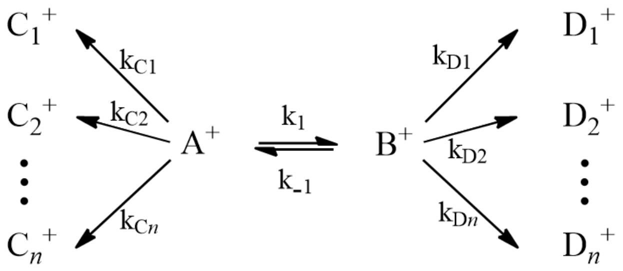

Figure 8. Isomerization of A^+ molecular ion to B^+ and their fragmentation to $C_1^+ \ldots C_n^+$ and $D_1^+ \ldots D_n^+$ ions, respectively.

For a hypothetical system shown on Figure 8, where A^+ molecular ion reversibly isomerizes to B^+, and A^+ dissociates to ($C_1^+ \ldots C_n^+$) and B^+ to ($D_1^+ \ldots D_n^+$), the kinetics of the isomerization/dissociation reactions can be described with a set of differential equations:

$$\frac{d[A^+]}{dt} = -k_1[A^+] + k_{-1}[B^+] - \sum\nolimits_i k_{Ci}[A^+] \tag{32}$$

$$\frac{d[B^+]}{dt} = k_1[A^+] - k_{-1}[B^+] - \sum\nolimits_i k_{Di}[B^+] \tag{33}$$

$$\frac{d[C_i^+]}{dt} = k_{Ci}[A^+] \tag{34}$$

$$\frac{d[D_i^+]}{dt} = k_{Di}[B^+] \tag{35}$$

The analytical solutions of these equations are programmed into the modeling code:

$$k_{fast} = \frac{1}{2}\left[\left(k_1 + k_{-1} + \sum_i k_{Ci} + \sum_i k_{Di}\right) + k_x\right] \tag{36}$$

$$k_{slow} = \frac{1}{2}\left[\left(k_1 + k_{-1} + \sum_i k_{Ci} + \sum_i k_{Di}\right) - k_x\right] \tag{37}$$

$$k_x = \sqrt{\left(k_1 + k_{-1} + \sum_i k_{Ci} + \sum_i k_{Di}\right)^2 - 4\left[\left(k_1 + \sum_i k_{Ci}\right)\left(k_{-1} + \sum_i k_{Di}\right) - k_1 k_{-1}\right]} \tag{38}$$

$$[A](t) = \frac{1}{k_{fast} - k_{slow}}\left[\left(k_{fast} - k_{-1} - \sum_i k_{Di}\right)e^{-k_{fast}t} + \left(-k_{slow} + k_{-1} + \sum_i k_{Di}\right)e^{-k_{slow}t}\right] \tag{39}$$

$$[B](t) = \frac{k_1}{k_{slow} - k_{fast}}\left[e^{-k_{fast}t} - e^{-k_{slow}t}\right] \tag{40}$$

$$[C_i](t) = \frac{k_{Ci}}{k_{slow} - k_{fast}}\left[\frac{\left(-k_{fast} + k_{-1} + \sum_i k_{Di}\right)}{k_{fast}}\left(1 - e^{-k_{fast}t}\right) - \frac{\left(-k_{slow} + k_{-1} + \sum_i k_{Di}\right)}{k_{slow}}\left(1 - e^{-k_{slow}t}\right)\right] \tag{41}$$

$$[D_i](t) = \frac{k_1 k_{Di}}{k_{slow} - k_{fast}}\left[\frac{\left(1 - e^{-k_{fast}t}\right)}{k_{fast}} - \frac{\left(1 - e^{-k_{slow}t}\right)}{k_{slow}}\right] \tag{42}$$

In summary, in the case of two molecular ion isomer structures, each fragment ion is formed with two apparent rate constants, k_{fast} and k_{slow}, which can manifest themselves in the TOF spectra as double-exponential asymmetric daughter ion peaks. Therefore, such features in the experimental TOF spectra indicate that isomerization might be at play.

2.4. Quantum Chemical Calculations

As it was discussed in the previous section, quantum chemical calculations play an important role in the modeling procedure. Density Functional Theory (DFT), specifically B3LYP hybrid functional, is most commonly used in the Sztáray group. It provides vibrational frequencies and rotational constants for the RRKM model. For large molecules, especially for organometallic compounds this computational level is the most realistic to use as the size of the molecules hinder the explicit treatment of the electron correlations.

Bond dissociation energies for systems with a relatively low number of heavy atoms can be accurately determined using composite methods such as G4, CBS-QB3/APNO, and W1U, or with Coupled Cluster (CC) methods. Generally, high accuracy can be obtained from highly correlated methods with large basis sets. Composite methods were developed in order to decrease the computational cost while keeping a relatively high accuracy. They employ various approximations in estimating the electron correlation energy and the energy from translation, rotation, and vibrations. In addition, composite methods contain empirical expressions that aim to correct for non-considered correlation effects. The aforementioned G4 and CBS methods are capable of calculating energies within 2–4 kJ mol^{-1} but the maximum error can reach even 20 kJ mol^{-1}.[80] The W*n* methods were developed by Martin *et al.*[81] and aimed to reach 1 kJ mol^{-1} accuracy by including relativistic corrections.

Describing the potential energy surface (PES) is important to unveil dissociation mechanisms and possible dissociation products. The thermochemical limit, which is the minimum energy of a product ion and neutral fragment to form, is used to rule out dissociation pathways that are higher in energy than the experimentally observed ones. Transition state (TS) structures were located using relaxed potential energy scans along the bond breaking coordinates. The local maximum on the PES was optimized as a transition state. In the cases, where the TS is hard to find, Synchronous Transit-Guided Quasi-Newton (STQN) method can be used. It searches for a saddle point along the PES between the reactant and the product ions. In the mode, called QST2, only a reactant and product ion structures are provided, whereas with QST3 a guess TS structure is given. Upon finding a transition state, intrinsic reaction coordinate

(IRC) calculation is done to confirm that the TS is in fact the local maximum connecting the reactant with the product on the PES. Detailed description on the performed calculations is given in the appropriate chapters of each project.

CHAPTER 3: RESULTS AND DISCUSSION

3.1. Toluene and 1,3,5-Cycloheptatriene

3.1.1. Background

Due to their ubiquity in the mass spectra of aromatic compounds, the decomposition of gaseous $C_7H_8^+$ ions is one of the most widely studied ion reactions. These investigations were carried out by techniques including, but not limited to, collisional activation,[82-83] photoionization,[3,84-85] ion cyclotron resonance mass spectrometry,[2,86-87] infrared spectroscopy,[16,88] and photoelectron photoion coincidence spectroscopy.[10,89-90] Hydrogen abstraction from $C_7H_8^{+\bullet}$ ions leads to the formation of $C_7H_7^+$ cations with more than 30 different possible isomeric structures, with benzyl (Bz^+), tropylium (Tr^+), and tolyl (Tl^+) being the most important ones among them. One of these, Tr^+, has received special attention since Hückel predicted it to be a stable seven-membered ring with high aromaticity in 1931.[91] Two decades later, Doering and Knox[92] proved this by synthesizing cylocheptatrienyl bromide, which was stable both as solid and in solution. Since then, Tr^+ has become one of the seminal textbook examples for aromaticity, and has been extensively discussed, including the ionization of its neutral tropyl radical form, which presents an intriguing example of Jahn–Teller coupling.[93-95] However, while the rearrangement reaction between the almost isoenergetic Tr^+ and Bz^+ has been the subject of several experimental and theoretical works, the driving forces guiding the reactive flux to one or the other in dissociation processes remain somewhat elusive and, even after 60 years,[4,96-102] the benzylium/tropylium ion dichotomy continues to motivate new experimental studies.[16,88,103]

Hydrogen atom loss from the toluene molecular ion was originally thought of as simple bond cleavage resulting in the formation of the benzyl ion. However, studies with ^{13}C and deuterium labeling[104-107] were not consistent with this simple mechanism. Hydrogen radical loss from the $C_6H_5CD_3^{+\bullet}$ molecular ion indicated a statistical D:H ratio of approximately 3:5, *i.e.*, the equivalence of all eight hydrogen atoms. The same was observed in the successive acetylene elimination from $C_7H_7^+$ ions and their deuterated equivalents, as well.

To account for this observation, Rylander *et al.*[104] claimed that the hydrogen-loss product of the toluene molecular ion has to be symmetrical, for which the tropylium ion is a good candidate. In order to lose the original locational identity of the hydrogens, rearrangements have to happen before or during fragmentation. The proposed mechanism included an irreversible isomerization step from the toluene molecular ion ($Tol^{+\bullet}$) to the 1,3,5-cycloheptatriene ($CHT^{+\bullet}$) ion, ruling out the benzyl ion H-loss product. Numerous publications about several $C_7H_8^{+\bullet}$ isomers[1,108-111] supported Rylander *et al.*'s theory and all shared a common element: the $CHT^{+\bullet}$ molecular ion as central intermediate. Meyerson and Rylander[105] provided additional support to this hypothesis by a ^{13}C labeling study on toluene.

Historically, the irreversible isomerization of the toluene molecular ion to $CHT^{+\bullet}$ was so widely accepted that when Meyer and Harrison[112] found that, in some cases, a methyl hydrogen-loss is favored, it was explained as an effect of the incomplete randomization of the hydrogen atoms in the $CHT^{+\bullet}$ molecular ion, but without questioning the general validity of the CHT-centered mechanism.

As advanced mass spectrometric techniques, such as ion–molecule reactions[2] and collisional activation became available,[113-115] it was revealed that not all $Tol^{+\bullet}$ molecular ions go through ring expansion to form $CHT^{+\bullet}$ (Scheme 1), but Bz^+ can also be formed from energetic

Tol$^{+\bullet}$ ions by a simple C–H bond cleavage, which may be followed by isomerization to produce the energetically more stable Tr^{+} if the internal energy of the Bz^{+} product ion is sufficient to overcome the isomerization barrier. Furthermore, a high-energy H-loss reverse barrier in CHT$^{+\bullet}$ to the more stable product Tr^{+} was proposed to render the thermochemical limit to form either fragment ion nearly equal.[97,99] We will show that said reverse barrier still lies considerably below the Bz^{+} formation threshold, but, combined with kinetic effects, the argument that the two channels should be competing with each other still holds. Furthermore, it also implies that CHT$^{+\bullet}$ may also yield both H-loss fragment isomers, which we will examine later in this paper.

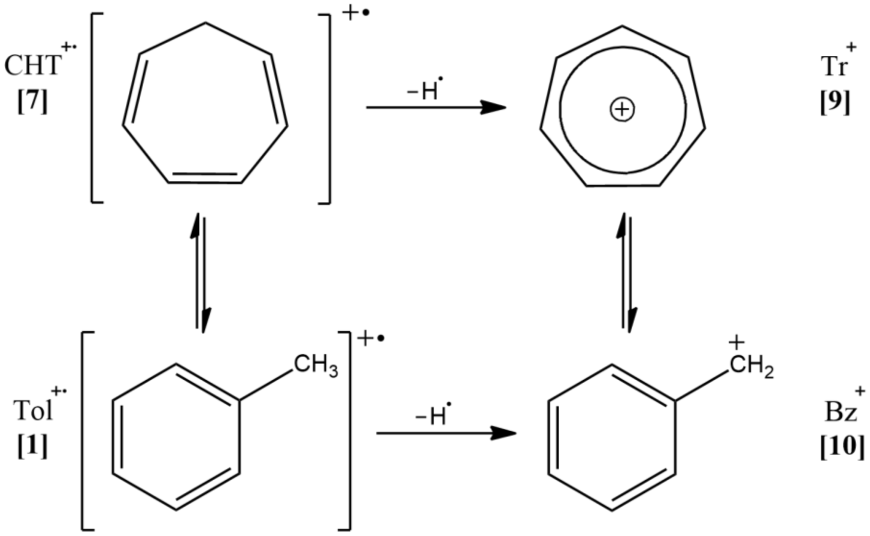

Scheme 1. General scheme for the formation of Bz^{+} and Tr^{+} cations from CHT$^{+\bullet}$ and Tol$^{+\bullet}$. The structures of intermediates and transition states are shown in Figures 11 and 12.

To determine the relative yield of Bz^{+} and Tr^{+} under various conditions barring their direct isomerization, ion–molecule reactions were found to be especially effective, because only Bz^{+} reacts by methylene transfer with, e.g., toluene or ethylbenzene, to form benzene and $C_8H_9^{+}$, or $C_9H_{11}^{+}$, respectively. However, experimental results showed some inconsistences, mainly because of the low energy difference and low activation barrier for isomerization between these two isomers.[99-102,116]

Imaging photoelectron photoion coincidence spectroscopy (iPEPICO) coupled with synchrotron radiation is a powerful tool to elucidate complex dissociation mechanisms and determine highly accurate photoionization onsets of gas phase ions.[18,117-118] The iPEPICO setup allows for accurate energy selection of the photoions and it can also be used to directly measure dissociation rates within the range of 10^3 $s^{-1} < k < 10^7$ s^{-1}.[32,119] The fractional ion abundances are customarily plotted in the breakdown diagram as a function of photon energy and are then modeled, together with the dissociation rate information extracted from time-of-flight mass spectra, using statistical rate theories. This approach was used to explore complex dissociation mechanisms, including isomerization processes as well as large kinetic and competitive shifts.[117,120-123] PEPICO does not offer isomer selective identification of isobaric fragment ions in the absence of diverging sequential fragmentation processes, which complicates the study of cycloheptatriene and toluene, since both are expected to yield Bz^+ and Tr^+ close to threshold. However, by recording high-resolution breakdown diagrams for $CHT^{+\bullet}$ and $Tol^{+\bullet}$, we hope to uncover evidence for the co-existing H-loss channels, and our goal is to construct a single statistical model to describe both systems simultaneously and, thereby, determine accurate appearance energies for the Bz^+ and Tr^+ fragment ions from both precursors.

3.1.2. Experimental and Theoretical Details

The experiments have been carried out on the iPEPICO endstation[119] at the Vacuum Ultraviolet (VUV) beamline[124] of the Swiss Light Source. Toluene and 1,3,5-cycloheptatriene were purchased from Sigma–Aldrich and used without further purification. Samples were introduced into the ionization chamber through an effusive inlet at room temperature and were intersected with the monochromatic radiation of the synchrotron beamline. Photoelectrons were extracted using a continuous 80 V cm^{-1} electric field and were velocity map imaged onto a delay-line Roentdek DLD40 imaging detector. Threshold electrons are detected at the center of the detector, while kinetic energy ("hot") electrons are only focused there if they have no off-axis momentum component. Therefore, this contribution of hot electrons can be subtracted from the center signal, based on the signal in a ring area around the center spot, thereby yielding only coincidences with threshold photoelectrons.[41] The detection of the electrons provides the start signal for the time-of-flight analysis of the coincident photoions, in a multiple-start/multiple-stop coincidence data acquisition scheme.[32]

The photoions are extracted toward a two-stage Wiley–McLaren[125] time-of-flight mass spectrometer (TOF-MS) and are space focused onto a non-imaging multichannel plate (MCP) detector. Due to the low extraction field and the long extraction region, they have a relatively long residence time (on the order of microseconds) in the first acceleration region. If the time it takes for the ion to dissociate is comparable to the time spent in this region, the time of flight of the fragment ions produced in the acceleration region will be longer than the nominal daughter ion TOF. This means that, if the mass difference between the molecular and fragment ions is significantly larger than the mass resolution of the instrument, the daughter ion peak will exhibit a broad, quasi-exponential shape towards higher *m/z* ratios, indicative of the dissociation rate constant.[29,117] This way, dissociation rates of 10^3–10^7 s^{-1} can be measured and the modeled rates are then fitted to these experimental data points, quantifying the kinetic shift and aiding the reliable extrapolation to the dissociation threshold. For the case of hydrogen loss from $C_7H_8^+$, however, the small mass difference between the molecular ion and the fragment ion is commensurate with the instrumental peak width, which obscures the pseudo-exponential shape. Yet even in such cases, the rate information can still be extracted based on the slight shift of the apparently symmetric fragment ion TOF peak center as a function of photon energy.[118,126] It was shown that this approach is suitable to extract accurate reaction rates when the asymmetric peak shapes are not clearly observable or the signal levels are low.[118,126-127] However, as the parent and H-loss peaks were not baseline separated in our case, we fitted the TOF distributions using three Gaussians and determined the shift in the daughter ion peak center based on this fit (see later).

3.1.3. *Ab Initio* Calculations

Quantum chemical calculations were performed using the Gaussian 09 suite of programs.[128] We used density functional theory to explore the potential energy surface and unveil the dissociation and isomerization pathways of $C_7H_8^{+\bullet}$ ions. Stationary points on the potential energy surface (PES) were located for toluene and 1,3,5-cycloheptatriene neutrals, parent and fragment ions as well as along the reaction coordinates at the B3LYP/6-311++G(d,p) level of theory. Approximate transition state (TS) structures were located and reaction paths were obtained by constrained optimizations (in which bond lengths were scanned), as well as by STQN calculations.[129-130] Normal mode analysis confirmed the nature of stationary points as TS structures or minima. We also carried out intrinsic reaction coordinate (IRC) calculations to check that the transition states connect the respective minima. The energies of the stationary points that likely play a role in the dissociation processes were refined by G4[131] and CBS-APNO[132] composite methods and also by CBS-QB3[133-134] and W1U[81] for accurate energetics. We would like to note that the second, QCISD/6-311G(d,p) geometry optimization step in CBS-

APNO, as implemented in Gaussian 09, always searches for a minimum, but uses the density functional force constant matrix in the first iteration. Thus, if the DFT and QCISD transition state geometries are similar, the QCISD optimization may also converge to the transition state, as was the case in all transition state calculations reported herein. This fortunate outcome allows us to report CBS-APNO transition state energies, as well. Harmonic vibrational frequencies, rotational constants, and zero-point energies of the optimized geometries were extracted and used in the RRKM model of dissociative photoionization.

3.1.4. Breakdown Diagram and TOF Distribution Modeling

The standard tools of statistical thermodynamics and rate theories were used to calculate the thermal internal energy distribution of the neutral sample (which is transposed to the ionic manifold and convoluted with instrument resolution functions) and the dissociation rate constants of the molecular ions. The dissociation rates were calculated using the rigid activated complex Rice–Ramsperger–Kassel–Marcus (rac-RRKM) theory.[117,135] The unimolecular rate constants, $k(E)$, are calculated by equation (24) described in Chapter 2.3.2. on the RRKM theory. The densities and sums of states are calculated using harmonic vibrational frequencies by the Beyer–Swinehart direct count algorithm.[136] In the toluene neutral and cation, the contribution of the methyl internal rotation to the density of states was approximated as a Pitzer rotor.[137]

3.1.5. PEPICO Experiments

Time-of-flight mass spectra of internal energy selected $Tol^{+\bullet}$ [**1**] and $CHT^{+\bullet}$ [**7**] molecular ions were collected in the 11.45–12.55 and 10.30–11.75 eV photon energy ranges, respectively, in which dissociative photoionization leads to hydrogen-loss fragment ions.

As explained above, the low electric field in the long extraction region is essential to obtain unimolecular rate information, revealed, in our case, by the shifting fragment ion peak centers for H-loss at $m/z = 91$. As a matter of fact, the parent and fragment ion peaks in the time-of-flight mass spectra are not baseline separated for $[M]^{+\bullet}$ ($m/z = 92$) and $[M - 1]^+$ ($m/z = 91$) therefore, we applied peak fitting (Figure 9) to extract the experimental ion fractional abundances and the fragment ion peak center shift as a function of photon energy, to construct the breakdown diagrams and obtain the rate information at the same time (Figure 10).

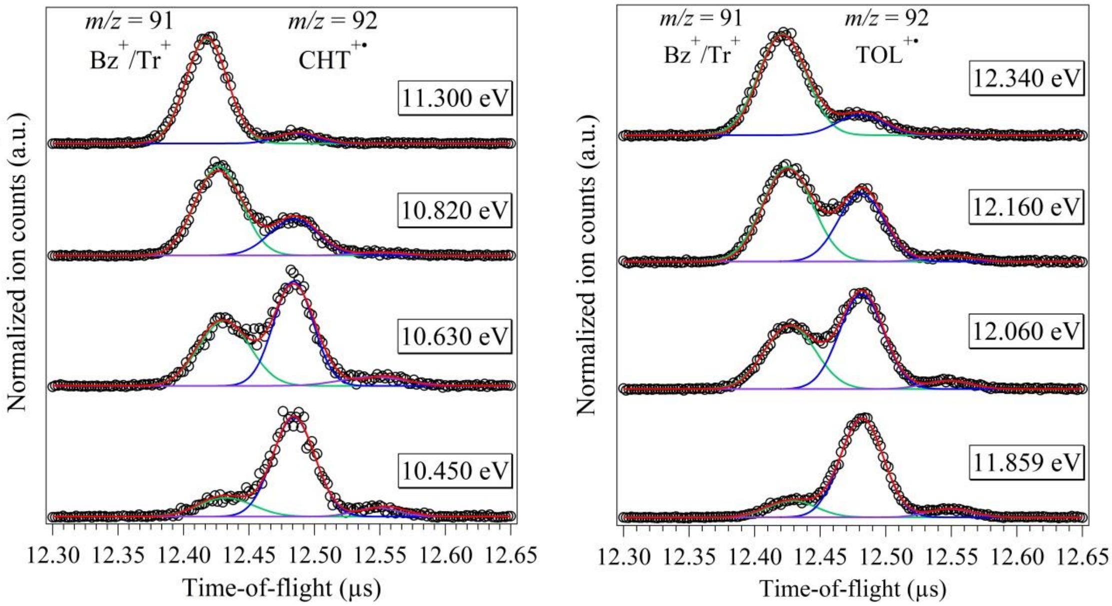

Figure 9. Sample threshold photoionization TOF spectra of CHT (left) and Tol (right). Open circles are experimentally measured ion abundances. Three Gaussian peaks were fitted to the TOF distributions to extract experimental ion fractional abundances are shown in green, blue, and purple for $[M–H]^+$, $[M]^+$, and $[M+1]^+$ peaks, respectively. The sum of these Gaussians is shown in red.

Three Gaussian functions were fitted to each TOF mass spectrum: one for the H-loss, one for the molecular ion, and one for the ^{13}C isotope peak of the molecular ion. Neglecting the double ^{13}C isotopologues at +2 amu, the peak area of the fitted peaks was used to calculate the fractional ion abundances according to the following equations:

$$A_{\mathrm{total}} = A_{91} + A_{92} + A_{93} = (A_{\mathrm{P}} + A_{\mathrm{D}})(1 + B_{\mathrm{isot}}) \tag{43}$$

$$A_{91} = A_{\mathrm{D}} \tag{44}$$

$$A_{92} = A_{\mathrm{P}} + A_{\mathrm{D}}\, B_{\mathrm{isot}} \tag{45}$$

$$A_{93} = A_{\mathrm{P}}\, B_{\mathrm{isot}} \tag{46}$$

where A_{total} is the sum of the areas of the integrated peaks of m/z = 91, 92 and 93, A_{91}, A_{92}, A_{93} respectively; and B_{isot} is the isotope abundance ratio (n.b., not percentage) between the ^{12}C$_7$ and the ^{12}C$_6$^{13}C isotopologues. A_{P} and A_{D} stand for the all-^{12}C part of the parent and daughter ion signals, respectively. Because only a hydrogen loss occurs, the peak at m/z = 92 encompasses both the all-^{12}C molecular ion and the ^{13}C peak of m/z = 91. Since the theoretical ratio of the ^{13}C peak (B_{isot}) is the same 7.6% for both ions, we can calculate B_{isot} for every photon energy after combining and rearranging the equations above:

$$(A_{92} - A_{91}\, B_{\mathrm{isot}})\, B_{\mathrm{isot}} = A_{93} \tag{47}$$

The physically meaningful root of this quadratic equation for B_{isot} was used to validate the fitting procedure, which yielded the fractional abundances, plotted in the breakdown diagram, and the shifting centers of gravity of the H-loss peak, indicative of the dissociation rate constant, as a function of photon energy.

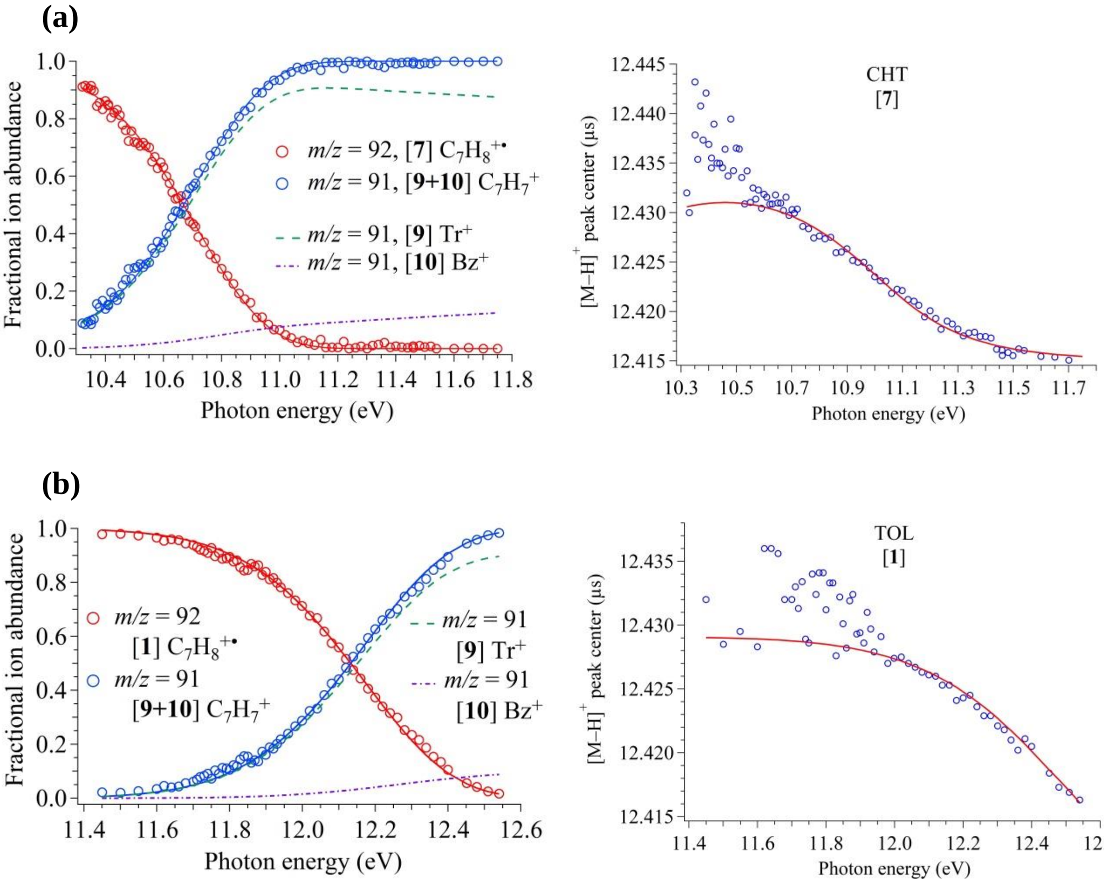

Figure 10. 1,3,5-cycloheptatriene (a) and toluene (b) breakdown diagrams and H-loss peak center shifts. Open circles are experimental data; solid lines are the best fit modeling of the data. Green and purple dashed lines show the contribution of the Tr^+ and Bz^+ ions to the overall *m/z* = 91 signal, respectively.

3.1.6. Potential Energy Surfaces

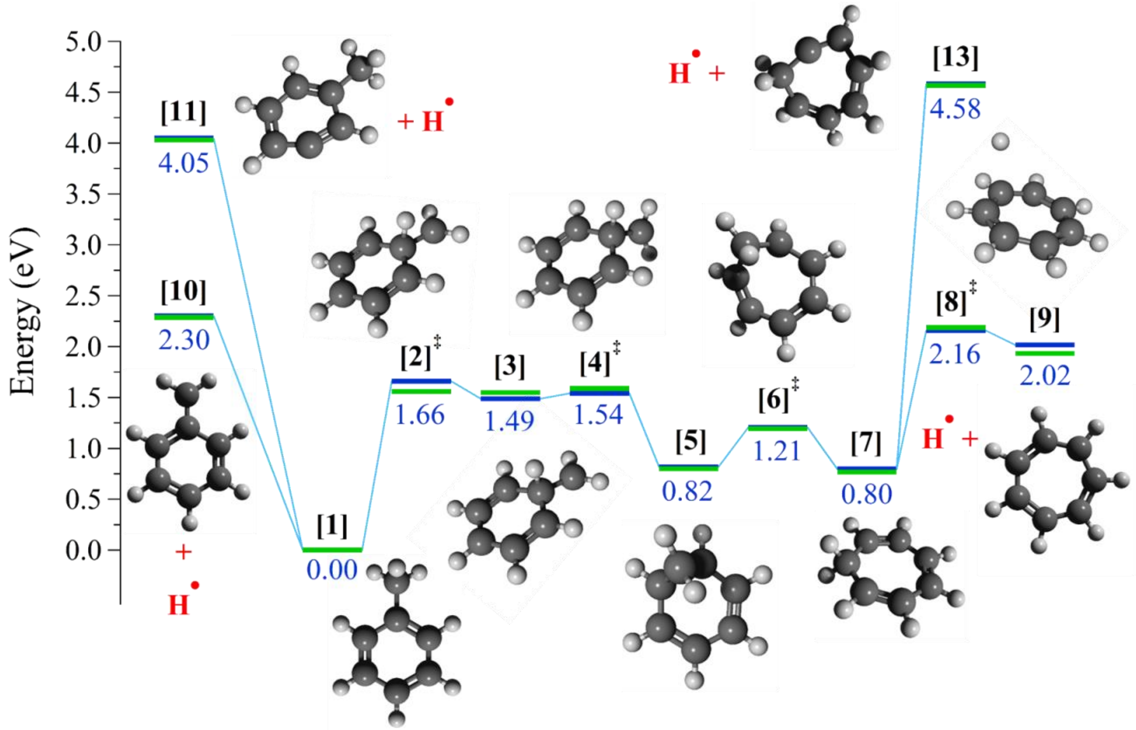

Figure 11. Potential energy surface of the isomerization and dissociative ionization pathways of 1,3,5-cycloheptatriene and toluene cations with the G4 (blue) and CBS-APNO (green) energies at 0 K. The TS geometries are marked with a double dagger, and all energies are relative to the $Tol^{+\bullet}$ molecular ion.

The potential energy surface (PES) connecting the two molecular ions with each other and with the H-loss fragment ions was explored to obtain a starting point for the statistical model (Figure 11). The calculated relative energies and structures are in good agreement with and confirm the previously reported isomerization pathway by Bullins *et al.*[100] and Choe.[116] However, the TS found uniquely by Bullins *et al.* for direct H loss from $Tol^{+\bullet}$ to Bz^{+} could not be located and it was probably an artifact at the HF/6-31G(d,p) and B3LYP/6-311++G(2d) levels of theory they used. On the other hand, Choe used the G3 composite method, with respect to which the present results only represent a minor improvement. The isomerization of $Tol^{+\bullet}$ [**1**] to form

CHT$^{+\bullet}$ [**7**] was studied first, which is the first isomerization step connecting the toluene cation to the most stable, Tr^{+} fragment ion. The mechanism for (Tol $\xrightarrow{-e^{-}}$) Tol$^{+\bullet}$ [**1**] → CHT$^{+\bullet}$ [**7**] → Tr^{+} [**9**] + H begins with a H-migration from the CH$_3$-carbon *via* a tight TS [**2**]‡ at 1.66 eV relative to the Tol$^{+\bullet}$ [**1**] and leads to the first intermediate [**3**] at 1.49 eV. Two more lower lying saddle points, [**4**]‡ and [**6**]‡, were located on the potential energy surface along with one intermediate structure, [**5**], leading to ring expansion and CHT$^{+\bullet}$ [**7**] formation at 0.80 eV.

The last step in the formation of the Tr^{+} [**9**] cation is H-loss from CHT$^{+\bullet}$ [**7**], which, as reported in the literature,[12,97,100,116] does not occur at the thermochemical threshold, due to a reverse barrier. An orbiting transition state [**8**]‡ was found by scanning a C–H bond length in the methylene group at 2.16 eV, 0.5 eV above the TS [**2**]‡ leading to ring expansion from Tol$^{+\bullet}$ [**1**].

We explored an alternative H-loss possibility in CHT$^{+\bullet}$: the C–H bond located next to the methylene carbon was stretched, which resulted in a dissociation without a saddle point producing the high-energy 1-cycloheptatrienyl cation [**13**], shown in Figure 11 at 4.58 eV. The Tol$^{+\bullet}$ [**1**] molecular ion may also lose a hydrogen atom directly from the aromatic ring or from the methyl carbon without first isomerizing to CHT$^{+\bullet}$. Scanning the C–H bond length in the methyl group yields a purely attractive potential energy curve, *i.e.*, indicates a dissociation without a reverse barrier to form benzyl ion, Bz^{+} [**10**], at 2.30 eV relative to the toluene molecular ion. One example of a H-loss from the aromatic ring is also shown in Figure 11. The C–H bond length in the *meta* position can be broken at 4.05 eV to yield the *m*-tolyl ion [**11**] without a saddle point. The other two isomers, *ortho* and *para* can be formed at 3.99 and 4.13 eV, respectively. These processes are beyond our experimental energy range and are not considered in the statistical model.

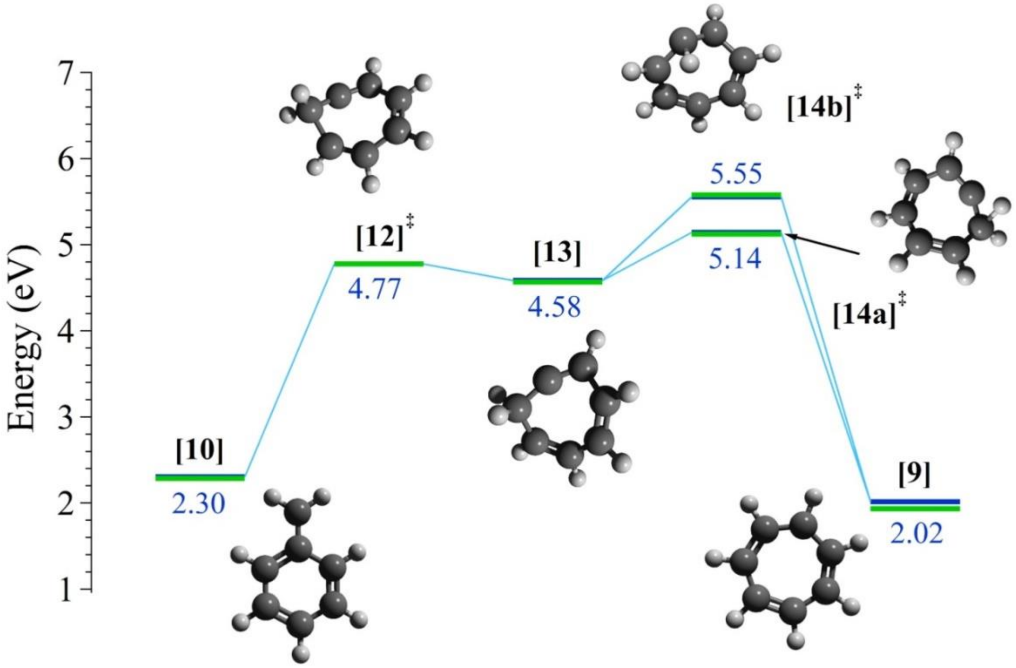

Figure 12. Potential energy surface (PES) of the isomerization pathway between Bz^+ and Tr^+ ions with G4 (blue) and CBS-APNO (green) energies at 0 K. Transition states are marked with a double dagger. All energies are relative to the $Tol^{+\bullet}$ molecular and only G4 energies are listed.

The above-mentioned 1-cycloheptatrienyl cation [**13**] is also implicated in the isomerization pathways connecting Bz^+ [**10**] and Tr^+ [**9**], as shown in Figure 12. Even the lower energy transition state [**12**]‡ connecting [**13**] to one of the fragment ions (Bz^+ [**10**]) is at 4.77 eV, while the transition state [**14a**]‡ towards the other fragment ion (Tr^+ [**9**]) is even higher at 5.14 eV, both relative to $Tol^{+\bullet}$ [**1**]. Since this saddle point, which is higher than our experimental energy range, would have to be overcome to allow for the interconversion of the two isomers, we conclude that the Bz^+ ↔ Tr^+ interconversion is not implicated under our experimental conditions. Therefore, the isomeric identity of the H-loss fragment ions should be preserved in the photon energy range of our experiment. Note, however, that in the absence of isomer specific sequential dissociation processes, the experimental data would not be affected by Bz^+ ↔ Tr^+ interconversion.

3.1.7. Statistical Model of Dissociative Ionization

The transition state connecting the $C_7H_8^+$ isomers lies at a lower energy than the barrier to any decomposition channel. Therefore, the parent ion isomers may interconvert prior to fragmentation. However, there is a close-lying decay channel accessible from each of the $C_7H_8^{+\bullet}$ isomers $CHT^{+\bullet}$ and $Tol^{+\bullet}$, namely the two, almost isoenergetic H-loss channels yielding Bz^+ and Tr^+. The loose H-loss transition states and the relatively tight and only slightly less energetic isomerization transition state result in potentially slow interconversion at the dissociation threshold, and fragmentation may compete efficiently with isomerization. Based on the computational results above, we propose a simplified mechanism, shown in Figure 17, with the aim to construct a single statistical model to fit both the cycloheptatriene and the toluene experimental data simultaneously. The fitting parameters are marked blue in Figure 17, indicating energies and, for the transition states, the scaling of the transitional normal modes to fit the RRKM rate curves to the measured ones. Since the dissociation of the $Tol^{+\bullet}$ [**1**] molecular ion takes place without a saddle point, the harmonic vibrational frequencies obtained at a constrained-optimized geometry at 5.0 Å C–H bond length were used to calculate the transition state density of states, as starting point for the statistical model. The $Tol^{+\bullet}$–$CHT^{+\bullet}$ isomerization number of states function and the reverse barrier height in Tr^+ production were taken from calculations of [**2**]‡ and not fitted. The density of states of the parent ions were calculated in the harmonic approximation based on computed frequencies, with the exception of the methyl rotational contribution in the toluene cation. This has a calculated harmonic vibrational frequency of 39 cm^{-1} and a rotational barrier of only 0.9 meV, at the B3LYP/6-311++G(d,p) level of theory and was approximated as a Pitzer rotor.[135] The thermal energy distribution of the precursor neutrals was also calculated within the harmonic vibrational approximation, with the exception of the methyl internal rotation in the toluene neutral, which was treated as a Pitzer rotor (harmonic frequency of 22 cm^{-1}, rotational barrier of 2.7 meV). As discussed elsewhere,[117] the parent ion internal energy distribution is calculated from the neutral precursor's thermal energy distribution, the photon energy, the ionization energy, and the ion optics parameters. It should be noted that neither CHT$^{+\bullet}$, nor Tol$^{+\bullet}$ breakdown curves could be modeled satisfactorily assuming only a single dissociation to Tr^{+} and Bz^{+}, respectively (Figures 13 and 14).

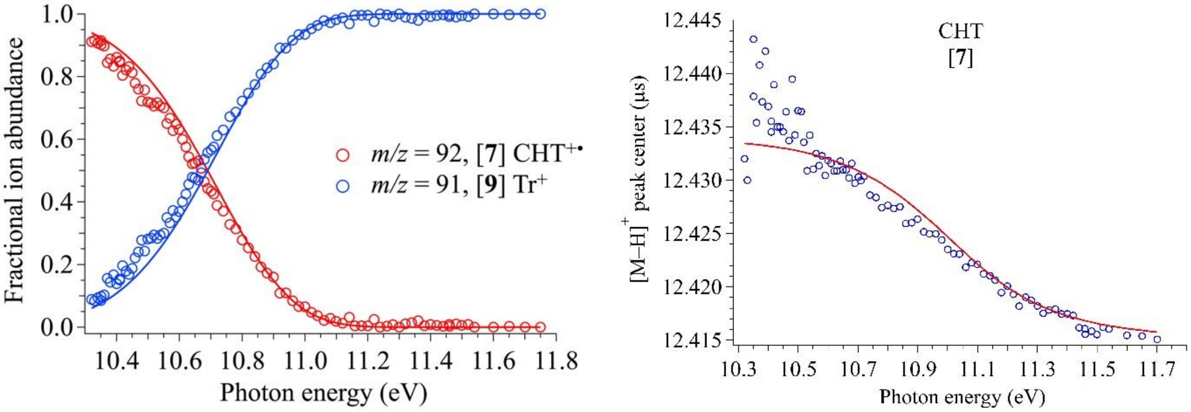

Figure 13. Breakdown diagram and H-loss peak center shifts of CHT in the 10.30 to 11.75 eV photon energy range, showing the single-well model that excludes the isomerization pathway. Closed polygons represent experimental data, while the lines show the best fit of the data with RRKM theory.

The obtained appearance energy of Tr^{+} is E_0 = 9.91 eV, which is significantly higher than the G4 calculated value of 9.60 eV and the double-well model result of 9.520 eV. Furthermore, the reaction rates could not be reproduced as shown by the H-loss peak center shifts at low-to-mid photon energies.

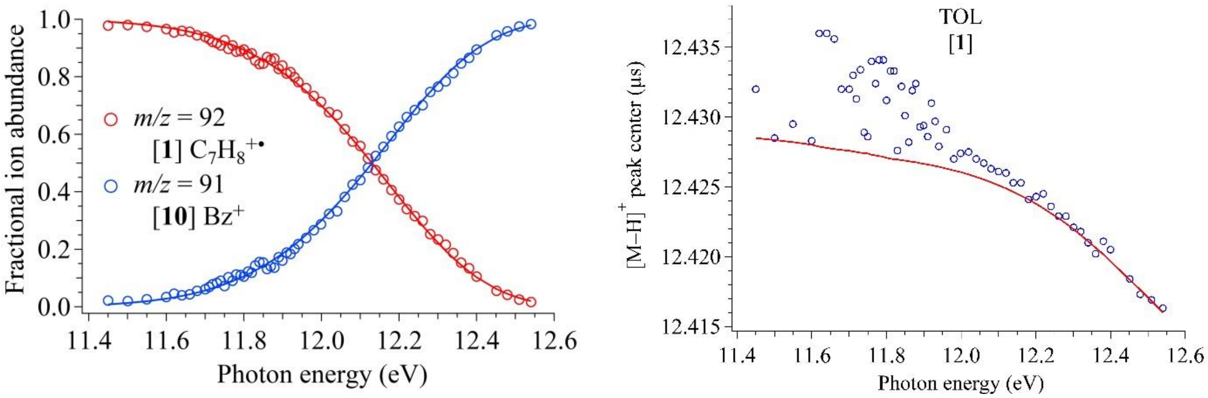

Figure 14. Breakdown diagram and H-loss peak center shifts of Tol in the 11.45 to 12.55 eV photon energy range, showing the single-well model. Closed polygons are experimental data, while the lines show the best fit of the data with RRKM theory.

Contrary to $CHT^{+\bullet}$, the obtained appearance energy of Bz^+ at E_0 = 10.91 eV is significantly lower than the G4 calculated value of 11.15 eV and the double-well result of 11.196 eV. Furthermore, the optimized activation entropy in the single-well model is unphysically high at 206.7 J mol^{-1} K^{-1} at 600 K. To prove that the double-well model is indeed necessary to model both CHT and Tol breakdown curves, we employed the SSACM approximation (Figures 15 and 16).

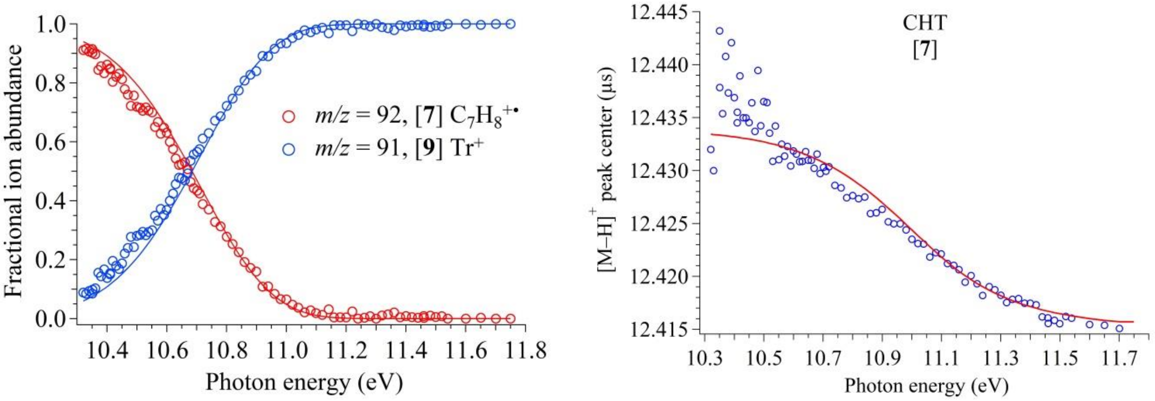

Figure 15. Breakdown diagram and H-loss peak center shifts of CHT in the 10.30 to 11.75 eV photon energy range, showing the single-well model that excludes the isomerization pathway. Closed polygons are experimental data, while the lines show the best fit of the data with Simplified Statistical Adiabatic Channel Model (SSACM) approximation.

Similarly to the RRKM model of CHT, the obtained appearance energy is significantly higher at E_0 = 9.95 eV than the G4 calculated value of 9.60 eV and the double-well model result of 9.520 eV.

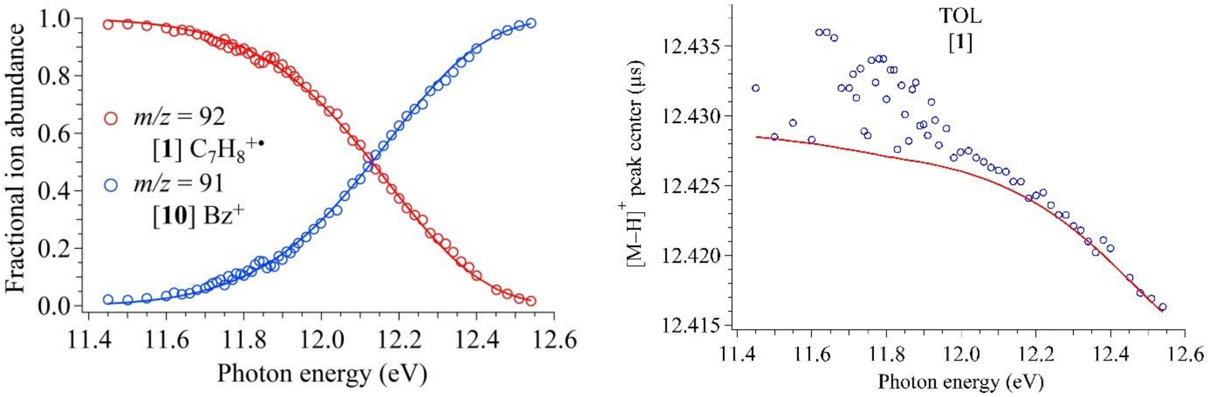

Figure 16. Breakdown diagram and H-loss peak center shifts of Tol in the 11.45 to 12.55 eV photon energy range, showing the single-well model that excludes the isomerization pathway. Closed polygons are experimental data, while the lines show the best fit of the data with Simplified Statistical Adiabatic Channel Model (SSACM) approximation.

The obtained appearance energy of Bz^+ at E_0 = 10.96 eV is lower than the G4 calculated value of 11.15 eV and the double-well result of 11.196 eV. Also, the optimized activation entropy in the single-well model is unphysically high at 198.5 J mol^{-1} K^{-1} at 600 K.

CHT undergoes large geometry change upon ionization, because the non-planar ring turns into a planar C_{2v} geometry. This makes it difficult to identify the origin transition in the photoelectron spectrum, hence, the adiabatic ionization energy of CHT. Traeger and McLoughlin reported 8.29 ± 0.01 eV as the upper limit to it using PIMS.[3] Later, Schwell *et al.* obtained 8.20 ± 0.05 eV by PEPICO.[4] To decide between these values, the AIE of CHT was calculated by G3, G4, CBS-QB3, CBS-APNO, and W1U composite methods as 8.24_0, 8.23_4, 8.18_5, 8.18_3, and 8.18_8 eV, respectively. The average value of 8.20_6 eV is in a good agreement with the experimentally measured 8.20 ± 0.05 eV by Schwell *et al*. Therefore, this experimental AIE was used to calculate the energy distribution of the $CHT^{+\bullet}$ molecular ion in the statistical model.

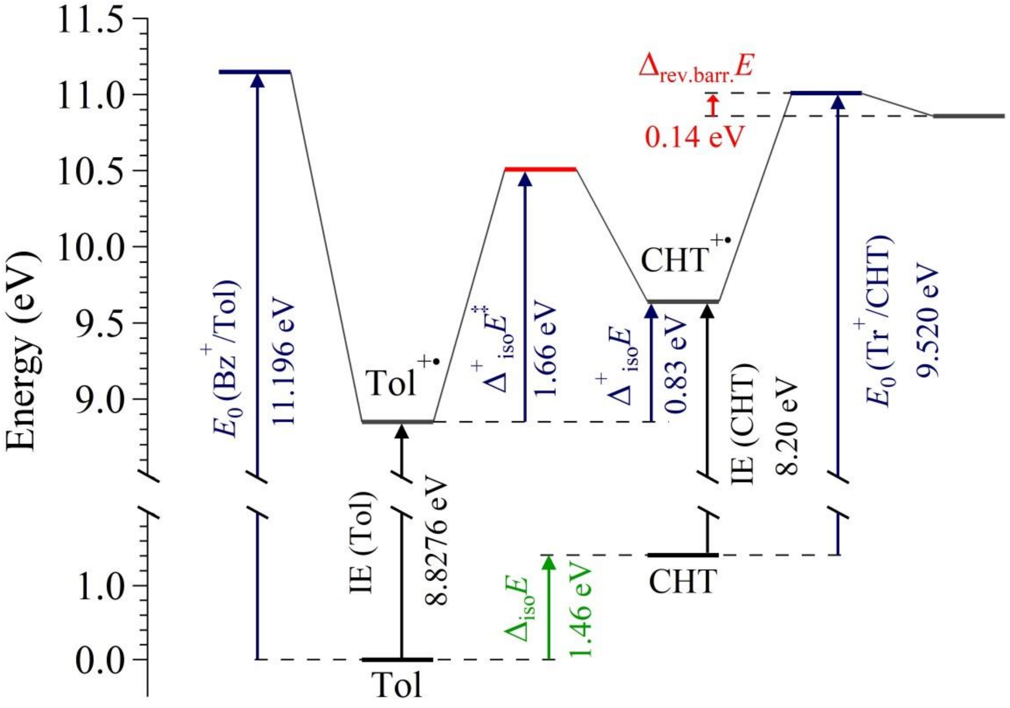

Figure 17. Schematic energy diagram of the RRKM model. The reverse barrier for H loss from $CHT^{+\bullet}$ (in red) was kept constant at its G4-calculated value. The parameters in blue were optimized to achieve the best fit of both breakdown diagrams. Parameters in black were taken from literature. The neutral isomerization energy (green) was calculated in a thermochemical cycle, see text.

The adiabatic ionization energy of Tol was reported to be 8.75 ± 0.05, 8.82 ± 0.01, 8.821 ± 0.010, and 8.8276 ± 0.0006 eV by Schwell *et al.*,[4] Bombach *et al.*,[90] Watanabe *et al.*,[138] and Lu *et al.*,[139] respectively and we used the most accurate Pulsed Field Ionization (PFI) value of 8.8276 eV in the statistical model.

The rate equation (25) also contains a symmetry number (σ) to take into account the changing degeneracies when calculating densities and numbers of states, as described by Pollak and Pechukas.[140] Due to the methyl internal rotation, we took $\sigma = 3$ for the hydrogen loss from toluene ion. The symmetry number is 2 for the H-loss from the 1,3,5–cycloheptatriene ion, because of the C_{2v} symmetry of the parent ion; i.e., both CH_2 hydrogens can leave over a small reverse barrier to produce the tropylium ion. For comparison, Bombach *et al.*[90] used $\sigma = 3$ in their statistical model of toluene ions forming Bz^+ and $\sigma = 6$ in case of Tr^+ as product ion. However, the latter value is of no concern here as toluene does not directly form Tr^+ in our RRKM model.

The plotted breakdown diagrams of CHT and Tol and the shifting peak center of the H-loss signal at *m*/*z* = 91 are shown in Figure 10, based on the Gaussian fits (Figure 9). Based on the latest literature mechanisms and our quantum chemical calculations, the isomerization barrier [**2**]‡ between the molecular ions, [**1**] and [**7**], is slightly lower than the simple H-loss leading to [**10**] and the small barrier [**8**]‡ towards [**9**].[97,99-100] Therefore, it is possible to form both the tropylium [**9**] and benzyl [**10**] ions already at the dissociation threshold and the isomerization between the molecular ions has to be incorporated into the statistical rate model. Notably, the model in Figure 17 is too flexible to extract reliable estimates for all parameters based on the experimental results of one sample. Therefore, the same statistical rate model was used to reproduce both the toluene and CHT breakdown diagrams and H-loss peak center positions simultaneously. The following parameters were varied: the two dissociation energies ($Tol^{+\bullet}$ to Bz^+ and $CHT^{+\bullet}$ to Tr^+), the transitional vibrational frequencies for these same two barriers, as well as the isomerization energy difference between Tol and CHT and the isomerization TS height. The vibrational frequencies, the reverse barrier height between the H-loss TS from CHT^+

and the Tr^+ thermochemical limit were fixed at the G4 calculated values. That is, we simultaneously fitted six parameters in a single statistical model to reproduce the measured abundances and dissociation rates of both measurements. The resulting appearance energies are shown in Figure 17, while the best fits to the breakdown curves and TOF peak positions are shown in Figure 10. To determine reasonable error bars for these values within the statistical model, the appearance energies were scanned individually and the rest of the adjustable parameters relaxed until the model stopped reproducing the experimental data acceptably.

Table 1.

Summary of 0 K Appearance Energies (E_0) of Tropylium and Benzyl Ions from CHT and Tol Precursors.

Reactant	Product	
	Tr^+	Bz^+
	E_0 (eV)	E_0 (eV)
CHT	9.520 ± 0.060[a]	9.738 ± 0.082[a]
	9.60[b]	9.74[b]
	9.36 ± 0.020[c]	
	unspecified: 10.3[g], 10.4 ± 0.1[h], 10.73[k]	
Tol	10.978 ± 0.063[a]	11.196 ± 0.080[a]
	11.00[b]	11.15[b]
	10.71 ± 0.03[c]	11.17 ± 0.10[d]
	10.52 ± 0.07[d]	11.1 ± 0.1[f]
	unspecified: 11.43[g], 11.8 ± 0.1[h], 11.8[k], 11.3 ± 0.2[m]	

[a] Experimental values from this study. [b] Based on our quantum chemical calculations, G4 composite method. [c] Traeger *et al.*[85] [d] Bombach *et al.*[90] [f] Lifshitz *et al.*[96-97] [g] Schwell *et al.*[4] [h] Meyerson and Rylander.[105] [k] Hoffman.[141] [m] Field *et al*.[142]

We determined the E_0 of the Tr^+ [**9**] fragment ion to be 9.520 ± 0.060 eV from CHT and 10.978 ± 0.063 eV from Tol. Traeger and McLoughlin[85] measured the appearance energy of the $C_7H_7^+$ ion from 1,3,5-cycloheptatriene to be 9.36 ± 0.02 eV and from toluene to be 10.71 ± 0.03 eV using PIMS and concluded that in both cases the fragment ions at threshold have the tropylium structure. They explained their significantly lower onsets, compared to other studies at that time, as the result of their increased detection sensitivity. Bombach *et al.*[90] have also reported a much lower value, 10.52 ± 0.07 eV from Tol using PEPICO. These literature values appear to be too low, as shown by our self-consistent experimental (9.520 and 10.978 eV) and G4-calculated 0 K appearance energies (9.60 and 11.00 eV, respectively).

The appearance energy of Bz^+ [**10**] was determined to be 9.738 ± 0.082 eV from CHT and 11.196 ± 0.080 eV from Tol. Both are in good agreement with the calculated values of 9.74 and 11.15 eV, respectively (G4). Because the latter value is also used in thermochemical computations (see later) which are in marked disagreement with previous literature values, we computed this onset energy also at the CBS-APNO and W1U levels of theory, which yielded 11.18 and 11.13 eV, respectively, yielding an average *ab initio* value of 11.16 eV, well within the experimental error bars. Bombach *et al.*[90] used PEPICO to measure the E_0 of Bz^+ [**10**] to be 11.17 ± 0.10 eV from Tol, which is in good agreement with our value. An extensive study on the dissociative ionization of toluene was carried out by Lifshitz *et al.*,[96-97] who gave the E_0 of Bz^+ [**10**] 11.1 ± 0.1 eV at 0 K in agreement with later studies[100] and with our experiment.

With the exception of the PEPICO study of toluene by Bombach *et al.*,[90] which was based on RRKM modeling, previous studies relied on a prior assumptions to assign the fragment ion as Tr^+ or Bz^+ when determining the thresholds listed in Table 1. Some forwent them, and reported the appearance energy of the H-loss fragment ion without proposing a fragment ion structure: 10.3 and 11.43 eV by Schwell *et al.*,[4] 10.4 ± 0.1 and 11.8 ± 0.1 eV by Meyerson and Rylander,[105] and 10.73 and 11.8 eV by Hoffman[141] from CHT and Tol, respectively. The discrepancies between different results may arise from the different timescales of the experiments combined with the large kinetic shifts as well as from the different sensitivity of the methods.[97]

Remarkably, the statistical model is more sensitive to the cation isomerization energy than to the appearance energies and $\Delta^{+}_{\mathrm{iso}}E$, was optimized to 0.83 ± 0.02 eV. This ancillary model parameter is in good agreement with the G4 calculated value of 0.80 eV and it can also be used in a thermochemical cycle, together with the literature ionization energies, to obtain the neutral isomerization energy $\Delta_{\mathrm{iso}}E = 1.46 \pm 0.05$ eV. The G4, CBS-APNO, W1U methods yield 1.41_0, 1.47_7, 1.42_9 eV, respectively, *i.e.*, 1.44 ± 0.07 eV on average for this value, confirming the modeling approach and its results.

3.1.8. Thermochemistry

Appearance energies correspond to the thermochemical limit in the absence of a reverse barrier along the dissociation coordinate. Therefore, we can calculate the 0 K enthalpy of formation of the Bz^+ [**9**] cation using the experimentally derived E_0 in this work, 11.196 ± 0.080 eV and the well-known $\Delta_{\mathrm{f}}H^{\ominus}_{0\ \mathrm{K}}$ of toluene, 73.65 ± 0.37 kJ mol^{-1}, and the hydrogen atom, 216.034 kJ mol^{-1}.[143] The obtained value, 937.9 ± 7.7 kJ mol^{-1}, is in good agreement with 935 ± 9 kJ mol^{-1} reported by Bombach *et al.*[90] from their toluene PEPICO study. Baer and co-workers[144] reported 919 ± 5 kJ mol^{-1} at 0 K on the basis of a benzyl bromide experiment. An extensive study on the thermochemistry of benzyl radicals and ions was published by Ellison *et al.*[145] They derived $\Delta_f H^{\ominus}_{0\,K}$ = 925.9 ± 2.5 kJ mol^{-1} for the benzyl ion using AIEs, E_0s, and C–H bond energies available at that time.

The adiabatic ionization energy of the benzyl radical is well known. Its threshold photoelectron spectrum was measured recently by Savee *et al.*,[146] and an IE of 7.252(5) eV was reported. Therefore, using this value and the derived $\Delta_f H^{\ominus}_{0\,K}$ of the Bz$^+$ [**9**] cation, the 0 K enthalpy of formation of the benzyl radical can be calculated as 238.1 ± 7.7 kJ mol^{-1}. We have to note that this value is outside of the range of 226.8 ± 1.9 kJ mol^{-1} taken from the Third Millennium Ideal Gas and Condensed Phase Thermochemical Database for Combustion, which agrees with 225 ± 4 kJ mol^{-1} recommended by Tsang[147] based on three different studies (converted from $\Delta_r H^{\ominus}_{298\,K}$ = 207 ± 4 kJ mol^{-1}; $H^{\ominus}_{298\,K} - H^{\ominus}_{0\,K}$ =18.178).[148] In both systems, a large kinetic shift of over 1.5 eV indicates that the dissociation is slow close to threshold. Although it cannot be ruled out definitely that the RRKM extrapolation is free of systematic errors, it is known to be more prone to overestimating the kinetic shift.[149] Therefore, the discrepancy between our results and the literature benzyl radical heat of formation is unlikely due to the employed statistical model. Furthermore, our experimental E_0 is in good agreement with high-level composite method calculations, which is why we suggest that the literature benzyl radical heat of formation is probably in error.

3.1.9. Conclusions

The unimolecular dissociation of internal energy selected 1,3,5-cycloheptatriene and toluene cations was investigated by imaging photoelectron photoion coincidence spectroscopy using VUV synchrotron radiation. In the studied energy ranges both molecules dissociate by a hydrogen atom loss that leads to the formation of $C_7H_7^+$ ions. Quantum chemical calculations were used to map the potential energy surface connecting the CHT and Tol molecular ions. It was shown that interconversion of the precursor ions happens below the dissociation threshold. Therefore, we modeled both breakdown diagrams simultaneously as a single system by optimizing the 0 K appearance energies, TS frequencies, isomerization barrier and isomer stabilization energies. This first, comprehensive statistical dissociative photoionization model for cycloheptatriene and toluene yielded 0 K appearance energies for Tr^+ of 9.520 ± 0.060 eV from $CHT^{+\bullet}$ [**7**] and 10.978 ± 0.063 eV from $Tol^{+\bullet}$ [**1**], and for Bz^+ 9.738 ± 0.082 eV from $CHT^{+\bullet}$ [**7**] and 11.196 ± 0.080 eV from $Tol^{+\bullet}$ [**1**]. These values are confirmed by G4 calculations, and illustrate that simultaneous statistical analysis of the dissociative photoionization of the two compounds can be used to establish their interconnected isomerization–dissociation energy landscape. The experimental E_0 of benzyl ion was used to calculate its 0 K heat of formation to be 937.9 ± 7.7 kJ mol^{-1}.

3.2. 1-Butanol and 2-Methyl-Propanol

3.2.1. Introduction

Butanols, which can be derived from lignocellulosic materials, are among the most promising alternatives to ethanol as a biofuel or as fuel. Although bioethanol is already widely used as a fuel additive in many countries, butanols, and 1-butanol in particular, have several advantages: lower water uptake, higher energy density, better mixing with common fuels, and better compatibility with traditional engines.[150] With the exception of *tert*-butanol, all butanol isomers can be produced from renewable sources, making them ideal biofuels.[151]

The various isomers of butanol have been the subject of many experimental studies with a focus on their viability as a fuel. These include investigations of their chemistry at high temperatures, relevant to combustion conditions, including species profile,[152-153] laminar flame speed,[154-155] and ignition delay times.[156-159] These studies were carried out in jet stirred reactors,[160-161] flames,[162-164] and pyrolysis.[152-153,165] Numerous kinetic models have been proposed to explain the combustion chemistry of butanol isomers and to fit experimental data for these systems.[159-161,165-166] Although many of these species and elementary reactions involved have been fairly well characterized, thermochemical input parameters are one of the major source of uncertainty in combustion models.[167-169] Unfortunately, the gas phase heats of formation of these butanol isomers remain poorly known. For 1-butanol, NIST[170] reports an averaged value –277 ± 5 kJ mol^{-1} as the 298 K gas phase heat of formation. None of the included 13 measurements are more recent than 1975 and most of these measurements were done on the 298 K heat of formation of 1-butanol in the liquid phase, which was subsequently converted to the gas phase by using the heat of vaporization reported by either Skinner and Snelson[7] or Wadsö.[171] The 298 K gas phase heat of formation of 1-butanol was reported in various other thermochemical databases: –274.9 ± 0.4 kJ mol^{-1} by Pedley *et al*.;[172] –274.4 kJ mol^{-1} by Rosenstock *et al*.;[173] and most recently (in 2006) as –274.6 kJ mol^{-1} by Yaws.[174] However, none of these are based on new experimental data. Isobutanol was less frequently studied and the most recent 298 K gas phase heat of formation is from 1975 by Connett,[175] published as –283.8 ± 0.9 kJ mol^{-1}. This value was determined by using the measured heat of formation of liquid isobutanol by Skinner and Nelson.[7] Rosenstock *et al*.[173] reported this same value, and Pedley *et al*.[172] reported –283.8 ± 0.8 kJ mol^{-1}.

Photoelectron photoion coincidence (PEPICO) spectroscopy coupled with vacuum ultraviolet (VUV) synchrotron radiation enables the measurement of highly accurate thermochemical data of a wide variety of systems.[176-177] In a PEPICO dissociative photoionization experiment, the threshold photoionization signal corresponding to a given photoion *m/z* is recorded together with the kinetic energy analysis of the coincident photoelectrons. Hence, a photoion mass-selected threshold photoelectron spectrum can be obtained, which is advantageous for mixtures. Or, along another dimension of the experimental data, fractional ion abundances can also be plotted as a function of the photon energy in a so-called breakdown diagram. This latter can be modeled with statistical energy distributions and unimolecular rates to extract thermochemical information (fragment ion appearance energies). Our motivation with this study is to revisit the dissociative photoionization of 1-butanol and isobutanol isomers to quantitively understand the ionic dissociation processes.

The dissociation mechanism of the butanol isomer cations and the possible fragment ions have been discussed at length in the literature.[5-6,8,178] McAdoo and Hudson[5] studied the dissociative photoionization H_2O-loss channel of 1-butanol and its deuterated analogs, using photoionization mass spectrometry. Deuterium labeled 1-butanol led to the loss of both HDO and D_2O in varying amounts, based on the original position of the heavy hydrogen isotope. For instance, the greatest percent of heavy water loss was observed when both the methyl and the hydroxyl group was labeled. D_2O elimination was still present when only the hydrogen atoms of the methyl group (CD_3) were replaced with deuterium, evidence of the extensive hydrogen interchange within the molecular ion. These results led McAdoo and Hundson[5] to hypothesize that 1-butanol isomerizes through a hydrogen transfer into the ion-neutral complex $CH_2CH_2CH_2CH_2OH_2^{+\bullet}$ at low energies, which could undergo a series of hydrogen transfer reactions. Unfortunately, the direct transfer of hydrogen would require the existence of a $CH_3CHCHCH_2OH_3^{+\bullet}$ ion, which was proven to be thermochemically unreasonable based on their *ab initio* calculations. Alternatively, they noted that $CH_2CH_2CH_2CH_2OH_2^{+\bullet}$ might isomerize reversibly into a cyclobutane ion–water complex, essentially rendering all hydrogen atoms equal. This would also explain the experimentally observed hydrogen exchange.

Shao *et al.*[8] further studied this H_2O-loss channel using photoelectron photoion coincidence spectroscopy (PEPICO). In the 9.8–10.2 eV photon energy range only the water-loss fragment ion, $C_4H_8^{+\bullet}$ (*m/z* = 56) was detected. They theorized that a complex reaction mechanism must be involved, and that there are two products connected to this H_2O-loss channel: the *trans*-2-butene ion, which is the most stable isomer of $C_4H_8^{+\bullet}$, and the methylcyclopropane ion. The formation of both products involves a rearrangement of the 1-butanol molecular ion to an ion-neutral complex between the 2-butene ion and water and the methylcyclopropane ion and water. They could not determine the energy of these ion-neutral complexes, however theorized that the formation of the methylcyclopropane ion is a slow process, and the formation of the most stable $C_4H_8^{+\bullet}$ isomer is a fast process. Due to the complexity of the dissociation mechanism, they could not analyze the slow rates in any quantitative manner. The appearance energy (E_0) of $C_4H_8^{+\bullet}$ was determined to be 10.18 ± 0.05 eV. This is in agreement with the electron impact value of 10.20 ± 0.05 eV by Bowen and Maccoll,[179] and with the E_0 of 10.19 ± 0.05 eV, determined by Xie *et al.*[178] using photoionization mass spectrometry. Two minor fragment ions were also observed by Xie *et al.*,[178] but with only a small contribution to the total photoionization cross-section of 1-butanol. The E_0 of *m/z* = 42 ion, $C_2H_2O^{+\bullet}$, was determined to be 11.10 ± 0.05 eV, and the E_0 of *m/z* = 31, CH_3O^+, was determined as 11.30 ± 0.05 eV. Both of these are in agreement with the values of 11.23 ± 0.1 eV by Lambdin *et al.*[180] and 11.40 ± 0.06 eV by Selim and Helal,[181] respectively.

The dissociative photoionization mechanisms of isobutanol have also been extensively studied.[6,8,178] Shao *et al.*[8] found these to be even more complex than that of 1-butanol. Four major fragments were detected in the photon energy range of 9.6–12.4 eV, in agreement with the findings of Xie *et al.*,[178] out of which the first two, *m/z* = 56 and *m/z* = 33, were slow dissociation processes. The water loss channel, that is *m/z* = 56, $C_4H_8^{+\bullet}$, is weak and quickly overtaken by the other slow channel, the formation of $CH_3OH_2^+$ (*m/z* = 33). Shao *et al.*[8] suggested that the water loss channel proceeds *via* the formation of a methylcyclopropane-water complex, which is the only contributor to this dissociation. The appearance energy of the *m/z* = 56 ion was given as 10.33 ± 0.03 eV. In agreement with this, Xie *et al.*[178] found that the $C_4H_8^+$ has only a minor contribution to the absolute photoionization cross-section of isobutanol, and determined an E_0 of 10.32 ± 0.05 eV. The *m/z* = 33 channel, $CH_3OH_2^+$, is the major fragment in the study of both Xie *et al.*[178] and Shao *et al.*[8] with appearance energies of 10.36 ± 0.05 eV and 10.43 ± 0.03 eV, respectively. The other two fragment ions detected are $C_3H_6^{+\bullet}$ (*m/z* = 42) and $C_3H_7^+$ (*m/z* = 43). These are consistent with the loss of methanol and the loss of CH_2OH, respectively. The *m/z* = 42 channel is the lower energy path, which requires a rearrangement of the molecular ion, but it is overtaken at higher energies by the $C_3H_7^+$ channel, formed by direct C–C bond cleavage in the parent ion. Appearance energies of $C_3H_6^{+\bullet}$ were determined to be 11.00 ± 0.03 eV and 10.81 ± 0.05 eV, and of $C_3H_7^+$ was found to be 11.28 ± 0.05 eV and 11.00 ± 0.05 eV, by Shao *et al.*[8] and Xie *et al.*,[178] respectively. Although Xie *et al.*[178] noted that their values are consistently lower than that of Shao *et al.*'s,[8] they gave no explanation on what may cause the discrepancy.

In this study, we investigated the dissociative photoionization of two internal energy selected butanol isomer cations using imaging photoelectron photoion coincidence (iPEPICO) spectroscopy at the Swiss Light Source (SLS). These two ionic species (1-butanol and isobutanol cations) dissociate into the same fragment ions but the relative abundance of these fragments differs widely between the two very similar species. Hence, in addition to generating new experimental thermochemical data or confirming existing thermochemistry, our analysis shall offer much insight into the dissociation mechanisms that may be qualitatively different between the two systems, despite their high similarity.

3.2.2. Experimental and Theoretical Approach

1-Butanol (99.7%) and 2-methyl-1-propanol (or isobutanol, 99.5%) were purchased from Sigma Aldrich and were used without further purification. Both room temperature samples were introduced through an effusive inlet into the ionization chamber of the iPEPICO endstation[119] at the VUV beamline[124] of the Swiss Light Source. The pressure of the experimental chamber was set to 1–3 x 10^{-6} mbar. VUV synchrotron radiation was used to ionize the samples in a 2 x 2 mm interaction region with a photon energy resolution of 3–5 meV. Photoions and photoelectrons were extracted in opposite directions from the ionization region, using a constant 120 V cm^{-1} electric field. Photoelectrons were velocity-map-imaged onto a Roentdek DLD40 position-sensitive delay-line detector from which two regions were utilized. First, threshold electrons were focused to the center of the detector, together with kinetic energy electrons with no off-axis momentum. Second, hot electrons with an off-axis momentum were detected in an arbitrarily defined ring around the center spot. Hot electron contribution to the threshold photoelectron signal was removed by subtracting the average signal counts in the ring region from that of the center signal using an appropriate scaling factor to account for differences in area.[41] Photoions were mass analyzed by a two-stage Wiley-McLaren[125] time-of-flight (TOF) mass spectrometer and were spaced-focused onto a Jordan TOF C-726 microchannel plate detector. The start signal for the TOF analysis of the photoions is provided by detection of the corresponding photoelectron in a multiple-start/multiple-stop coincidence data acquisition scheme.[32] Ion residence times are on the order of microseconds due to the long extraction region with low extraction field. If a molecular ion dissociates in this extraction region, the time-of-flight of the resulting fragment ion will be somewhere between the nominal TOF of the parent ion and the fragment ion and, therefore, the peak corresponding to a slowly dissociating ion will exhibit a broad, quasi-exponential shape toward higher *m/z* ratios, indicative of the unimolecular rate constant of dissociation.[29,117] Dissociation rates of $10^3 – 10^7$ s^{-1} can be measured and fit to the modeled rates, quantifying the kinetic shift[182] and providing a reliable extrapolation to the dissociation threshold.

3.2.3. Statistical Modeling

The experimental breakdown diagram and the threshold TOF mass spectra with asymmetric ion peak shapes were modeled using rigid activated complex Rice–Ramsperger–Kassel–Marcus (rac-RRKM) theory.[117,135] These calculations were used to extract the experimental rate constants from the experimental time-of-flight data by fitting the calculated peak shapes to the quasi-exponential asymmetric fragment ion peaks. For this purpose, we employed statistical thermodynamics and statistical rate theory to calculate the molecular ion's internal energy distribution from the thermal energy of the neutral sample, the dissociation rate constants of the dissociating ions, from which ion branching ratios and theoretical TOF spectra were calculated and compared to the experimental data. The unimolecular rate constants, $k(E)$, were extracted by equation (24) described in Chapter 2.3.2. on the RRKM theory. The sums and densities of states were calculated using harmonic vibrational frequencies by the Beyer–Swinehart direct count algorithm.[183]

There are many cases when the molecular ion undergoes reversible isomerization prior to dissociation.[19,184-190] The product ions can be formed from either the parent ion or from its isomer. Solutions of the rate equations for a two-well system (Figure 8) are provided in Chapter 2.3.5. In short, in the case of two molecular ion isomer structures, each fragment ion is formed with two apparent rate constants, k_{fast} and k_{slow}, which can manifest themselves in the TOF spectra as double-exponential asymmetric daughter ion peaks. Therefore, such features in the experimental TOF spectra indicate that isomerization might be at play.

3.2.4. Quantum Chemistry

The analysis of the experimental data and the statistical modeling was aided by *ab initio* calculations, using the Gaussian 09 suite of programs.[128] Rotational constants and harmonic vibrational frequencies at the B3LYP/6-311++G(d,p) level of theory were extracted to calculate the thermal energy distribution of the neutral precursor molecules, numbers and densities of states for the rate equation (1), and stationary point energies for examining the possible isomerization and dissociation pathways.[117] Stationary points for the most likely dissociative photoionization pathways and ion rearrangements were refined using the G4 composite method.[131] Transition state (TS) structures were located using constrained optimizations (for loose transition states with no saddle point) and synchronous transit-guided quasi-Newton calculations[129-130] and verified using intrinsic reaction coordinate (IRC) calculations. Further composite method calculations (CBS-QB3,[133-134] CBS-APNO,[132] and W1U[81]) have also been carried out on the ionization energy of 1-butanol and isobutanol.

3.2.5. Results and Discussion

3.2.5.1. Statistical modeling of the dissociative photoionization processes. PEPICO time-of-flight mass spectra of internal energy selected 1-butanol and isobutanol ions were collected in the 10.0–13.2 eV photon energy range. We found that the dissociative photoionization of 1-butanol and isobutanol both generate fragment ions with the following mass-to-charge ratios: *m/z* = 31, 33, 41, 42, 43, and 56. The most likely fragmentation processes leading to these ions are shown in Scheme 2.

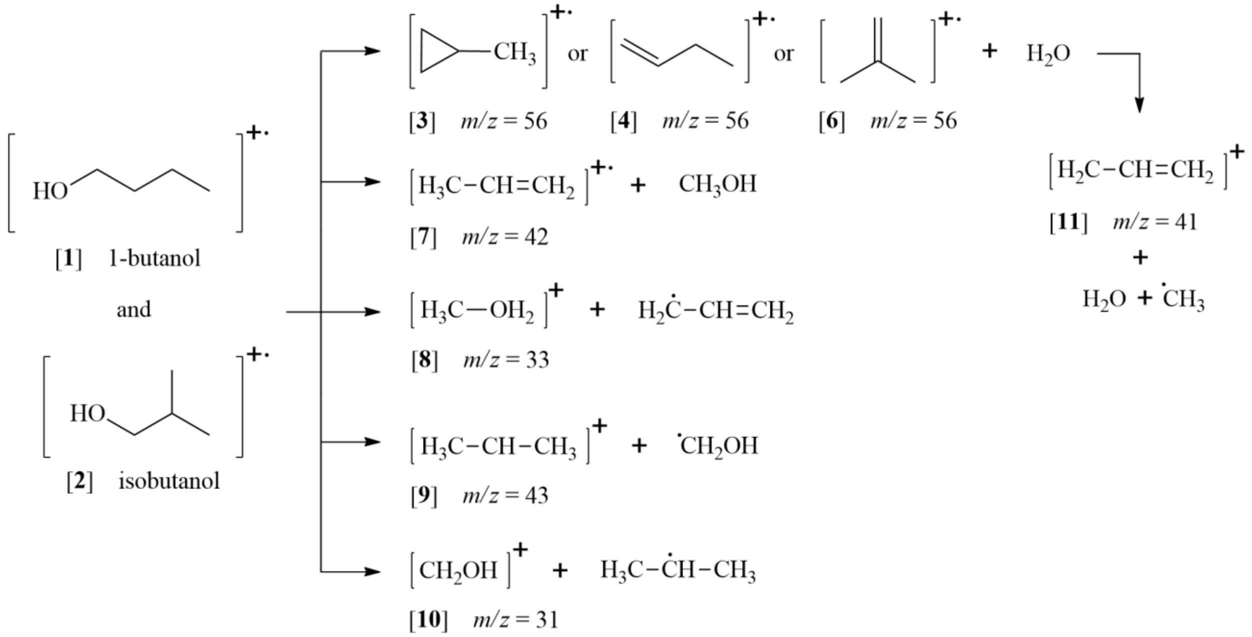

Scheme 2. General dissociation pathways of 1-butanol and isobutanol in the 10.0–13.2 eV photon energy range.

3.2.5.2. 1-butanol. Reported adiabatic ionization energies (AIE) of 1-butanol vary between 9.95–10.10 eV, as listed in Table 2. (Holmes and Lossing,[191] Shao *et al.*,[8] Cocksey *et al.*,[192] Watanabe *et al.*,[193] Xie *et al.*[178]) Our PEPICO measurement, however, show significant dissociation already at 10.0 eV, which might imply that these literature values are overestimated. For reasons why this might indeed be the case, see the analogous section under isobutanol, *vide infra*. Hence, we calculated a theoretical 1-butanol AIE at the G4,[131] CBS-QB3,[133-134] CBS-

APNO,[132] and W1U[81] composite levels of theory (9.86_1, 9.86_3, 9.83_1, and 9.88_7 eV, respectively). All these calculated values are in remarkably good agreement with each other but are lower than the literature values. Therefore, their average of 9.86 eV most likely represents a reliable theoretical estimate for the 1-butanol AIE and we used this value to calculate the internal energy distribution of the 1-butanol molecular ion in the statistical model. It is important to note here that since, in the PEPICO experiment, we directly measure the appearance energy of a fragment ion, variations in the AIE only indirectly affect the results from the statistical model.

Table 2.

Summary of adiabatic ionization energies (AIE) and 0 K appearance energies (E_0) for the two butanol isomer cations and their fragment ions.

Species	E_0 (eV) Experimental[a]	AIE or E_0 (eV) Computed (G4)[a]	AIE or E_0 (eV) Literature
1–C_4H_9OH [**1**]		[b]9.86 ± 0.05	[c]9.99 ± 0.05
m/z = 74			[d]10.09 ± 0.02
			[e]9.95 ± 0.05
CH_3–c–$C_3H_5^{+\bullet}$ [**3**]	10.347 ± 0.015	10.42	[c]10.18 ± 0.05
CH_2=CH–$C_2H_5^{+\bullet}$ [**4**]	10.95 ± 0.15		[f]10.20 ± 0.05
m/z = 56			[e]10.19 ± 0.05
CH_3–CH=$CH_2^{+\bullet}$ [**7**]	10.942 ± 0.040	10.87	[e]11.10 ± 0.05
m/z = 42			[g]11.23 ± 0.1
CH_3–OH_2^+ [**8**]	10.738 ± 0.090	[j]10.51	
m/z = 33			
CH_3–CH–CH_3^+ [**9**]	11.104 ± 0.030	11.00	
m/z = 43		[j]10.99	
CH_2OH^+ [**10**]	11.104 ± 0.030	[j]11.05	[e]11.30 ± 0.05
m/z = 31			[h]11.40 ± 0.06
CH_2=CH–CH_2^+ [**11**]	11.6 – 11.7	11.63	
m/z = 41			
i–C_4H_9OH [**2**]		[b]9.66 ± 0.05	[c]10.02 ± 0.05
m/z = 74			[d]10.09 ± 0.02
			[e]9.95 ± 0.05
$CH_3C(=CH_2)CH_3^{+\bullet}$ [**6**]	10.566 ± 0.050	10.50	[c]10.33 ± 0.03
m/z = 56			[e]10.32 ± 0.05
CH_3–CH=$CH_2^{+\bullet}$ [**7**]	10.723 ± 0.020	[j]10.77	[c]11.00 ± 0.03
m/z = 42			[e]10.81 ± 0.05
CH_3–OH_2^+ [**8**]	10.612 ± 0.020	[j]10.62	[c]10.43 ± 0.03
m/z = 33			[e]10.36 ± 0.05
CH_3–CH–CH_3^+ [**9**]	10.970 ± 0.050	11.09	[c]11.28 ± 0.05
m/z = 43			[e]11.00 ± 0.05
CH_2OH^+ [**10**]	11.11 ± 0.20	11.15	
m/z = 31			
CH_2=CH–CH_2^+ [**11**]	11.6 – 11.9	11.73	
m/z = 41			

[a]This work. [b]Average computed AIE at the G4, CBS-QB3, CBS-APNO, and W1U levels. [c]Shao *et al.*[8] [d]Cocksey *et al.*[192] [e]Xie *et al.*[178] [f]Bowen and Maccoll.[179] [g]Lambdin *et al.*[180] [h]Selim and Helal.[181] [j]G4-calculated thermochemical limit.

The experimental and modeled breakdown diagrams of 1-butanol are shown in Figure 18, along with selected PEPICO TOF spectra in Figure 19. Below the photon energy of 10.8 eV, only the molecular ion, $CH_3CH_2CH_2CH_2OH^{+\bullet}$ (*m/z* = 74) [**1**], and the first fragment ion $C_4H_8^{+\bullet}$ (*m/z* = 56, [**3**]), consistent with the loss of a water, were detected. This is in line with earlier photoionization studies, which also observed a H_2O-loss channel. Based on the asymmetric fragment ion TOF peak shapes, shown in Figure 19, this dissociation pathway is “slow” near threshold; that is, the molecular ions are metastable on the time scale of the experiment. The *m/z* = 56 fragment ion can be formed *via* a hydrogen atom transfer to the OH group from one of the carbon atoms. In order to determine which hydrogen transfer pathway is responsible for this dissociation channel, extensive quantum-chemical calculations (with G4 energies) were carried out. These results are discussed in the Potential Energy Surface section (*vide infra*) and shown in Figure 22. In short, our calculations show that the hydrogen transfer processes proceed through transition states 0.14 to 1.42 eV above the molecular ion (10.00 to 11.28 eV relative to the neutral precursor), leading to lower energy isomeric structures that feature more and more loosely attached ion$\cdots H_2O$ moieties, consistent with earlier literature findings.[5-6] The first step in the α-carbon hydrogen shift involves a transition state that is at 11.28 eV (*relative to the neutral precursor*), much too high to be relevant at threshold. H-atom transfer from the β-carbon features a similarly too high saddle point at 10.70 eV. However, for a γ-carbon H-atom shift, the CH_2OH moiety can first rotate closer to the γ-carbon and the hydrogen transfer happens through a transition state at 10.42 eV. The subsequent loss of water produces the methylcyclopropane fragment ion with a calculated thermochemical limit of 9.87 eV. The δ-carbon hydrogen shift and subsequent water-loss follows the well-known McLafferty rearrangement mechanism[194] forming cyclobutane with an effective transition state 0.40 eV higher than the γ-carbon H-shift pathway.

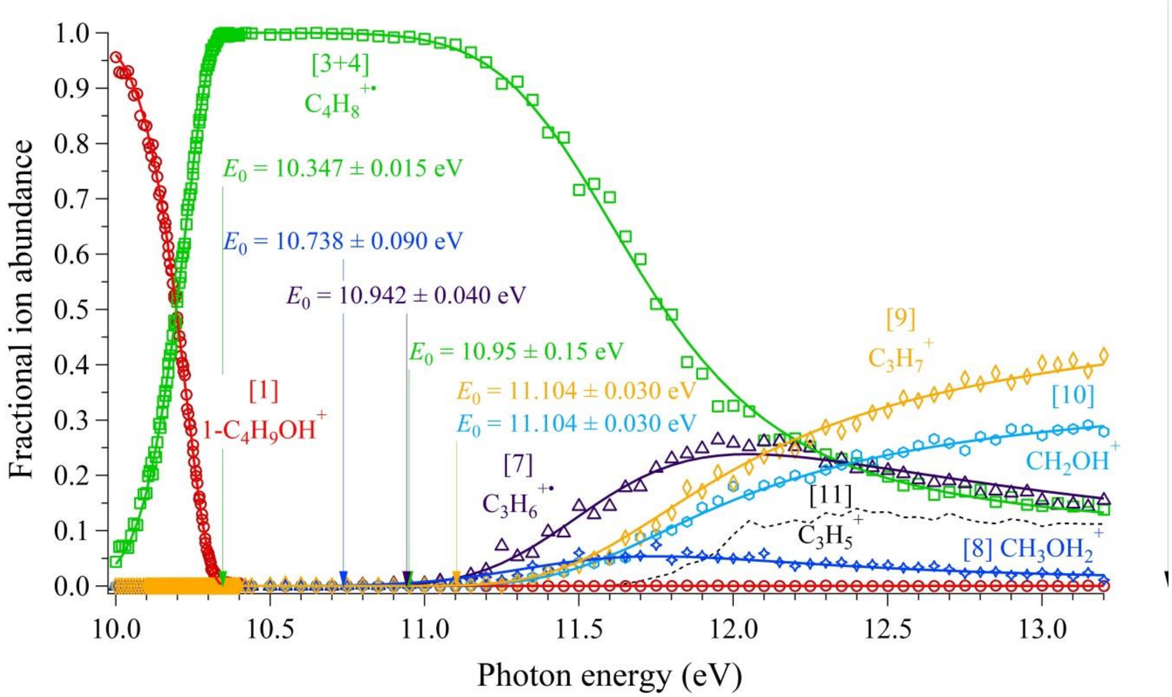

Figure 18. Breakdown diagram for 1-butanol in the 10.0–13.2 eV photon energy range. Polygons are experimentally measured ion abundances and the solid lines are the best-fit modeling of the data (*see text*). The dashed line shows the fractional abundance of the *m/z* = 41 ion, the consecutive dissociation of the *m/z* = 56 ion which was not separated out in the statistical model and, therefore, the green polygons and line stand for the sum of the *m/z* = 56 and 41 ions above 11.6 eV photon energy.

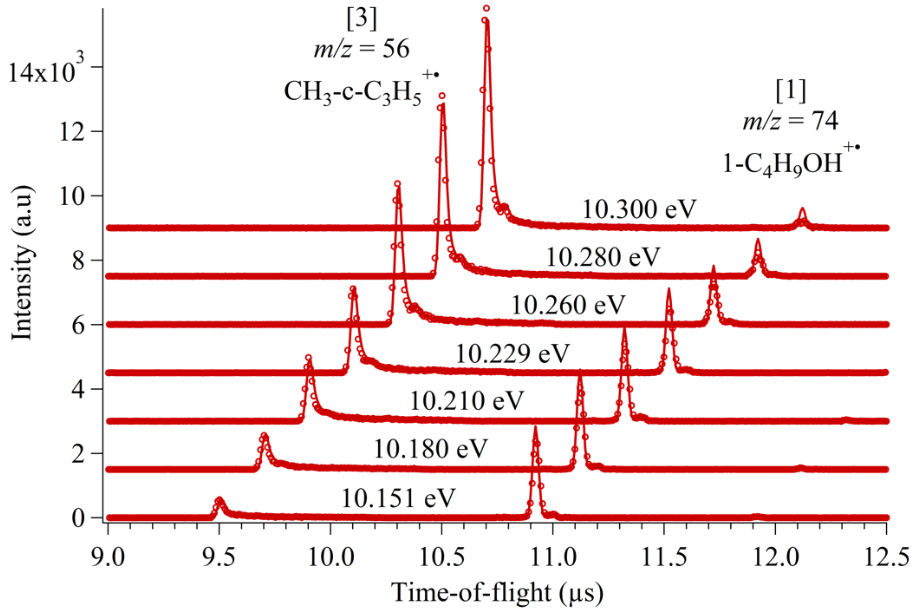

Figure 19. Selected threshold photoionization TOF distributions of 1-butanol. Open circles are the experimentally measured PEPICO TOF spectra and lines are the best fit modeling of the data.

To discuss the intricacies of the ionic dissociation mechanism, it is essential to understand the role of various isomeric structures. As mentioned earlier, an asymmetric double (or triple) exponential fragment ion peak shape is a revealing sign that more than one isomeric structure plays an active role in the dissociation process.[19,117] Furthermore, only using one parent ion structure in the statistical modeling did not result in an acceptable fit to the experimental rate curve (manifested in the asymmetric TOF distribution data). Therefore, the statistical model includes the molecular ion reversibly isomerizing into a methylcyclopropane¨water ion-neutral complex isomeric structure and with two transition states: a tight TS reversibly connecting the 1-butanol molecular ion with the isomer structure and a loose TS serving as the exit channel into products. In fitting the model's output to the experimental TOF distributions and breakdown curves, we optimized the barrier height leading to dissociation and the lowest five frequencies of the corresponding loose TS structure, and the height of both the forward and reverse isomerization barriers. The isomerization transition state frequencies were calculated at the B3LYP level and were kept unchanged in the model. In the best fit of the data, the isomerization barrier height and the isomer stabilization energy (both relative to the molecular ion) were found to be at 0.44 eV and –0.19 eV, respectively. With this model, the appearance energy of the water-loss m/z = 56 (methylcyclopropane) fragment ion (E_0) was determined to be 10.347 ± 0.015 eV. This is in reasonable agreement with the G4 value of 10.42 eV and suggests that the lowest-energy water-loss channel of 1-butanol leads to the formation of methylcyclopropane ion. This is also in line with the hypothesis of Shao *et al.*,[8] who assumed the formation of two $C_4H_8^{+\bullet}$ isomer cations: *trans*-2-butene and methylcyclopropane. Although energetically *trans*-2-butene is the most stable $C_4H_8^+$ isomer, our quantum chemical calculations revealed no low-energy pathways to it and the most probable $C_4H_8^{+\bullet}$ structure is methylcyclopropane.

Beyond 11 eV, four additional parallel dissociation channels open up at approximately the same photon energy: $C_3H_6^{+\bullet}$ (m/z = 42, [**7**]) with a methanol-loss, $CH_3OH_2^+$ (m/z = 33, [**8**]) from loss of C_3H_5, $C_3H_7^+$ (m/z = 43, [**9**]) from loss of CH_2OH, and CH_2OH^+ (m/z = 31, [**10**]) from C_3H_7-loss. Two of these dissociation channels, m/z = 33 and 43, were not reported in earlier studies. These four channels were modeled in parallel with the m/z = 56, using calculated frequencies for the loose transition states as starting points and fitting both the transitional TS frequencies and the appearance energies to the experimental breakdown curves.

The formation of the $C_3H_6^{+\bullet}$ (m/z = 42, [**7**]) and the $CH_3OH_2^+$ (m/z = 33, [**8**]) fragment ions once again require rearrangement of the 1-butanol cation prior to dissociation. Based on our quantum chemical calculations, the most likely structure of $C_3H_6^{+\bullet}$ is $CH_3CHCH_2^{+\bullet}$, formed by a γ-carbon hydrogen transfer to the α-carbon followed by the loss of a CH_3OH fragment. The calculated transition state for this pathway lies at 10.87 eV, in reasonable agreement with the experimentally derived appearance energy of 10.942 ± 0.040 eV. Xie *et al.*[178] reported a slightly higher value, 11.10 ± 0.05 eV from their photoionization mass spectrometry measurement but, strangely, they identified the *m/z* = 42 ion as ketene, $C_2H_2O^{+\bullet}$. They provided no explanation, however, on the formation of ketene ion from 1-butanol molecular ion, which would require a C_2H_8 loss – mayhap a couple of molecules with bovine gastrointestinal significance. The formation of $CH_3OH_2^+$ requires even more rearrangements. According to our calculations, the β-carbon hydrogen first transfers to the OH group, then the water and the methyl group forms the protonated methanol while the $CH_2CHCH_2^\bullet$ (allyl) fragment is lost. The experimentally derived E_0 is 10.738 ± 0.090 eV, which could not be corroborated with a G4 transition state energy as optimizations of this TS structure have not converged.

The next two fragmentation pathways correspond to a complementary pair: $C_3H_7^+$ (*m/z* = 43, [**9**]) through the loss of CH_2OH, and CH_2OH^+ (*m/z* = 31, [**10**]) through the loss of C_3H_7. If the appearance energies of these two channels correspond to their respective thermochemical limits, the difference in the E_0 values has to be equal to the ionization energy difference of the two neutral fragments, i.e. C_3H_7 and CH_2OH, for which the ATcT value is 0.110 ± 0.007 eV. However, the experimental 0 K appearance energies are equal within error bars at 11.104 ± 0.030 eV, suggesting that these reactions proceed through a common transition state, slightly above the thermochemical limits. This is not surprising since there is a necessary H-shift in order to form the most stable C_3H_7 isomer neutral or ion, CH_3CHCH_3. Calculated thermochemical limits of 10.99 and 11.05 eV for the formation of the $CH_3CHCH_3^+$ and CH_2OH^+ fragment ions, respectively, are indeed below the experimental onset. We identified their common transition state at 11.00 eV, which is only slightly higher than the thermochemical threshold of the isopropyl ion. Previously, Xie *et al.*[178] measured a somewhat higher value, 11.30 ± 0.05 eV for the appearance energy of the *m/z* = 31 ion, which they identified as CH_3O^+. This is most likely another oversight as this structural isomer of CH_2OH^+ is 3.5 eV less stable, based on ATcT heat of formation values.

Finally, a sixth channel opens up around 11.7 eV, consistent with $C_3H_5^+$ (*m/z* = 41, [**11**]). Since the formation of this ion requires an overall loss of CH_5O, it must be a product of sequential steps; conveniently, a methyl loss dissociation from the first fragment ion, $C_4H_8^{+\bullet}$ (*m/z* = 56). Our PEPICO modeling code is equipped to handle complex dissociation schemes with two isomer ions, several parallel dissociation channels and consecutive dissociations from one of those. However, according to theory, the situation is even more complicated here, due to the multiple possibilities on forming the *m/z* = 56 fragment ion (*vide supra*).[117] Therefore, we were unable to determine a reliable experimental value for the appearance energy of the *m/z* = 41 ion and, instead, its experimental ion abundances were summed into its parent ion and they were modeled together as one channel. Then, the high energy tail of this combined breakdown curve could not be reproduced with a single *m/z* = 56 channel, which finding is in line with the quantum-chemical calculations but complicates the picture of how the *m/z* = 41 fragment ion came about. Therefore, a more complex model was built with two parallel $C_4H_8^{+\bullet}$ channels and this model provided an excellent fit to the combined *m/z* = 56 and *m/z* = 41 curve. However since, according to the model, the contribution of the second H_2O-loss pathway never amounts to more than 15%, the model is not very sensitive to this second *m/z* = 56 appearance energy, for which 10.95 ± 0.15 eV is our best estimate. This value is not far from the calculated transition state energy of 10.70 eV leading to the formation of the 1-butene fragment ion and while, from the experimental data alone, it is not possible to firmly address the energetics of this second *m/z* = 56 channel, its existence is quite clear.

3.2.5.3. Isobutanol. The AIE of isobutanol was reported to be between 9.95 and 10.12 eV with typical uncertainties of 0.05 eV.[8,178-179,191-192] Similarly to the case of 1-butanol, we calculated the isobutanol AIE at the G4,[131] CBS-QB3,[133-134] CBS-APNO,[132] and W1U[81] composite levels of theory (9.65_6, 9.68_6, 9.63_3, and 9.68_7 eV, respectively). Determining the precise location of an onset of photoionization mass spectrometry (PIMS) data involves extrapolation to the baseline with a straight line. The extrapolated energy depends on which region of the spectrum is fitted as most photoionization plots are curved. Photoelectron spectroscopy is not sensitive to reverse barriers or slow reactions unlike PIMS but weakly overlapping Franck-Condon factors could shift the determined AIE to a higher value. This has been shown for ethanol where the reported AIE values were found to be significantly off from the true value.[126] A similarly large discrepancy but with an opposite sign has been observed between the previously published and the true AIE of diethyl ether.[118] As the precision of our calculated values is impressive, and they are significantly lower than the experimental data found in the literature it is possible that literature values do not correspond to the adiabatic value. Therefore, we used the 9.66 ± 0.05 eV in the statistical modeling of the isobutanol PEPICO data.

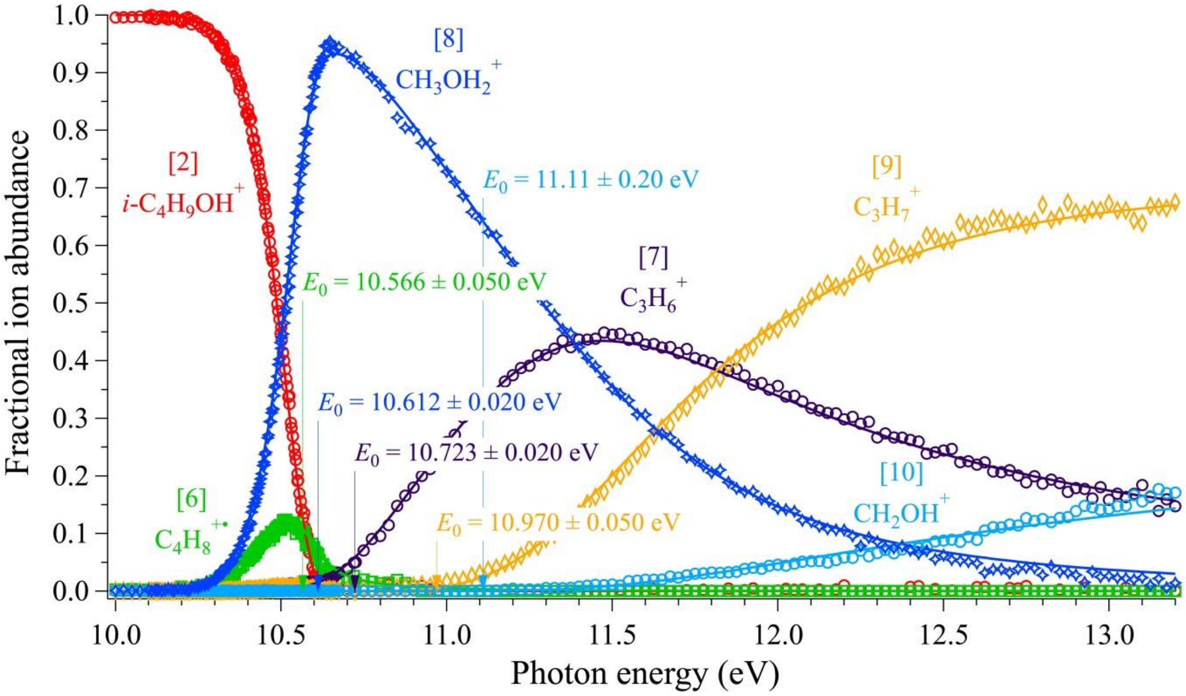

Figure 20. Breakdown curves for isobutanol in the 10.0–13.2 eV photon energy range. Solid polygons correspond to experimental data points, whereas continuous lines are modeling results. The *m/z* = 41 channel is not included here because of its low abundance.

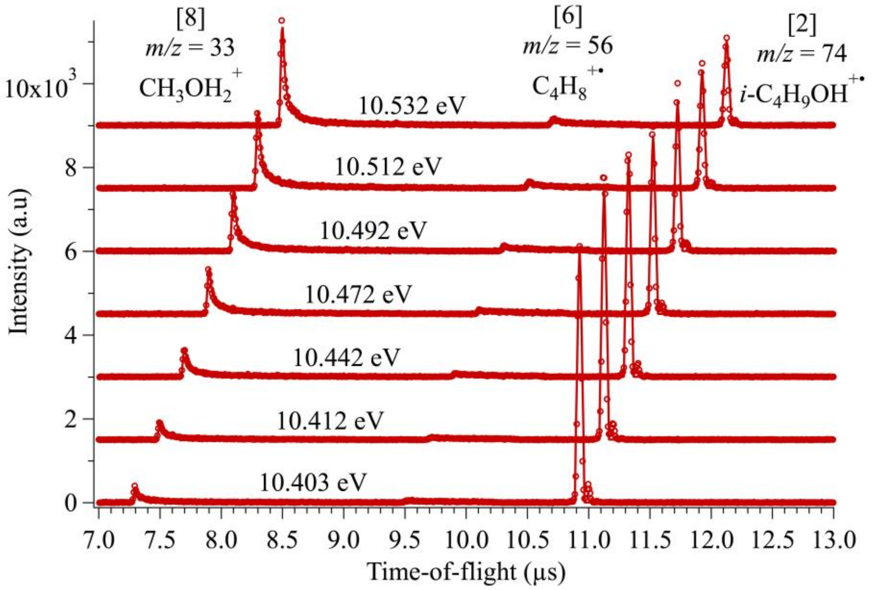

Figure 21. Sample threshold photoionization TOF distributions of isobutanol. Open circles are the experimentally measured PEPICO mass spectra and lines are the best fit modeling of the data.

The breakdown diagram of isobutanol is shown in Figure 20 and selected PEPICO time-of-flight spectra are shown in Figure 21. Compared to 1-butanol, the breakdown diagram for isobutanol consists of the same six fragment ions, but with the notable difference that the lowest energy H_2O-loss channel is no longer the only low-energy channel. Similarly to 1-butanol, two dissociation channels, the formation of *m/z* = 31 and 41, were not reported in the literature before.

The first channel involves a loss of water to produce $C_4H_8^{+\bullet}$ (*m/z* = 56, [**3**,**4**,**6**]). In contrast to 1-butanol, the water-loss channel is much less abundant and is quickly overtaken by the loss of $C_3H_5^{\bullet}$ to produce $CH_3OH_2^+$ (*m/z* = 33, [**8**]) at nearly the same photon energy. This is consistent with the findings of Shao *et al*. and Xie *et al*.[8,178] The asymmetric fragment ion TOF peaks of both of these ions are indicative of slow dissociation and their double-exponential shape implies isomerization of the molecular ion, as also noted by Shao *et al*.[8] To make sure that this is indeed the case, we first assumed direct dissociation for both dissociation pathways in the statistical model, which resulted in an unacceptable fit even when the transition states were set unreasonably tight. Therefore, in the model that we used to successfully fit the experimental data, isomerization was also included, similar to the 1-butanol model. In this case, as discussed in detail in the computational section, a hydrogen atom shifts from the methine group to the hydroxyl through a reverse barrier at 10.50 eV and the resulting water is coordinated in a bridging position. Water is lost from this complex to form isobutene [**6**] fragment ion. From the best fit to the experimental data, a 0 K appearance energy of 10.566 ± 0.050 eV was obtained, which is in reasonable agreement with our G4 calculated value for the hydrogen transfer transition state. These results are in contrast to Shao *et al*.,[8] who suggested that methylcyclopropane ion is the only contributor to the *m/z* = 56 channel. However, methylcyclopropane ion [**4**] could also be formed if the hydrogen is transferred from one of the methyl groups, then the two CH_2 moiety close the three-membered ring. According to our calculations, the distance of these aforementioned groups is approximately 2.5 Å and it proceeds through a reverse barrier at 10.64 eV. The $CH_3OH_2^+$ [**8**] fragment ion comes from a different ion-neutral complex, where one of the methyl hydrogen is transferred to the hydroxyl group, then the other methyl group migrates to the water moiety to form the protonated methanol fragment ion. The 0 K appearance energy of $CH_3OH_2^+$ was determined to be 10.612 ± 0.020 eV, which is in good agreement with the G4 thermochemical limit of 10.62 eV, indicating a submerged barrier corresponding to the methyl migration.

The next fragment ion, $C_3H_6^{+\bullet}$ (m/z = 42, [**7**]) is formed by methanol loss from the molecular ion and quickly overtakes both previous channels and accounts for the highest ion abundance between 11.4 and 11.9 eV. To rationalize the methanol loss, the simplest explanation is that the hydroxyl group shifts to one of the methyl groups, which induces the barrierless loss of CH_3OH neutral fragment, forming a propene, $CH_3CHCH_2^{+\bullet}$ cation in the process. Most likely, the roaming OH transition state, with an ill-defined geometry, lies below the dissociation threshold as the experimental E_0 of 10.723 ± 0.020 eV is in good agreement with the calculated thermochemical limit of 10.77 eV.

The abundance of the $C_3H_7^+$ (m/z = 43, [**9**]) ion, formed by direct CH_2OH loss, steadily rises after ~11 eV and becomes the dominant channel above 12 eV. Contrary to 1-butanol, where an internal hydrogen shift was required to form the more stable CH_3CHCH_3 structure, it is directly available from the isobutanol molecular ion by a simple bond rupture. The experimental 0 K appearance energy was found to be 10.970 ± 0.050 eV, slightly lower than the G4-calculated thermochemical limit of 11.09 eV but in reasonable agreement with the ATcT value of 11.035 ±

0.010 eV. Similarly to the case of 1-butanol, the corresponding heterolytic bond breakage is also possible, and the CH_2OH^+ (*m/z* = 31, [**10**]) fragment ion appears as a minor dissociation channel at 11.2 eV, with a maximum of 15% abundance by 13.2 eV. The branching ratios between these two complementary channels are in contrast to our observations for 1-butanol, where the abundances of these channels are comparable: $C_3H_7^+$ [**9**] is 40%, and CH_2OH^+ [**10**] reaches its maximum just below 30%. This is another argument for a qualitatively different dissociation mechanism between the two systems and the common transition state that both dissociations go through is responsible for the similar branching ratios between the homolytic and heterolytic cleavage in the 1-butanol ion. From isobutanol, the experimental E_0 of CH_2OH^+ was determined to be 11.11 ± 0.20 eV, in agreement with the ATcT and G4 calculated values of 11.145 ± 0.011 eV and 11.15 eV, respectively.

The final dissociation channel from isobutanol ions in the studied photon energy range is the consecutive formation of the $C_3H_5^+$ (*m/z* = 41, [**11**]) cation by a methyl loss from *m/z* = 56, with a maximum intensity of 5%. The abundance of this channel is so small that it could not be modeled reliably and it was excluded from the model. The visual appearance energy of $C_3H_5^+$ is between 11.6 and 11.9 eV, in agreement with the calculated G4 E_0 of 11.73 eV.

3.2.6. Calculated Dissociation Mechanisms

Quantum chemical calculations were carried out to assist in the identification of the unimolecular dissociation pathways and quantify their energetics. Stationary points that are likely to play a role in the ionic dissociation processes were optimized at the B3LYP/6-311G++(d,p) level of theory. The stationary point energies were refined using G4[131] composite method (Figures 23, 25, and 27). All G4 energies are reported relative to the corresponding neutral butanol isomers.

3.2.6.1. 1-Butanol. The first dissociation channel of 1-butanol molecular ion [**1**] leads to the formation of $C_4H_8^{+\bullet}$ [**3**–**6**] by a water loss that, as we discussed in the previous section, requires the rearrangement of the molecular ion. We explored hydrogen atom transfers to the OH group from the α-, β-, γ-, and δ-carbon atoms. The α-carbon hydrogen shift proceeds through a transition state that is at 11.28 eV, well above the experimental E_0 of 10.347 ± 0.015 eV. The hydrogen on the β-carbon can also be transferred in a single step through a transition state at 10.70 eV, leading to an ion-molecule complex between water and a 1-butene ion with an O···C distance of 2.279 Å. This complex is 0.39 eV more stable than the 1-butanol molecular ion itself and water is lost *via* a barrierless dissociation, forming 1-butene.

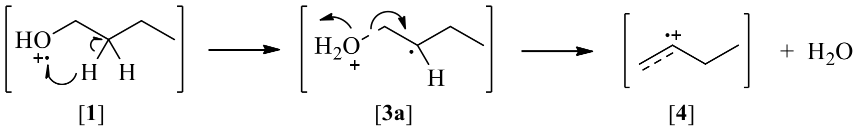

Scheme 3. Formation of 1-butene ion (*m/z* = 56) *via* a β-hydrogen transfer, followed by water loss.

In the case of a H-atom shift from the γ-carbon, the CH_2OH moiety rotates closer to this site and the hydrogen transfer proceeds through a barrier of 10.42 eV, while the carbon chain assumes a cyclic structure. Then, through a second saddle point at 9.87 eV, water is lost, resulting in a methylcyclopropane ion at a G4 thermochemical limit of 9.87 eV. Similarly to the β-carbon transfer, the ion-neutral complex, with an O···C distance of 2.431 Å, is energetically more stable than the parent ion, by 0.35 eV.

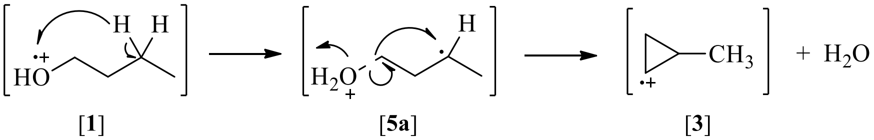

Scheme 4. Formation of methylcyclopropane ion (m/z = 56) *via* a γ-hydrogen transfer followed by water loss.

As a fourth possible pathway, the δ-carbon hydrogen shift involves the classic McLafferty rearrangement mechanism.[194] To form the six-membered ring structure, the CH_2OH moiety of 1-butanol ion is rotated to an H–O–C_α–C_β dihedral angle of 92° through a barrier of 10.00 eV and the actual hydrogen transfer occurs *via* a transition state at 9.90 eV. The α- and γ-carbon atoms get closer to form the cyclobutane ring through a TS at 10.82 eV. While the barrier to the cyclobutane-water complex is lower than the transition states mentioned above, this ion-molecule complex is actually higher in energy than the 1-butanol cation by 0.18 eV.

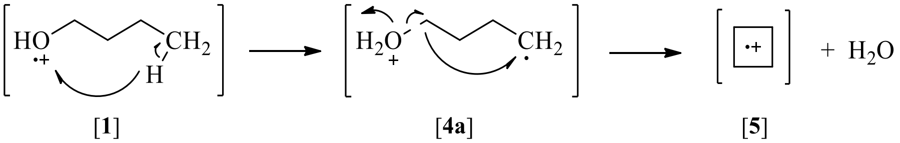

Scheme 5. Formation of cyclobutane ion (m/z = 56) *via* a δ-hydrogen transfer followed by water loss.

From here, water is directly lost with a thermochemical limit of 10.44 eV, which is energetically less feasible than the methylcyclopropane fragment ion channel. Because of this, the m/z = 56 ion is most likely methylcyclopropane [**3**] at low energies but, at higher energies, dissociation to cyclobutane ion [**5**] is also possible. Therefore, as discussed in length in the previous section, the source of the m/z = 41 ion [**11**] is most likely 1-butene ion [**4**] formed through the β-carbon H-shift. The structure of the $C_3H_5^+$ ion is $CH_2CHCH_2^+$ formed by a methyl loss without a saddle point from 1-butene ion at 11.63 eV.

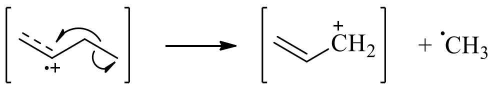

[**4**] [**11**]

Scheme 6. Formation of allylium ion (*m/z* = 41) from 1-butene ion (*m/z* = 56) *via* a methyl radical loss.

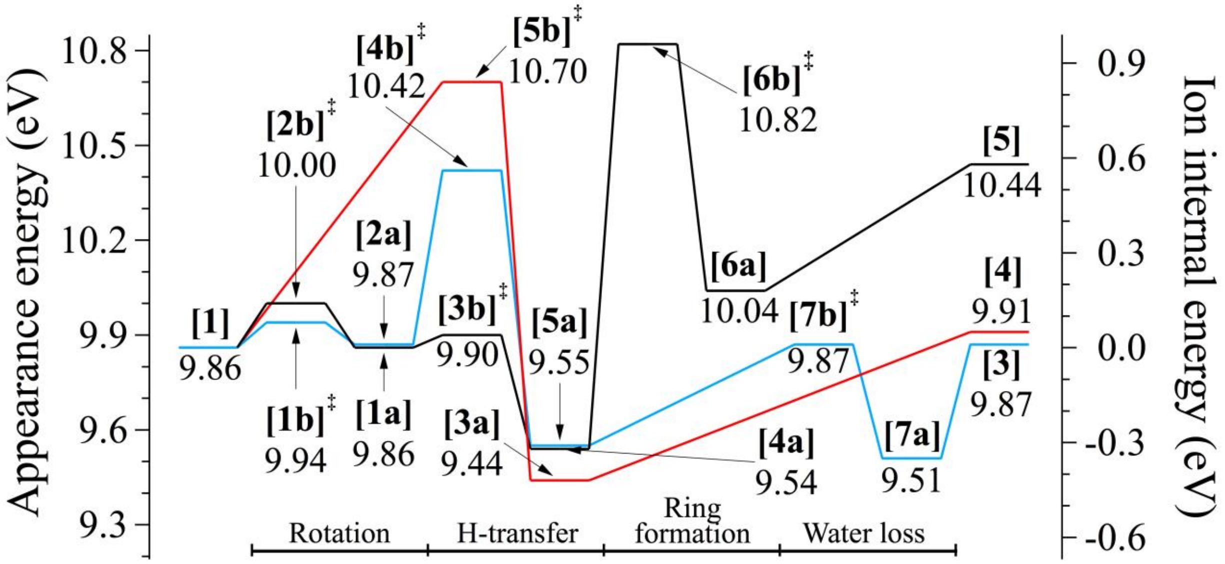

Figure 22. Potential energy surface of the beta, gamma, and delta-carbon hydrogen transfers, shown with red, blue, and black colors, respectively. All energies are at 0 K at the G4 level of theory. Energies on the left axis are relative to the neutral precursor while energies on the right axis are relative to the molecular ion. For structures, see Figure 23 and the schemes in the text.

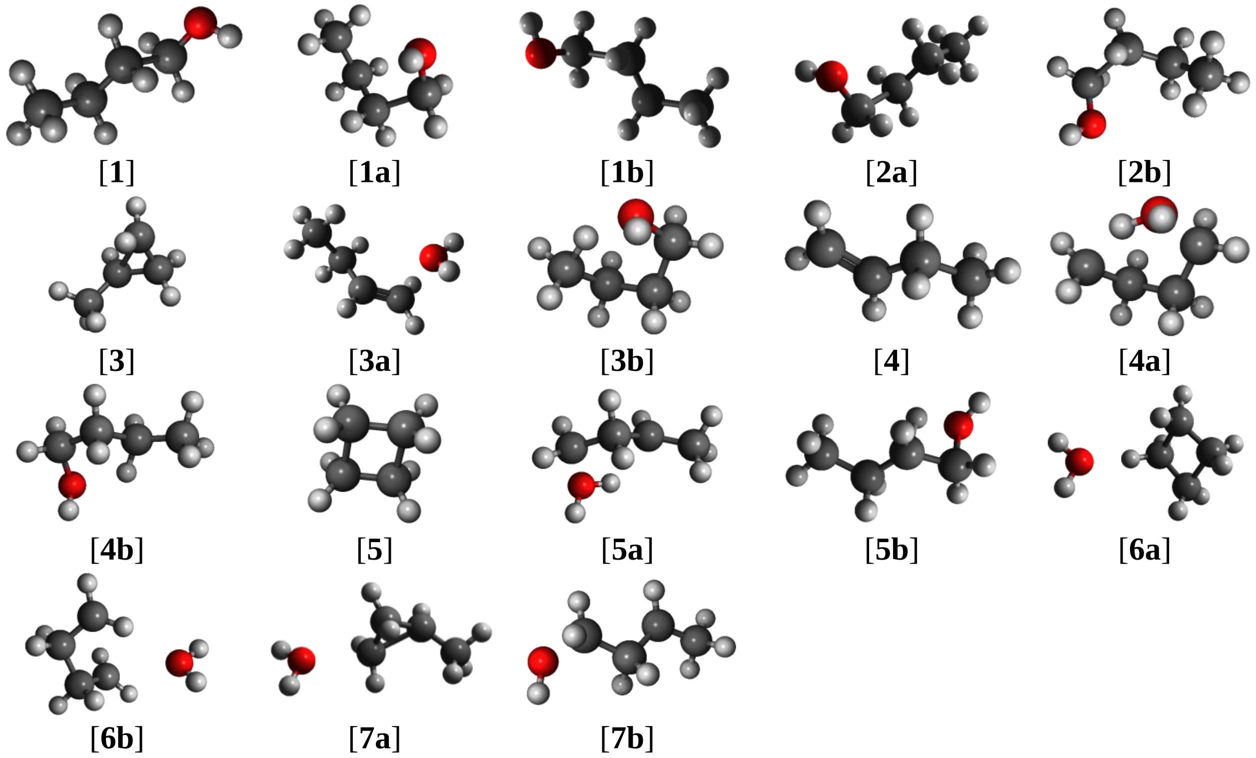

Figure 23. Structures of minima and saddle points as indicated in Figure 22.

The next ion in the breakdown diagram, $C_3H_6^{+\bullet}$ [**7**], is the product of a methanol loss. The lowest energy pathway is the γ-carbon hydrogen transfer to the α-carbon followed by the barrierless loss of the CH_3OH fragment. Hydrogen migration proceeds through a reverse barrier of 10.87 eV and falls into a minimum structure, where the α- and β-carbon atoms are separated by a bridging hydrogen atom. At this point, methanol is in a loose ion-neutral complex with the $CH_3CHCH_2^{+\bullet}$ molecular ion. The α-carbon–hydrogen and β-carbon–hydrogen distances are 1.283 Å and 1.445 Å, respectively, and a C_α–H–C_β angle of 169°.

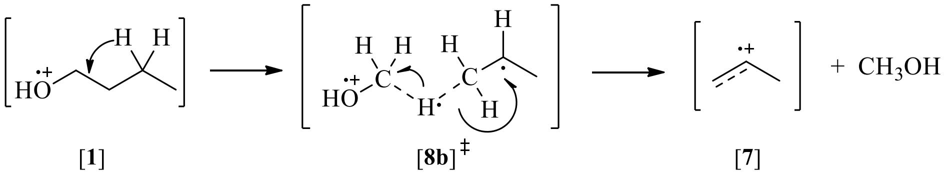

Scheme 7. Formation of propene ion (*m/z* = 42) *via* a methanol loss.

It is evident that the *m/z* = 33 ion, $CH_3OH_2^+$ [**8**], cannot be formed without substantial rearrangement of the molecular ion. The first step is the β-carbon hydrogen transfer to the OH group at 10.70 eV, which is the same initial step that we saw in the higher-energy water-loss channel. Then, the methyl group and water molecule form protonated methanol through a reverse barrier and the CH_2CHCH_2 fragment is lost. Optimizations of this TS structure have not converged.

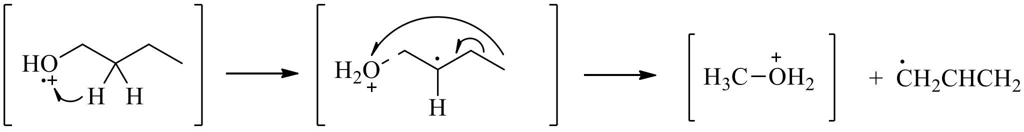

[**1**] [**5b**]‡ [**8**]

Scheme 8. Formation of methyloxonium ion (*m/z* = 33) *via* an allyl radical loss.

The last two ions observed in our experiments, CH_2OH^+ [**10**] and $C_3H_7^+$ [**9**], could theoretically be formed by a simple bond rupture of 1-butanol. To confirm or reject this, constrained potential energy scans along the C_α–C_β bond length were performed on the molecular ion and no saddle point was located at the B3LYP level of theory. This means that $CH_2OH^+ + CH_3CH_2CH_2^•$ and $CH_3CH_2CH_2^+ + CH_2OH^•$ could formed at 11.17 eV and 11.34 eV, respectively. However, both of these values are higher than the experimental appearance energies of 11.104 ± 0.030 eV. Further quantum-chemical investigation revealed that one of the γ-hydrogen atoms can be transferred over to the β-carbon, forming the energetically more stable CH_3CHCH_3 structure. At the G4 level, the saddle point corresponding to hydrogen transfer is at 11.00 eV; slightly higher than the thermochemical threshold for $CH_3CHCH_3^+$ (10.99 eV) and slightly lower than the calculated threshold for CH_2OH^+ (11.05 eV).

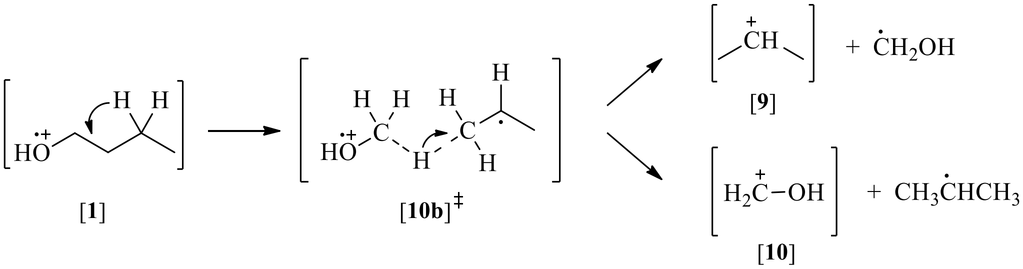

Scheme 9. Formation of isopropylium (m/z = 43) and hydroxymethylium (m/z = 31) ions.

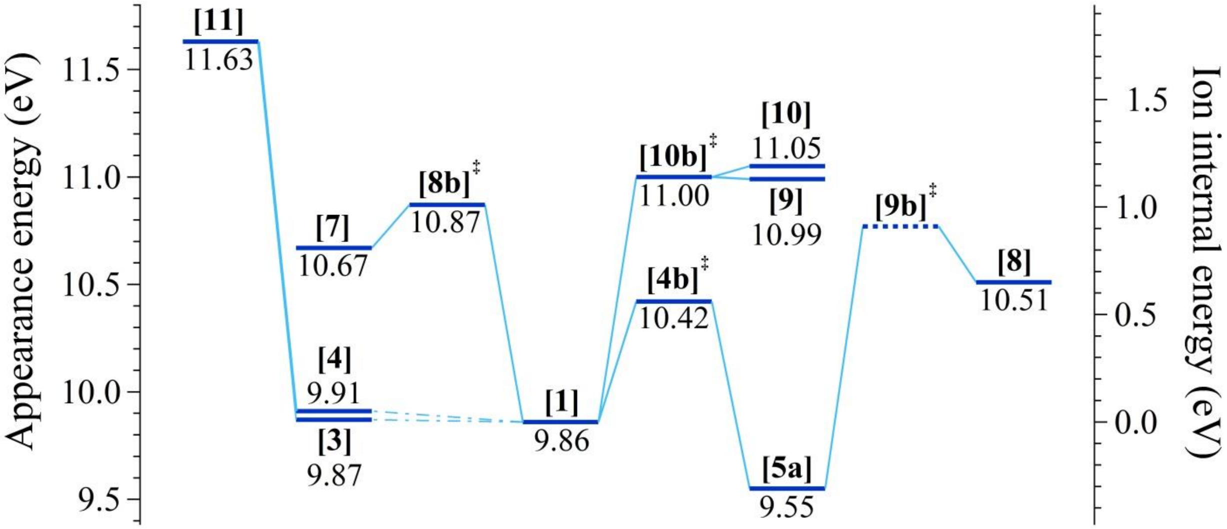

Figure 24. G4-calculated potential energy surface for the remaining dissociation pathways of energy-selected 1-butanol ions. Energies on the left axis are relative to the neutral precursor while energies on the right axis are relative to the molecular ion. For structures, see Figures 23, 25 and the schemes in the text.

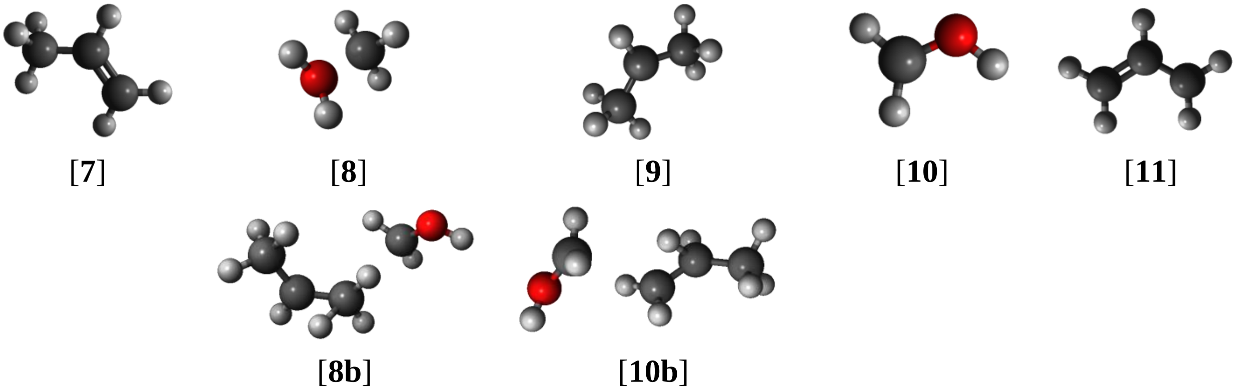

Figure 25. Structures of minima and saddle points as indicated in Figure 24.

3.2.6.2. Isobutanol. The first dissociation channel is the formation of $C_4H_8^{+\bullet}$ by a water loss that also requires the rearrangement of the molecular ion. We explored hydrogen atom transfers to the OH group both from the CH and CH_3 groups. The methine hydrogen is transferred in a single step through a barrier at 10.50 eV, forming isobutene, $CH_2{=}C(CH_3)CH_3^{+\bullet}$ molecular ion after the successive, barrierless water loss.

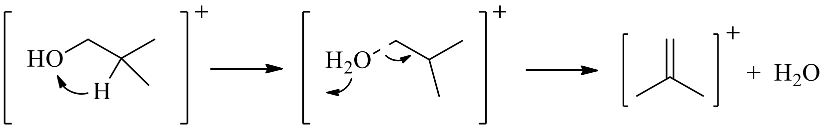

[**2**] [**8a**] [**6**]

Scheme 10. Formation of isobutene (*m/z* = 56) *via* a water loss.

In the case of the methyl hydrogen shift, the transfer happens through a saddle point at 10.58 eV. This ion-molecule complex has a 4-membered ring, which is significantly more strained, compared to ones formed in the case of 1-butanol, with a O···C bond distance of only 1.547 Å. At this point there are two possibilities: (1) losing the water or (2) forming a three-membered ring. In the first case, water is lost through a barrier at 10.34 eV, while the molecular ion undergoes a rearrangement *via* a methyl migration, forming 1-butene molecular ion.

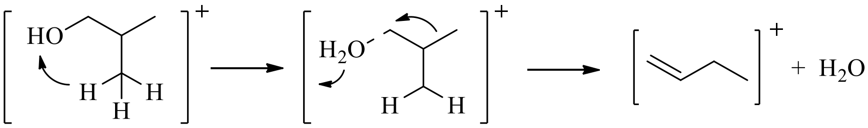

[**2**] [**9a**] [**4**]

Scheme 11. Formation of 1-butene (*m/z* = 56) after an internal rearrangement.

In the other pathway, the α and γ carbon atoms move closer to each other, forming a cyclopropane ring through a barrier of 10.64 eV. Then, water is lost without a saddle point, forming methylcyclopropane molecular ion with a similar thermochemical limit as in the case of [**4**].

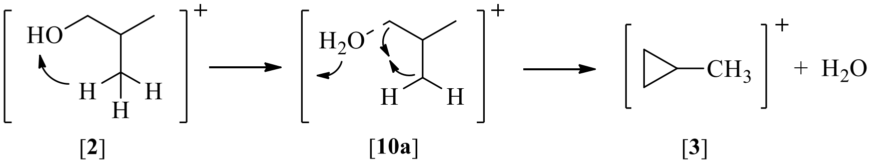

Scheme 12. Formation of methylcyclopropane (*m/z* = 56) *via* ring closure.

Since the ring closure step proceeds through a higher-lying transition state than for 1-butene (see Scheme 10), the most likely second contributor to the *m/z* = 56 signal is 1-butene ion but this latter channel leading to methylcyclopropane ion cannot be ruled out, either.

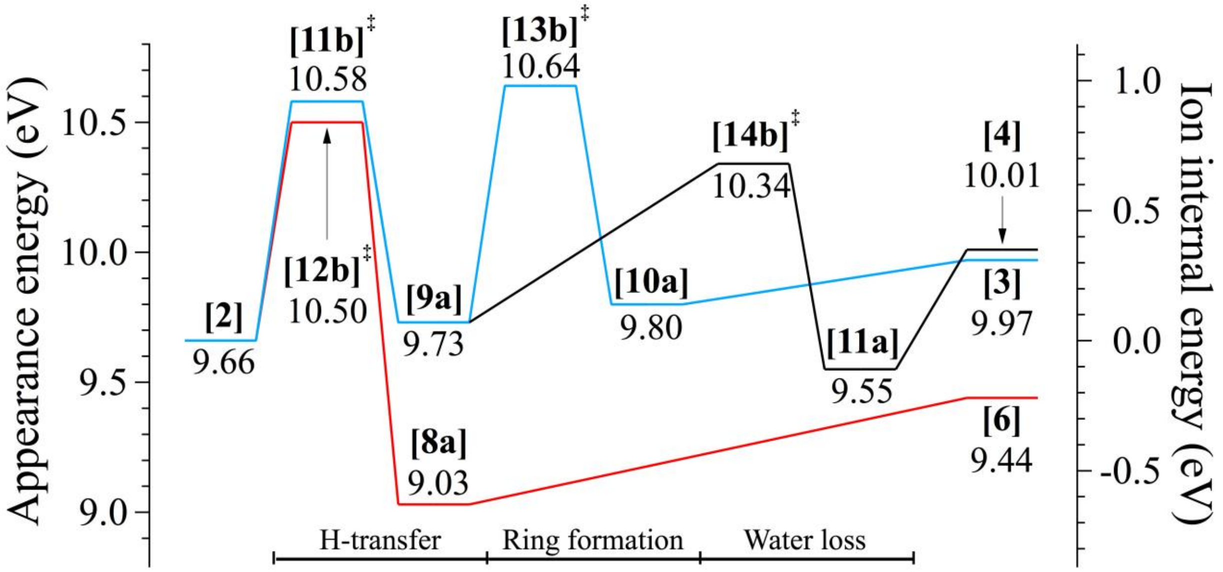

Figure 26. Potential energy surface for the internal hydrogen rearrangement and subsequent water loss from energy-selected isobutanol ions. Beta and gamma hydrogen transfers are shown with red and blue ink, respectively, and black lines show the methylcyclopropane formation through the ring closure. Energies on the left axis are relative to the neutral precursor while energies on the right axis are relative to the molecular ion. For structures, see Figures 23, 27 and the schemes in the text.

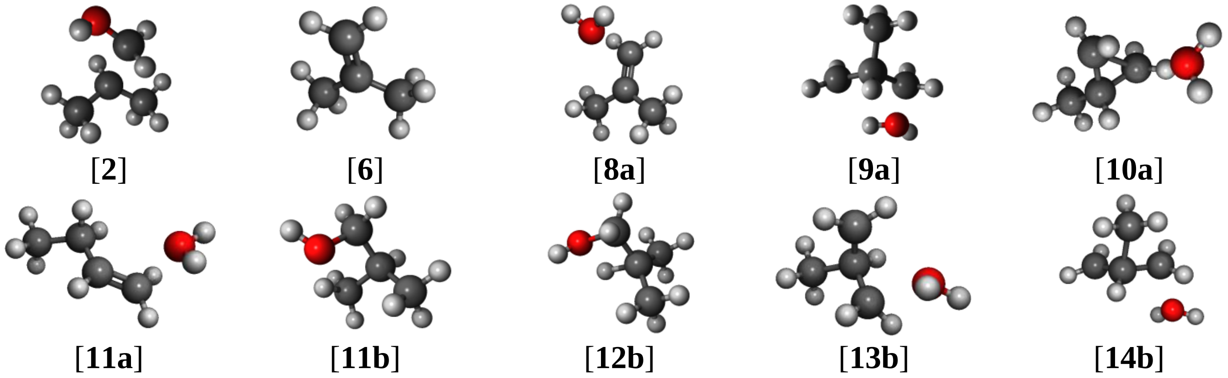

Figure 27. Structures of minima and saddle points as indicated in Figure 26.

The next fragment ion, namely $CH_3OH_2^+$ is formed by a C_3H_5 loss. Its formation requires substantial rearrangement within the molecular ion. First, a hydrogen atom is transferred from one of the methyl groups to the hydroxyl group at 10.58 eV, similarly to the water loss channel. Then, the other methyl group and the water moiety forms the protonated methanol ion. The remaining neutral, which has a CH_2CHCH_2 structure leaves without a reverse barrier.

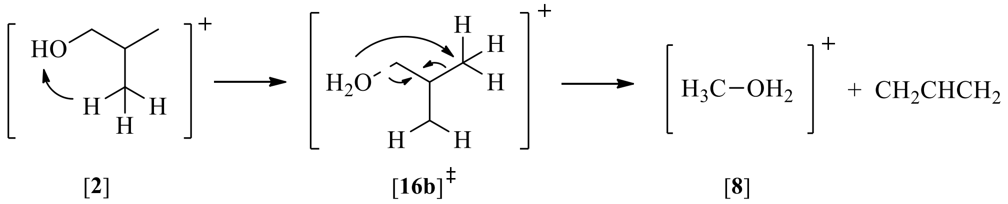

Scheme 13. Formation of methyloxonium ion (*m/z* = 33) *via* two internal rearrangement steps.

The next ion in the breakdown diagram, $C_3H_6^{+\bullet}$, is formed *via* a methanol loss and the dissociation mechanism is similar to the $CH_3OH_2^+$ channel. In this case, one of the methyl groups moves closer to the hydroxyl group, forming a CH_3OH group, which leaves without a reverse barrier, forming the $CH_3CHCH_2^{+\bullet}$ fragment ion at a thermochemical threshold of 10.77 eV. An other possibility involving the transfer of a methyl hydrogen to the α-carbon was ruled out as it only resulted in an internal rearrangement of the molecular ion. The hydroxyl group moves to the place of the transferred hydrogen atom, essentially reforming isobutanol.

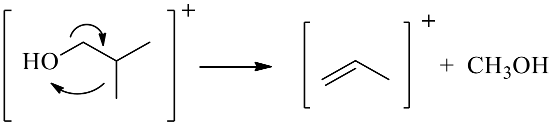

[**2**] [**7**]

Scheme 14. Formation of propene ion (*m/z* = 42) *via* a methanol loss.

$C_3H_7^+$ is the dominant channel in the breakdown diagram above 12.0 eV. Contrary to 1-butanol there is no need for rearrangement to form the energetically favorable CH_3CHCH_3 structure. Constrained potential energy scans along the C_α–C_β bond length in the isobutanol molecular ion showed no saddle point, forming the energetically favored $C_3H_7^+$ ion at 11.09 eV, or forming CH_2OH^+ at 11.15 eV, which latter is only a minor product, contrary to the analogous dissociation from the 1-butanol ion.

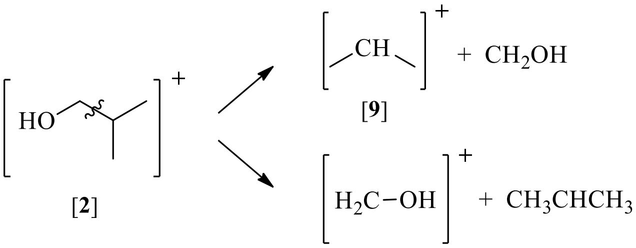

[**2**] [**9**] [**10**]

Scheme 15. Formation of isopropylium ion (*m/z* = 43) and hydroxymethylium ion (*m/z* = 31) *via* a bond rupture.

Finally, $C_3H_5^+$ is formed by a sequential $CH_3^\bullet$ loss from 1-butene molecular ion without a saddle point at 11.73 eV.

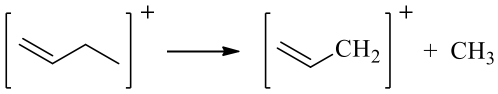

[**4**] [**11**]

Scheme 16. Formation of allylium ion (*m/z* = 41) from 1-butene ion (*m/z* = 56) *via* a methyl radical loss.

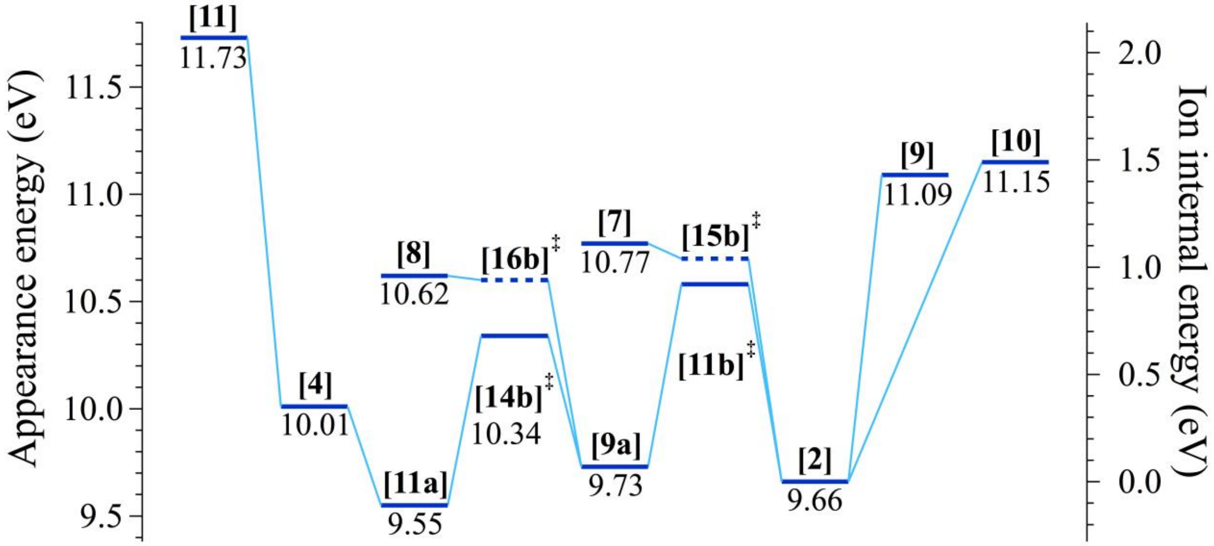

Figure 28. G4-calculated potential energy surface for the remaining dissociation pathways of energy-selected isobutanol ions. Energies on the left axis are relative to the neutral precursor while energies on the right axis are relative to the molecular ion. For structures, see Figures 23, 25, 27, and the schemes in the text.

Calculated and experimental appearance energies are summarized in Table 3.

Table 3

Comparison of the appearance energies for the various dissociation channels of 1-butanol and isobutanol cations.

Fragment ion	Experimental E_0 (eV)		G4-calculated E_0 (eV)	
	from 1-butanol	from isobutanol	from 1-butanol	from isobutanol
$C_4H_8^{+\bullet}$	10.347 ± 0.015	10.566 ± 0.050	10.42	10.58
$C_3H_7^{+}$	11.104 ± 0.030	10.970 ± 0.050	11.00	11.09
$C_3H_6^{+\bullet}$	10.942 ± 0.040	10.723 ± 0.020	10.87	TS (10.77)
$C_3H_5^{+}$	11.6 – 11.7	11.6 – 11.9	11.63	11.73
$CH_3OH_2^{+}$	10.738 ± 0.090	10.612 ± 0.020	TS (10.51)	TS (10.62)
CH_2OH^{+}	11.104 ± 0.030	11.11 ± 0.20	11.05	11.15

3.2.7. Thermochemistry

In the absence of a reverse barrier (that is, through a loose transition state), appearance energies represent the thermochemical limits leading to the ionic and neutral products. Therefore, the 0 K heat of formation of the 1-butanol and isobutanol can be calculated by using well-known literature thermochemical data on the fragment ions and neutrals and the appearance energies extracted from the modeled breakdown diagrams. Ancillary thermochemical data and the results of this work are summarized in Table 4.

Table 4

Auxiliary and derived thermochemical data.

Chemical formula	**Species**	$\Delta_f H^{\circ}_{0\,K}$	$\Delta_f H^{\circ}_{298\,K}$	
		kJ mol^{-1}		
$C_4H_{10}O$	1-butanol	–245.81[c]		
			–274.4[d]	
			–274.9[e]	± 0.4
	isobutanol	–249.4[a]	–279.1[a]	± 1.6
			–283.8[d,f]	± 0.8
			–284.1[e]	± 0.9
$C_3H_7^+$	$CH_3CH^+CH_3$	822.91[b]		± 0.25
	$CH_3CH_2CH_2^+$	856.96[b]		± 0.86
C_3H_7	CH_3CHCH_3	105.32[b]		± 0.53
	$CH_3CH_2CH_2$	118.34[b]		± 0.55
CH_3O^+	CH_2OH^+	717.9[b]		± 0.7
		717.70[b]		± 0.18
CH_3O	CH_2OH	–11.1[b]		± 0.9
		–10.46[b]		± 0.28

[a]This work; [b]ATcT[195]; [c]Yaws[174]; [d]Rosenstock *et al.*[173]; [e]Pedley *et al.*[172]; [f]Connett.[175]

In the studied energy ranges, every dissociation pathway of 1-butanol ions and most isomerization pathways of isobutanol ions proceed through various higher-lying transition states, which means that the appearance energies do not correspond to the thermochemical limits corresponding to the products. This prevents using these experimental appearance energies to extract reliable and accurate thermochemical information. However, there is one, rather prominent channel in isobutanol dissociative photoionization where the rearrangement transition state is submerged and the appearance energy does correspond to the thermochemical limit, and this is the $CH_3CHCH_2^{+\bullet}$ + CH_3OH channel. Combining this with the E_0s of $C_3H_7^+$ and CH_2OH^+ channels, we can calculate the isobutanol 0 K heat of formation reliably from three different channels. The extracted appearance energy for $CH_3CHCH_2^{+\bullet}$ + CH_3OH dissociation is 10.723 ± 0.020 eV. The ATcT[195] reports $\Delta_f H^{\circ}_{0\,K}$ of 975.22 ± 0.21 kJ mol^{-1} for the propylene ion and –190.01 ± 0.15 kJ mol^{-1} for methanol, which gives –249.40 ± 1.76 kJ mol^{-1} for the 0 K heat of formation of isobutanol. The second channel is for $CH_3CHCH_3^+$ + $CH_2OH^\bullet$ dissociation with a E_0 of 10.970 ± 0.050 eV. Using the heats of formations found in ATcT[195] as 822.91 ± 0.25 kJ mol^{-1} for the ion and –10.46 ± 0.28 kJ mol^{-1} for the radical, we obtain a 0 K heat of formation of isobutanol as –245.99 ± 4.84 kJ mol^{-1}. Finally, the complimentary pair of the former dissociation, CH_2OH^+ + $CH_3CHCH_3^\bullet$, is used in a similar fashion with ATcT heats of formations of 717.70 ± 0.18 kJ mol^{-1} for the ion and 105.32 ± 0.53 kJ mol^{-1} for the radical. The isobutanol heat of formation is calculated to be –248.0 ± 19.3 kJ mol^{-1}. The weighted average of all three values is calculated to be –249.00 ± 1.64 kJ mol^{-1} as described by Shuman *et al.*[196] To compare the evaluated heat of formation of isobutanol with literature values we converted our 0 K value to 298 K. The conversion factor ($H_{298\ \mathrm{K}} - H_{0\ \mathrm{K}}$) was carefully calculated to be 20.7 kJ mol^{-1} by Bodi *et al.*,[197] who took every internal rotation of isobutanol into account. Therefore, we obtain –279.10 ± 1.64 kJ mol^{-1} as the 298 K heat of formation of isobutanol. Connett[175] and Rosenstock[173] reported –283.8 kJ mol^{-1} and –283.8 ± 0.9 kJ mol^{-1}, respectively as the gas phase heat of formation of isobutanol at 298 K, while Pedley *et al.*[172] gave –284.1 ± 0.9 kJ mol^{-1} at the same temperature. Our calculated 298 K heat of formation value does not match with literature findings.

3.2.8. Conclusions

The unimolecular dissociation mechanism of internal energy selected 1-butanol and isobutanol cations was investigated by imaging photoelectron photoion coincidence spectroscopy using VUV synchrotron radiation. Both butanol isomer cations dissociate by numerous parallel and consecutive dissociation channels producing fragment ions with the same mass-to-charge ratios: *m/z* = 31, 33, 41, 42, 43, and 56. The fractional ion abundances were plotted in breakdown diagrams, which showed markedly different behaviors between the two butanol isomers, despite the similarity expressed in fragment masses. To understand the reaction mechanisms and to obtain reliable 0-K appearance energies, the breakdown diagrams were modeled using statistical energy distributions and rate theory and the interpretation and analysis was aided by high-level quantum chemical calculations.

In both systems, the first dissociation channel is a water-loss at the 0 K appearance energy of 10.347 ± 0.015 eV and 10.566 ± 0.050 eV for 1-butanol and isobutanol, respectively. Both channels are slow at the dissociation limit on the timescale of the experiment and involve an initial isomerization step forming loose $C_4H_8^{+\bullet}\cdots H_2O$ ion-neutral complexes. It should be noted, however, that the two isomers do not proceed through the same ion-neutral complex. In the case of 1-butanol, the ion-neutral complex is formed by a γ-carbon H-atom shift through a transition state at 10.42 eV and followed by a subsequent loss of water producing the methylcyclopropane fragment ion (*m/z* = 56, [**3**]). In contrast, in isobutanol the ion-neutral complex is formed by a H-atom shift from the methine group through a reverse barrier at 10.50 eV and the resulting water is lost to form the isobutene fragment ion (*m/z* = 56, [**6**]). On one hand, this H_2O-loss channel dominates the 1-butanol breakdown diagram in the 10.0–11.5 eV photon energy range while, on the other hand, it only appears as a minor pathway for isobutanol. The noticeable difference in behavior observed between the two isomers can be explained by examining the tightness of the H-shift transition state involved in the formation of the ion-neutral complex. This rearrangement involves a favored 5-membered ring structure in 1-butanol, but requires a less favorable 4-membered ring structure in isobutanol, resulting in a more strained TS in isobutanol. Therefore, this channel is quickly overtaken by the kinetically more favorable $CH_3OH_2^+$ channel.

For 1-butanol, the $CH_3OH_2^+$ (m/z = 33, [**8**]) channel only reaches ~10% maximum abundance. The formation of this cation proceeds through a higher lying transition state, rendering it unavailable at its thermochemical threshold. The 0 K appearance energy was found to be 10.738 ± 0.090 eV. The experimentally derived activation entropies at 600 K are 18.2 $J\ K^{-1}\ mol^{-1}$ and 2.0 $J\ K^{-1}\ mol^{-1}$ for m/z = 56 and 33 channels in 1-butanol, respectively. In contrast, for isobutanol, the breakdown diagram is dominated by this cation in the 10.4–11.3 eV photon energy range. Its formation is slow at the dissociation limit and involves the formation of another ion-neutral complex by first a H-atom shift from one of the methyl to the hydroxyl group at 10.58 eV, and a subsequent $CH_3OH_2^+$-loss through a submerged reverse barrier. The 0 K appearance energy of $CH_3OH_2^+$ was determined to be 10.612 ± 0.020 eV, in excellent agreement with the G4 calculated thermochemical limit of 10.62 eV. The experimental activation entropies at 600 K are –43.1 $J\ K^{-1}\ mol^{-1}$ and 17.1 $J\ K^{-1}\ mol^{-1}$ for m/z = 56 and 33 channels, respectively. This provides further evidence that the m/z = 56 transition state is significantly tighter than that of m/z = 33.

The next channel in the 1-butanol breakdown diagram is the formation of $C_3H_6^{+\bullet}$ (m/z = 42, [**7**]) by a CH_3OH-loss. The lowest energy structure is the $CH_3CH{=}CH_2$ ion, which is formed by an internal H-shift from the γ-carbon to the β-carbon through a reverse barrier of 10.87 eV prior to a barrierless loss of CH_3OH. The 0 K appearance energy is 10.942 ± 0.040 eV. In the breakdown diagram of the isobutanol cation, the formation of $C_3H_6^{+\bullet}$ rapidly takes over, with an appearance energy of 10.723 ± 0.020 eV, and accounts for the highest ion abundance up to about 11.9 eV. This ion is easily accessible by a methyl group "grabbing on" the hydroxyl group, forming the $CH_3CH{=}CH_2$ ion. Note, that this mechanism in 1-butanol would result in the formation of a higher-energy *c*-$CH_2CH_2CH_2$ ion, which is not energetically consistent with the observed experimental results.

In both butanol isomers, the fragmentation pathways of the $C_3H_7^+$ (*m/z* = 43, [**9**]) and the CH_2OH^+ (*m/z* = 31, [**10**]) cations correspond to a complementary pair. Based on the experimentally indistinguishable appearance energies of these two fragments in 1-butanol, we concluded that the dissociation proceeds through a common transition state, slightly above the thermochemical limits at 11.104 ± 0.030 eV. However, in the case of isobutanol, the $C_3H_7^+$ (*m/z* = 43) and CH_2OH^+ (*m/z* = 31) fragment ions are formed by direct C–C bond cleavage at the appearance energy of 10.970 ± 0.050 and 11.11 ± 0.20 eV, respectively. The difference between the E_0 for these two fragment ions can be accounted for by looking at the difference in the ionization energy of CH_2OH^+ and $C_3H_7^+$, calculated to be 0.110 eV, in good agreement with our experimental appearance energies. These conclusions are further supported by observed discrepancies in the branching ratios between the two complementary channels in the two butanol isomers. In the case of 1-butanol, the abundances of these channels are comparable with a maximum of 40% for $C_3H_7^+$ [**9**] and 30% for CH_2OH^+ [**10**], supporting the conclusion of a common transition state at play. However, for isobutanol cations, $C_3H_7^+$ [**9**] dominates the breakdown diagram above 11.9 eV with a maximum abundance of ~70%, whereas CH_2OH^+ [**10**] is only a minor channel with 15%. This significant difference is explained by $C_3H_7^+$ [**9**] being the thermodynamically favored product.

Finally, in the case of both butanol isomers, a consecutive dissociation channel opens up around 11.7–11.9 eV, consistent with the formation of $C_3H_5^+$ (*m/z* = 41, [**11**]) by a consecutive loss of a methyl group from the H_2O-loss fragment ion. This consecutive channel amounts to about 15% in 1-butanol and only a few percent in isobutanol. Since water loss is possible through more than one mechanism and, in fact, the *m/z* = 41 channel could only be fit assuming at least two parallel pathways, an accurate statistical modeling of the consecutive dissociation was not possible with any practical fidelity.

In conclusion, PEPICO is successfully implemented to investigate complex dissociation mechanisms of 1-butanol and isobutanol involving isomerization of molecular ions. These findings were used to explain the differences in the relative abundances of dissociation channels. Furthermore, fragment ions *m/z* = 33 and 43 in 1-butanol, and *m/z* = 31 and 41 in isobutanol, were not reported in earlier studies.

REFERENCES

1. Meyerson, S., Organic Ions in the Gas Phase. XIII. Cycloheptatriene-7-*d*; Decomposition of $C_7H_8^+$ and $C_7H_8^{++}$ from Cycloheptatriene and Toluene. *J. Am. Chem. Soc.* **1963**, *85*, 3340–3344.

2. Hoffman, M. K.; Bursey, M. M., The Structure of the Molecular Ion of C_7H_8 Isomers: an ICR Study. *Tetrahedron Lett.* **1971**, *12*, 2539–2542.

3. Traeger, J. C.; McLoughlin, R. G., A Photoionization Study of the Energetics of the $C_7H_7^+$ Ion Formed from C_7H_8 Precursors. *Int. J. Mass Spectrom. Ion Phys.* **1978**, *27*, 319–333.

4. Schwell, M.; Dulieu, F.; Gée, C.; Jochims, H.-W.; Chotin, J.-L.; Baumgärtel, H.; Leach, S., Photoionization Mass Spectrometry of Six Isomers of C_7H_8 in the 7-22 eV Photon Energy Range. *Chem. Phys.* **2000**, *260*, 261–279.

5. McAdoo, D. J.; Hudson, C. E., Ion-Neutral Complex-Mediated Hydrogen Exchange in Ionized *n*-Butanol: a Mechanism for 'Non-specific' Hydrogen Migrations. *Org. Mass Spectrom.* **1987**, *22*, 615–621.

6. Ahmed, M. S.; Hudson, C. E.; Giam, C. S.; McAdoo, D. J., Methylcyclopropane Ion Formation by Elimination of Water from *n*-Butanol and 2-Methylpropanol Ions. *Org. Mass Spectrom.* **1991**, *26*, 1089–1091.

7. Skinner, H. A.; Snelson, A., The Heats of Combustion of the Four Isomeric Butyl Alcohols. *Trans. Faraday Soc.* **1960**, *56*, 1776–1783.

8. Shao, J. D.; Baer, T.; Lewis, D. K., Dissociation Dynamics of Energy-Selected Ion-Dipole Complexes. 2. Butyl Alcohol Ions. *J. Phys. Chem* **1988**, *92*, 5123–5128.

9. McLafferty, F. W.; Bockhoff, F. M., Formation of Benzyl and Tropylium Ions from Gaseous Toluene and Cycloheptatriene Cations. *J. Am. Chem. Soc.* **1979**, *101*, 1783–1786.

10. Bombach, R.; Dannacher, J.; Stadelmann, J.-P., The Rate-Energy Functions for the Formation of Tropylium and Benzylium Ions from Toluene Molecular Cations. *Chem. Phys. Lett.* **1983**, *95*, 259–261.

11. Traeger, J. C.; Kompe, B. M., Threshold $C_7H_7^+$ Formation from the Benzyl Halides by Photoionization Mass Spectrometry. *Int. J. Mass Spectrom. Ion Proc.* **1990**, *101*, 111–120.

12. Lifshitz, C.; Gotkis, Y.; Laskin, J.; Ioffe, A.; Shaik, S., Threshold Formation of Benzylium (Bz^+) and Tropylium (Tr^+) from Toluene. Nonstatistical Behavior in Franck-Condon Gaps. *J. Phys. Chem.* **1993**, *97*, 12291–12295.

13. Fati, D.; Lorquet, A. J.; Locht, R.; Lorquet, J. C.; Leyh, B., Kinetic Energy Release Distributions for Tropylium and Benzylium Ion Formation from the Toluene Cation. *J. Phys. Chem. A* **2004**, *108*, 9777–9786.

14. Nagy, A.; Fulara, J.; Garkusha, I.; Maier, J. P., On the Benzylium/Tropylium Ion Dichotomy: Electronic Absorption Spectra in Neon Matrices. *Angew. Chem. Int. Ed.* **2011**, *50*, 3022–3025.

15. Chiavarino, B.; Crestoni, M. E.; Dopfer, O.; Maitre, P.; Fornarini, S., Benzylium versus Tropylium Ion Dichotomy: Vibrational Spectroscopy of Gaseous $C_8H_9^+$ Ions. *Angew. Chem. Int. Ed.* **2012**, *51*, 4947–4949.

16. Jusko, P.; Simon, A.; Banhatti, S.; Brünken, S.; Joblin, C., Direct Evidence of the Benzylium and Tropylium Cations as the Two Long-Lived Isomers of $C_7H_7^+$. *ChemPhysChem* **2018**, *19*, 3182–3185.

17. Baer, T.; Booze, J. A.; Weitzel, K. M. In *Vacuum Ultraviolet Photoionization and Photodissociation of Molecules and Clusters*, Wiley Series in Ion Chemistry and Physics, Singapore, Ng, C.-Y., Ed. World Scientific: Singapore, 1991; pp 259–298.
18. Borkar, S.; Sztáray, B., Self-Consistent Heats of Formation for the Ethyl Cation, Ethyl Bromide, and Ethyl Iodide from Threshold Photoelectron Photoion Coincidence Spectroscopy. *J. Phys. Chem. A* **2010**, *114*, 6117–6123.
19. Borkar, S.; Sztáray, B.; Bodi, A., Dissociating $C_3H_5Br^+$ Ions: Almost All Roads Lead to the Allyl Cation. *Int. J. Mass Spectrom.* **2012**, *330–332*, 100–108.
20. Muller, G.; Voronova, K.; Sztáray, B.; Meloni, G., Rotamers and Migration: Investigating the Dissociative Photoionization of Ethylenediamine. *The Journal of Physical Chemistry A* **2016**, *120*, 3906-3916.
21. Stockbauer, R., Threshold Electron-Photoion Coincidence Mass Spectrometric Study of CH_4, CD_4, C_2H_6, and C_2D_6. *J. Chem. Phys.* **1973**, *58*, 3800–3815.
22. Rosenstock, H. M.; Stockbauer, R.; Parr, A. C. P., Photoelectron–Photoion Coincidence Study of the Bromobenzene Ion. *J. Chem. Phys.* **1980**, *73*, 773–777.
23. Werner, A. S.; Baer, T., Absolute Unimolecular Decay Rates of Energy Selected $C_4H_6^+$ Metastable Ions. *J. Chem. Phys.* **1975**, *62*, 2900–2910.
24. Das, P. R.; Nishimura, T.; Meisels, G. G., Fragmentation of Energy-Selected Hexacarbonylchromium Ion. *J. Phys. Chem.* **1985**, *89*, 2808–2812.
25. Norwood, K.; Guo, J. H.; Ng, C. Y., A Photoion–Photoelectron Coincidence Study of Ar_n (n=2–4). *J. Chem. Phys.* **1989**, *90*, 2995–3003.
26. Dutuit, O.; Baer, T.; Metayer, C.; Lemaire, J., Isotope Effects in the Dissociation of Partially Deuterated Dimethyl Ether, CH_3OCD^{+3} Ions. *Int. J. Mass Spectrom. Ion Proc.* **1991**, *110*, 67–82.
27. Weitzel, K.-M.; Mähnert, J.; Baumgärtel, H., The Determination of the Transition State Structure from the J Dependence of the Dissociation Energy E_0 (J): The Methane and Ethane Ion Dissociation. *Ber. Bunsenges. Phys. Chem.* **1993**, *97*, 134–139.
28. Thissen, R.; Alcaraz, C.; Hepburn, J.; Vervloet, M.; Dutuit, O., Dissociative Photoionisation of Acetylene-Ethane van der Waals Clusters. *Int. J. Mass Spectrom.* **2000**, *199*, 201–209.
29. Baer, T.; Sztáray, B.; Kercher, J. P.; Lago, A. F.; Bodi, A.; Skull, C.; Palathinkal, D., Threshold Photoelectron Photoion Coincidence Studies of Parallel and Sequential Dissociation Reactions. *Phys. Chem. Chem. Phys.* **2005**, *7*, 1507–1513.
30. Winick, H.; Brown, G.; Halbach, K.; Harris, J., Wiggler and Undulator Magnets. *Phys. Today* **1981**, *34*, 50–63.
31. Bodi, A.; Sztáray, B.; Baer, T., Dissociative Photoionization of Mono-, Di- and Trimethylamine Studied by a Combined Threshold Photoelectron Photoion Coincidence Spectroscopy and Computational Approach. *Phys. Chem. Chem. Phys.* **2006**, *8*, 613–623.
32. Bodi, A.; Sztáray, B.; Baer, T.; Johnson, M.; Gerber, T., Data Acquisition Schemes for Continuous Two-Particle Time-of-Flight Coincidence Experiments. *Rev. Sci. Instrum.* **2007**, *78*, 084102.
33. Kramida, A.; Ralchenko, Y.; Reader, J.; Team, N. A., NIST Atomic Spectra Database (version 5.7.1). National Institute of Standards and Technology: Gaithersburg, MD, 2019.
34. Eppink, A. T. J. B.; Parker, D. H., Velocity Map Imaging of Ions and Electrons Using Electrostatic Lenses: Application in Photoelectron and Photofragment Ion Imaging of Molecular Oxygen. *Rev. Sci. Instrum.* **1997**, *68*, 3477–3484.

35. Chandler, D. W.; Parker, D. H., Velocity Mapping of Multiphoton Excited Molecules. In *Advances in Photochemistry,* Neckers, D. C.; Volman, D. H.; von Bünau, G., Eds. John Wiley & Sons, Inc.: New York, NY, 1999; pp 59–106.
36. Davies, J. A.; LeClaire, J. E.; Continetti, R. E.; Hayden, C. C., Femtosecond Time-Resolved Photoelectron–Photoion Coincidence Imaging Studies of Dissociation Dynamics. *J. Chem. Phys.* **1999**, *111*, 1–4.
37. Tsai, B.; Baer, T.; Horovitz, M. L., A Time-of-Flight Detection System for Near Threshold Photoelectron Spectroscopy. *Rev. Sci. Instrum.* **1974**, *45*, 494–498.
38. King, G. C.; Zubek, M.; Rutter, P. M.; Read, F. H., A High Resolution Threshold Electron Spectrometer for Use in Photoionisation Studies. *J. Phys. E: Sci. Instrum.* **1987**, *20*, 440–443.
39. Chandler, D. W.; Houston, P. L., Two-Dimensional Imaging of State-Selected Photodissociation Products Detected by Multiphoton Ionization. *J. Chem. Phys.* **1987**, *87*, 1445–1447.
40. Baer, T.; Li, Y., Threshold Photoelectron Spectroscopy with Velocity Focusing: an Ideal Match for Coincidence Studies. *Int. J. Mass Spectrom.* **2002**, *219*, 381–389.
41. Sztáray, B.; Baer, T., Suppression of Hot Electrons in Threshold Photoelectron Photoion Coincidence Spectroscopy Using Velocity Focusing Optics. *Rev. Sci. Instrum.* **2003**, *74*, 3763–3768.
42. Baer, T.; Bodi, A.; Sztáray, B., Photoelectron-Photoion Coincidence Methods in Mass Spectrometry (PEPICO). In *Encyclopedia of Spectroscopy and Spectrometry*, Lindon, J.; Tranter, G. E.; Koppenaal, D., Eds. Academic Press: Oxford, 2017; Vol. 3rd Edition, pp 635–649.
43. Osborn, D. L.; Zou, P.; Johnsen, H.; Hayden, C. C.; Taatjes, C. A.; Knyazev, V. D.; North, S. W.; Peterka, D. S.; Ahmed, M.; Leone, S. R., The Multiplexed Chemical Kinetic Photoionization Mass Spectrometer: A New Approach to Isomer-Resolved Chemical Kinetics. *Rev. Sci. Instrum.* **2008**, *79*, 104103.
44. Taatjes, C. A.; Hansen, N.; Osborn, D. L.; Kohse-Höinghaus, K.; Cool, T. A.; Westmoreland, P. R., "Imaging" Combustion Chemistry via Multiplexed Synchrotron-Photoionization Mass Spectrometry. *Phys. Chem. Chem. Phys.* **2008**, *10*, 20–34.
45. Greenwald, E. E.; Ghosh, B.; Anderson, K. C.; Dooley, K. S.; Zou, P.; Selby, T.; Osborn, D. L.; Meloni, G.; Taatjes, C. A.; Goulay, F., *et al.*, Isomer-Selective Study of the OH Initiated Oxidation of Isoprene in the Presence of O_2 and NO. I. The Minor Inner OH-Addition Channel. *J. Phys. Chem. A* **2010**, *114*, 904–912.
46. Taatjes, C. A.; Meloni, G.; Selby, T. M.; Trevitt, A. J.; Osborn, D. L.; Percival, C. J.; Shallcross, D. E., Direct Observation of the Gas-Phase Criegee Intermediate (CH_2OO). *J. Am. Chem. Soc.* **2008**, *130*, 11883–11885.
47. Welz, O.; Savee, J. D.; Osborn, D. L.; Vasu, S. S.; Percival, C. J.; Shallcross, D. E.; Taatjes, C. A., Direct Kinetic Measurements of Criegee Intermediate (CH_2OO) Formed by Reaction of CH_2I with O_2. *Science* **2012**, *335*, 204–207.
48. Trevitt, A. J.; Goulay, F.; Meloni, G.; Osborn, D. L.; Taatjes, C. A.; Leone, S. R., Isomer-Specific Product Detection of CN Radical Reactions with Ethene and Propene by Tunable VUV Photoionization Mass Spectrometry. *Int. J. Mass Spectrom.* **2009**, *280*, 113–118.
49. Sztáray, B.; Voronova, K.; Torma, K. G.; Covert, K. J.; Bodi, A.; Hemberger, P.; Gerber, T.; Osborn, D. L., CRF-PEPICO: Double Velocity Map Imaging Photoelectron Photoion Coincidence Spectroscopy for Reaction Kinetics Studies. *J. Chem. Phys.* **2017**, *147*, 013944.
50. Schleier, D.; Constantinidis, P.; Faßheber, N.; Fischer, I.; Friedrichs, G.; Hemberger, P.; Reusch, E.; Sztáray, B.; Voronova, K., Kinetics of the a-C_3H_5 + O_2 Reaction, Investigated by

Photoionization Using Synchrotron Radiation. *Phys. Chem. Chem. Phys.* **2018**, *20*, 10721–10731.

51. Voronova, K.; Ervin, K. M.; Torma, K. G.; Hemberger, P.; Bodi, A.; Gerber, T.; Osborn, D. L.; Sztáray, B., Radical Thermometers, Thermochemistry, and Photoelectron Spectra: A Photoelectron Photoion Coincidence Spectroscopy Study of the Methyl Peroxy Radical. *J. Phys. Chem. Lett.* **2018**, *9*, 534–539.
52. Hinshelwood, C. N., On the Theory of Unimolecular Reactions. *Proc. R. Soc. Lond. A* **1926**, *3*, 230–233.
53. William, A. C., Effect of Unimolecular Decay Kinetics on the Interpretation of Appearance Potentials. *J. Chem. Phys.* **1959**, *30*, 191–211.
54. Lifshitz, C., Kinetic Shifts. *Eur. J. Mass Spectrom.* **2002**, *8*, 85–98.
55. Dunbar, R. C.; Chen, J. H.; So, H. Y.; Asamoto, B., Infrared Fluorescence Relaxation of Photoexcited Gas-Phase Ions by Chopped-Laser Two-Photon Dissociation. *J. Chem. Phys.* **1987**, *86*, 2081–2086.
56. Asamoto, B.; Dunbar, R. C., Observation of the Infrared Radiative Relaxation of Iodobenzene Ions Using Two-Light-Pulse Photodissociation. *J. Phys. Chem.* **1987**, *91*, 2804–2807.
57. Sztáray, B.; Baer, T., Dissociation Dynamics and Thermochemistry of Energy-Selected $CpCo(CO)_2^+$ Ions. *J. Am. Chem. Soc.* **2000**, *122*, 9219–9226.
58. Rodgers, M. T.; Armentrout, P. B., Statistical Modeling of Competitive Threshold Collision-Induced Dissociation. *J. Chem. Phys.* **1998**, *109*, 1787–1800.
59. Rice, O. K.; Ramsperger, H. C., Theories of Unimolecular Gas Reactions at Low Pressures. *J. Am. Chem. Soc.* **1927**, *49*, 1617–1629.
60. Rice, O. K.; Ramsperger, H. C., Theories of Unimolecular Gas Reactions at Low Pressures. II. *J. Am. Chem. Soc.* **1928**, *50*, 617–620.
61. Kassel, L. S., Studies in Homogeneous Gas Reactions. I. *J. Phys. Chem.* **1928**, *32*, 225–242.
62. Weston Jr, R. E., A Comparison of Various Methods for Calculating Unimolecular Reaction Rate Constants. *Int. J. Chem. Kinet.* **1986**, *18*, 1259–1276.
63. Marcus, R. A.; Rice, O. K., The Kinetics of the Recombination of Methyl Radicals and Iodine Atoms. *J. Phys. Chem.* **1951**, *55*, 894–908.
64. Rosenstock, H. M.; Wallenstein, M. B.; Wahrhaftig, A. L.; Eyring, H., Absolute Rate Theory for Isolated Systems and the Mass Spectra of Polyatomic Molecules. *Proc. Natl. Acad. Sci. U.S.A* **1952**, *38*, 667.
65. Robinson, P. J.; Holbrook, K. A., *Unimolecular reactions*. Wiley-Interscience: London, 1972; p 371.
66. Garrett, B. C.; Truhlar, D. G., Improved Canonical Variational Theory for Chemical Reaction Rates. Classical Mechanical Theory and Applications to Collinear Reactions. *J. Phys. Chem.* **1980**, *84*, 805–812.
67. Miller, W. H., Importance of Nonseparability in Quantum Mechanical Transition-State Theory. *Acc. Chem. Res.* **1976**, *9*, 306–312.
68. Troe, J., Theory of Thermal Unimolecular Reactions at High Pressures. *J. Chem. Phys.* **1981**, *75*, 226–237.
69. Brouwer, L.; Cobos, C. J.; Troe, J.; Dübal, H. R.; Crim, F. F., Specific Rate Constants $k(E,J)$ and Product State Distributions in Simple Bond Fission Reactions. II. Application to $HOOH \rightarrow OH + OH$. *J. Chem. Phys.* **1987**, *86*, 6171–6182.
70. Light, J. C., Phase-Space Theory of Chemical Kinetics. *J. Chem. Phys.* **1964**, *40*, 3221–3229.

71. Pechukas, P.; Light, J. C., On Detailed Balancing and Statistical Theories of Chemical Kinetics. *J. Chem. Phys.* **1965**, *42*, 3281–3291.
72. Nikitin, E. E., Statistical Theory of Endothermic Reactions. *Theor. Exp. Chem.* **1965**, *1*, 90-94.
73. Troe, J., Specific Rigidity Factors in Simple Unimolecular Bond Fission Reactions. *J. Chem. Soc., Faraday Trans.* **1997**, *93*, 885–891.
74. Lifshitz, C., Time-resolved Appearance Energies, Breakdown Graphs, and Mass Spectra: The Elusive "Kinetic Shift". *Mass Spectrom. Rev.* **1982**, *1*, 309–348.
75. Sztáray, B.; Baer, T., Consecutive and Parallel Dissociation of Energy-Selected $Co(CO)_3NO^+$ Ions. *J. Phys. Chem. A* **2002**, *106*, 8046–8053.
76. Klots, C. E., Reformulation of the Quasiequilibrium Theory of Ionic Fragmentation. *J. Phys. Chem.* **1971**, *75*, 1526–1532.
77. Klots, C. E., Quasi-Equilibrium Theory of Ionic Fragmentation: Further Considerations. *Z. Naturforsch. A* **1972**, *27*, 553–561.
78. Li, Y.; Sztáray, B.; Baer, T., Dissociation Kinetics of Energy-Selected Cp_2Mn^+ Ions Studied by Threshold Photoelectron-Photoion Coincidence Spectroscopy. *J. Am. Chem. Soc.* **2002**, *124*, 5843–5849.
79. Nelder, J. A.; Mead, R., A Simplex Method for Function Minimization. *Comp. J.* **1965**, *7*, 308–313.
80. Jensen, F., *Introduction to Computational Chemistry*. 2nd ed.; John Wiley & Sons, Ltd: Chichester, West Sussex, England, 2007; p 620.
81. Martin, J. M. L.; de Oliveira, G., Towards Standard Methods for Benchmark Quality Ab Initio Thermochemistry—W1 and W2 Theory. *J. Chem. Phys.* **1999**, *111*, 1843–1856.
82. Howe, I.; McLafferty, F. W., Unimolecular Decomposition of Toluene and Cycloheptatriene Molecular Ions. Variation of the Degree of Scrambling and Isotope Effect with Internal Energy. *J. Am. Chem. Soc.* **1971**, *93*, 99–105.
83. McLafferty, F. W.; Winkler, J., Metastable Ion Characteristics. XXXI. Gaseous Tropylium, Benzyl, Tolyl, and Norbornadienyl Cations. *J. Am. Chem. Soc.* **1974**, *96*, 5182–5189.
84. Stebbings, W. L.; Taylor, J. W., Photoionization Mass Spectrometry. II. Contrasting Fragmentation of Toluene by Photons and by Electrons. *Int. J. Mass Spectrom. Ion Phys.* **1972**, *9*, 471–484.
85. Traeger, J. C.; McLoughlin, R. G., Threshold Photoionization and Dissociation of Toluene and Cycloheptatriene. *J. Am. Chem. Soc.* **1977**, *99*, 7351–7352.
86. Lin, C. Y.; Dunbar, R. C., Time-Resolved Photodissociation Rates and Kinetic Modeling for Unimolecular Dissociations of Iodotoluene Ions. *J. Phys. Chem.* **1994**, *98*, 1369–1375.
87. Huang, F.-S.; Dunbar, R. C., Time-Resolved Photodissociation of Toluene Ion. *Int. J. Mass Spectrom. Ion Proc.* **1991**, *109*, 151–170.
88. Wagner, J. P.; McDonald, D. C., II; Duncan, M. A., Mid-Infrared Spectroscopy of $C_7H_7^+$ Isomers in the Gas Phase: Benzylium and Tropylium. *J. Phys. Chem. Lett.* **2018**, *9*, 4591–4595.
89. Olesik, S.; Baer, T.; Morrow, J. C.; Ridal, J. J.; Buschek, J. M.; Holmes, J. L., Dissociation Dynamics of Halotoluene Ions. Production of Tolyl, Benzyl and Tropylium ($[C_7H_7]^+$) Ions. *Org. Mass Spectrom.* **1989**, *24*, 1008–1016.
90. Bombach, R.; Dannacher, J.; Stadelmann, J.-P., Energy and Time Dependence of the Decay Processes of Toluene Molecular Cations. *J. Am. Chem. Soc.* **1983**, *105*, 4205–4211.
91. Hückel, E., Quantentheoretische Beiträge zum Benzolproblem. *Z. Physik* **1931**, *70*, 204–286.

92. Doering, W. v. E.; Knox, L. H., The Cycloheptatrienylium (Tropylium) Ion. *J. Am. Chem. Soc.* **1954**, *76*, 3203–3206.

93. Stakhursky, V. L.; Sioutis, I.; Tarczay , G.; Miller, T. A., Computational Investigation of the Jahn-Teller Effect in the Ground and Excited Electronic States of the Tropyl Radical. Part I. Theoretical Calculation of Spectroscopically Observable Parameters. *J. Chem. Phys.* **2008**, *128*, 084310.

94. Sioutis, I.; Stakhursky, V. L.; Tarczay , G.; Miller, T. A., Experimental Investigation of the Jahn-Teller Effect in the Ground and Excited Electronic States of the Tropyl Radical. Part II. Vibrational Analysis of the $\tilde{A}^2E_3''$-$\tilde{X}^2E_2''$ Electronic Transition. *J. Chem. Phys.* **2008**, *128*, 084311.

95. Fischer, K. H.; Hemberger, P.; Bodi, A.; Fischer, I., Photoionisation of the Tropyl Radical. *Beilstein J. Org. Chem.* **2013**, *9*, 681–688.

96. Lifshitz, C., Tropylium Ion Formation from Toluene: Solution of an Old Problem in Organic Mass Spectrometry. *Acc. Chem. Res.* **1994**, *27*, 138–144.

97. Lifshitz, C.; Gotkis, Y.; Ioffe, A.; Laskin, J.; Shaik, S., Is the Tropylium Ion (Tr^+) Formed from Toluene at Its Thermochemical Threshold? *Int. J. Mass Spectrom. Ion Proc.* **1993**, *125*, R7–R11.

98. Zins, E.-L.; Pepe, C.; Schröder, D., Methylene-Transfer Reactions of Benzylium/Tropylium Ions with Neutral Toluene Studied by Means of Ion-trap Mass Spectrometry. *Faraday Discuss.* **2010**, *145*, 157–169.

99. Fridgen, T. D.; Troe, J.; Viggiano, A. A.; Midey, A. J.; Williams, S.; McMahon, T. B., Experimental and Theoretical Studies of the Benzylium$^+$/Tropylium$^+$ Ratios after Charge Transfer to Ethylbenzene. *J. Phys. Chem. A* **2004**, *108*, 5600–5609.

100. Bullins, K. W.; Huang, T. T. S.; Kirkby, S. J., Theoretical Investigation of the Formation of the Tropylium Ion From the Toluene Radical Cation. *Int. J. Quantum. Chem.* **2009**, *109*, 1322–1327.

101. Smith, B. J.; Hall, N. E., G2(MP2, SVP) Study of the Relationship Between the Benzyl and Tropyl Radicals, and Their Cation Analogues. *Chem. Phys. Lett.* **1997**, *279*, 165–171.

102. Ignatyev, I. S.; Sundius, T., Competitive Ring Hydride Shifts and Tolyl-Benzyl Rearrangements in Tolyl and Silatolyl Cations. *Chem. Phys. Lett.* **2000**, *326*, 101–108.

103. Nagy, A.; Fulara, J.; Garkusha, I.; Maier, J. P., On the Benzylium/Tropylium Ion Dichotomy: Electronic Absorption Spectra in Neon Matrices. *Angew. Chem. Int. Ed.* **2011**, *50*, 3022–3025.

104. Rylander, P. N.; Meyerson, S.; Grubb, H. M., Organic Ions in the Gas Phase. II. The Tropylium Ion. *J. Am. Chem. Soc.* **1957**, *79*, 842–846.

105. Meyerson, S.; Rylander, P. N., Organic Ions in the Gas Phase. IV. $C_7H_7^+$ and $C_5H_5^+$ Ions from Alkylbenzenes and Cycloheptatriene. *J. Chem. Phys.* **1957**, *27*, 901–904.

106. Meyerson, S.; Rylander, P. N., Organic Ions in the Gas Phase. VI. The Dissociation of *p*-Xylene under Electron Impact. *J. Phys. Chem.* **1958**, *62*, 2–5.

107. Tait, J. M. S.; Shannon, T. W.; Harrison, A. G., The Structure of Substituted C_7 Ions from Benzyl Derivatives at the Appearance Potential Threshold. *J. Am. Chem. Soc.* **1962**, *84*, 4–8.

108. Meyerson, S.; McCollum, J. D.; Rylander, P. N., Organic Ions in the Gas Phase. VIII. Bicycloheptadiene. *J. Am. Chem. Soc.* **1961**, *83*, 1401–1403.

109. Hanuš, V., Isomerization to the Tropylium Ion Induced by Electron Impact and its Significance. *Nature* **1959**, *184*, 1796–1796.

110. Dolejšek, Z.; Hanuš, V.; Prinzbach, H., Das massenspektrometrische Verhalten von Quadricyclen. *Angew. Chem.* **1962**, *74*, 902–902.
111. Lifshitz, C.; Bauer, S. H., Mass Spectra of Valence Tautomers. *J. Phys. Chem.* **1963**, *67*, 1629–1635.
112. Meyer, F.; Harrison, A. G., A Mechanism for Tropylium Ion Formation by Electron Impact. *J. Am. Chem. Soc.* **1964**, *86*, 4757-4761.
113. Yamamoto, Y.; Takamuku, S.; Sakurai, H., Structure and reactivity of organic ions in gas-phase radiolysis. I. The $C_7H_7^+$ ion from toluene, ethylbenzene, and m-xylene. *J. Am. Chem. Soc.* **1969**, *91*, 7192-7194.
114. Takamuku, S.; Sagi, N.; Nagaoka, K.; Sakurai, H., Structure and Reactivity of Organic Ions in Gas-phase Radiolysis. VI. Formation Process of the $C_7H_7^+$ Ion from Ethylbenzene and the Reaction with Dimethylamine. *J. Am. Chem. Soc.* **1972**, *94*, 6217–6218.
115. Yamamoto, Y.; Takamuku, S.; Sakurai, H., Structure and Reactivity of Organic Ions in Gas-Phase Radiolysis. V. Structure and Formation Process of the $C_7H_7^+$ Ion from Toluene. *J. Am. Chem. Soc.* **1972**, *94*, 661–663.
116. Choe, J. C., Dissociation of Toluene Cation: A New Potential Energy Surface. *J. Phys. Chem. A* **2006**, *110*, 7655–7662.
117. Sztáray, B.; Bodi, A.; Baer, T., Modeling Unimolecular Reactions in Photoelectron Photoion Coincidence Experiments. *J. Mass Spectrom.* **2010**, *45*, 1233–1245.
118. Voronova, K.; Mozaffari Easter, C. M.; Covert, K. J.; Bodi, A.; Hemberger, P.; Sztáray, B., Dissociative Photoionization of Diethyl Ether. *J. Phys. Chem. A* **2015**, *119*, 10654–10663.
119. Bodi, A.; Johnson, M.; Gerber, T.; Gengeliczki, Z.; Sztáray, B., Imaging Photoelectron Photoion Coincidence Spectroscopy with Velocity Focusing Electron Optics. *Rev. Sci. Instrum.* **2009**, *80*, 034101.
120. Mayer, P. M.; Blanchet, V.; Joblin, C., Threshold Photoelectron Study of Naphthalene, Anthracene, Pyrene, 1,2-Dihydronaphthalene, and 9,10-Dihydroanthracene. *J. Chem. Phys.* **2011**, *134*, 244312.
121. West, B.; Joblin, C.; Blanchet, V.; Bodi, A.; Sztáray, B.; Mayer, P. M., Dynamics of Hydrogen and Methyl Radical Loss from Ionized Dihydro-Polycyclic Aromatic Hydrocarbons: A Tandem Mass Spectrometry and Imaging Photoelectron–Photoion Coincidence (iPEPICO) Study of Dihydronaphthalene and Dihydrophenanthrene. *J. Phys. Chem. A* **2014**, *118*, 1807–1816.
122. West, B.; Joblin, C.; Blanchet, V.; Bodi, A.; Sztáray, B.; Mayer, P. M., On the Dissociation of the Naphthalene Radical Cation: New iPEPICO and Tandem Mass Spectrometry Results. *J. Phys. Chem. A* **2012**, *116*, 10999–11007.
123. Stevens, W.; Sztáray, B.; Shuman, N.; Baer, T.; Troe, J., Specific Rate Constants k(E) of the Dissociation of the Halobenzene Ions: Analysis by Statistical Unimolecular Rate Theories. *J. Phys. Chem. A* **2009**, *113*, 573–582.
124. Johnson, M.; Bodi, A.; Schulz, L.; Gerber, T., Vacuum Ultraviolet Beamline at the Swiss Light Source for Chemical Dynamics Studies. *Nucl. Instrum. Methods Phys. Res. A* **2009**, *610*, 597–603.
125. Wiley, W. C.; McLaren, I. H., Time-of-Flight Mass Spectrometer with Improved Resolution. *Rev. Sci. Instrum.* **1955**, *26*, 1150–1157.
126. Bodi, A.; Brannock, M. D.; Sztáray, B.; Baer, T., Tunneling in H Loss from Energy Selected Ethanol Ions. *Phys. Chem. Chem. Phys.* **2012**, *14*, 16047–16054.

127. Fischer, K. H.; Schneider, M.; Fischer, I.; Pfaffinger, B.; Braunschweig, H.; Sztáray, B.; Bodi, A., Bonding in a Borylene Complex Investigated by Photoionization and Dissociative Photoionization. *Chem. Eur. J.* **2012**, *18*, 4533–4540.
128. Frisch, M. J.; Trucks, G. W.; Schlegel, H. B.; Scuseria, G. E.; Robb, M. A.; Cheeseman, J. R.; Scalmani, G.; Barone, V.; Mennucci, B.; Petersson, G. A., *et al. Gaussian 09*, Gaussian, Inc.: Wallingford, CT, USA, 2009.
129. Peng, C.; Bernhard Schlegel, H., Combining Synchronous Transit and Quasi-Newton Methods to Find Transition States. *Isr. J. Chem.* **1993**, *33*, 449–454.
130. Peng, C.; Ayala, P. Y.; Schlegel, H. B.; Frisch, M. J., Using Redundant Internal Coordinates to Optimize Equilibrium Geometries and Transition States. *J. Comput. Chem.* **1996**, *17*, 49–56.
131. Curtiss, L. A.; Redfern, P. C.; Raghavachari, K., Gaussian-4 Theory. *J. Chem. Phys.* **2007**, *126*, 084108.
132. Ochterski, J. W.; Petersson, G. A.; Montgomery Jr., J. A., A Complete Basis Set Model Chemistry. V. Extensions to Six or More Heavy Atoms. *J. Chem. Phys.* **1996**, *104*, 2598–2619.
133. Montgomery, J. A. J.; Frisch, M. J.; Ochterski, J. W.; Petersson, G. A., A Complete Basis Set Model Chemistry. VI. Use of Density Functional Geometries and Frequencies. *J. Chem. Phys.* **1999**, *110*, 2822–2827.
134. Montgomery, J. A. J.; Frisch, M. J.; Ochterski, J. W.; Petersson, G. A., A Complete Basis Set Model Chemistry. VII. Use of the Minimum Population Localization Method. *J. Chem. Phys.* **2000**, *112*, 6532–6542.
135. Baer, T.; Hase, W. L., *Unimolecular Reaction Dynamics: Theory and Experiments*. Oxford University Press: New York, 1996.
136. Beyer, T.; Swinehart, D. F., Algorith 448: number of multiply-restricted partitions. *Commun. ACM* **1973**, *16*, 379.
137. Pitzer, K. S., *Quantum Chemistry*. Prentice Hall: New York, 1953; p 339.
138. Watanabe, K., Photoionization and Total Absorption Cross Section of Gases. I. Ionization Potentials of Several Molecules. Cross Sections of NH_3 and NO. *J. Chem. Phys.* **1954**, *22*, 1564–1570.
139. Lu, K.-T.; Eiden, G. C.; Weisshaar, J. C., Toluene Cation: Nearly Free Rotation of the Methyl Group. *J. Phys. Chem.* **1992**, *96*, 9742–9748.
140. Pollak, E.; Pechukas, P., Symmetry Numbers, not Statistical Factors, Should Be Used in Absolute Rate Theory and in Broensted Relations. *J. Am. Chem. Soc.* **1978**, *100*, 2984–2991.
141. Hoffman, M. K., Hidden Rearrangements in the Mass Spectral Decomposition of Cycloheptatriene. *Z. Naturforsch.* **1974**, *29a*, 1077–1080.
142. Field, T. A.; Dulieu, F.; Fillion, J.-H.; Chotin, J.-L.; Douin, S.; Lemaire, J.-L.; Leach, S., Fragmentation of Three Isotopic Toluene Monocations in the 15–100 eV Photon Energy Range. *Chem. Phys.* **1999**, *250*, 81–110.
143. Ruscic, B. *Active Thermochemical Tables (ATcT)* values based on ver. 1.112 of the Thermochemical Network. available at ATcT.anl.gov.
144. Baer, T.; Morrow, J. C.; Shao, J. D.; Olesik, S., Gas-Phase Heats of Formation of $C_7H_7^+$ Isomers: *m*-Tolyl, *p*-Tolyl, and Benzyl Ions. *J. Am. Chem. Soc.* **1988**, *110*, 5633–5638.
145. Ellison, G. B.; Davico, G. E.; Bierbaum, V. M.; DePuy, C. H., Thermochemistry of the Benzyl and Allyl Radicals and Ions. *Int. J. Mass Spectrom. Ion Proc.* **1996**, *156*, 109–131.
146. Savee, J. D.; Zádor, J.; Hemberger, P.; Sztáray, B.; Bodi, A.; Osborn, D. L., Threshold Photoelectron Spectrum of the Benzyl Radical. *Mol. Phys.* **2015**, *113*, 2217–2227.

147. Tsang, W., Heats of Formation of Organic Free Radicals by Kinetic Methods. In *Energetics of Organic Free Radicals*, Martinho Simões, J. A.; Greenberg, A.; Liebman, J. F., Eds. Springer Netherlands: Dordrecht, 1996; pp 22–58.

148. Baulch, D. L.; Bowman, C. T.; Cobos, C. J.; Cox, R. A.; Just, T.; Kerr, J. A.; Pilling, M. J.; Stocker, D.; Troe, J.; Tsang, W., *et al.*, Evaluated Kinetic Data for Combustion Modeling: Supplement II. *J. Phys. Chem. Ref. Data* **2005**, *34*, 757–1397.

149. Shuman, N. S.; Bodi, A.; Baer, T., Heats of Formation of *t*-Butyl Peroxy Radical and *t*-Butyl Diazyl Ion: RRKM vs SSACM Rate Theories in Systems with Kinetic and Competitive Shifts. *J. Phys. Chem. A* **2010**, *114*, 232–240.

150. Kohse-Höinghaus, K.; Oßwald, P.; Cool, T. A.; Kasper, T.; Hansen, N.; Qi, F.; Westbrook, C. K.; Westmoreland, P. R., Biofuel Combustion Chemistry: From Ethanol to Biodiesel. *Angew. Chem., Int. Ed.* **2010**, *49*, 3572–3597.

151. Nigam, P. S.; Singh, A., Production of Liquid Biofuels from Renewable Resources. *Prog. Energy Combust. Sci.* **2011**, *37*, 52–68.

152. Harper, M. R.; Van Geem, K. M.; Pyl, S. P.; Marin, G. B.; Green, W. H., Comprehensive Reaction Mechanism for *n*-Butanol Pyrolysis and Combustion. *Combust. Flame* **2011**, *158*, 16–41.

153. Cai, J.; Zhang, L.; Zhang, F.; Wang, Z.; Cheng, Z.; Yuan, W.; Qi, F., Experimental and Kinetic Modeling Study of *n*-Butanol Pyrolysis and Combustion. *Energy Fuels* **2012**, *26*, 5550–5568.

154. Gu, X.; Huang, Z.; Wu, S.; Li, Q., Laminar Burning Velocities and Flame Instabilities of Butanol Isomers–Air Mixtures. *Combust. Flame* **2010**, *157*, 2318–2325.

155. Veloo, P. S.; Egolfopoulos, F. N., Flame Propagation of Butanol Isomers/Air Mixtures. *Proc. Combust. Inst.* **2011**, *33*, 987–993.

156. Black, G.; Curran, H. J.; Pichon, S.; Simmie, J. M.; Zhukov, V., Bio-Butanol: Combustion Properties and Detailed Chemical Kinetic Model. *Combust. Flame* **2010**, *157*, 363–373.

157. Heufer, K. A.; Fernandes, R. X.; Olivier, H.; Beeckmann, J.; Röhl, O.; Peters, N., Shock Tube Investigations of Ignition Delays of *n*-Butanol at Elevated Pressures Between 770 and 1250K. *Proc. Combust. Inst.* **2011**, *33*, 359–366.

158. Stranic, I.; Chase, D. P.; Harmon, J. T.; Yang, S.; Davidson, D. F.; Hanson, R. K., Shock Tube Measurements of Ignition Delay Times for the Butanol Isomers. *Combust. Flame* **2012**, *159*, 516–527.

159. Moss, J. T.; Berkowitz, A. M.; Oehlschlaeger, M. A.; Biet, J.; Warth, V.; Glaude, P.-A.; Battin-Leclerc, F., An Experimental and Kinetic Modeling Study of the Oxidation of the Four Isomers of Butanol. *J. Phys. Chem. A* **2008**, *112*, 10843–10855.

160. Dagaut, P.; Sarathy, S. M.; Thomson, M. J., A Chemical Kinetic Study of *n*-Butanol Oxidation at Elevated Pressure in a Jet Stirred Reactor. *Proc. Combust. Inst.* **2009**, *32*, 229–237.

161. Sarathy, S. M.; Thomson, M. J.; Togbé, C.; Dagaut, P.; Halter, F.; Mounaim-Rousselle, C., An Experimental and Kinetic Modeling Study of *n*-Butanol Combustion. *Combust. Flame* **2009**, *156*, 852–864.

162. Yang, B.; Oßwald, P.; Li, Y.; Wang, J.; Wei, L.; Tian, Z.; Qi, F.; Kohse-Höinghaus, K., Identification of Combustion Intermediates in Isomeric Fuel-Rich Premixed Butanol–Oxygen Flames at Low Pressure. *Combust. Flame* **2007**, *148*, 198–209.

163. Hansen, N.; Harper, M. R.; Green, W. H., High-Temperature Oxidation Chemistry of *n*-Butanol – Experiments in Low-Pressure Premixed Flames and Detailed Kinetic Modeling. *Phys. Chem. Chem. Phys.* **2011**, *13*, 20262–20274.

164. Oßwald, P.; Güldenberg, H.; Kohse-Höinghaus, K.; Yang, B.; Yuan, T.; Qi, F., Combustion of Butanol Isomers – A Detailed Molecular Beam Mass Spectrometry Investigation of Their Flame Chemistry. *Combust. Flame* **2011**, *158*, 2–15.
165. Merchant, S. S.; Zanoelo, E. F.; Speth, R. L.; Harper, M. R.; Van Geem, K. M.; Green, W. H., Combustion and Pyrolysis of *iso*-Butanol: Experimental and Chemical Kinetic Modeling Study. *Combust. Flame* **2013**, *160*, 1907–1929.
166. Sarathy, S. M.; Vranckx, S.; Yasunaga, K.; Mehl, M.; Oßwald, P.; Metcalfe, W. K.; Westbrook, C. K.; Pitz, W. J.; Kohse-Höinghaus, K.; Fernandes, R. X., *et al.*, A Comprehensive Chemical Kinetic Combustion Model for the Four Butanol Isomers. *Combust. Flame* **2012**, *159*, 2028–2055.
167. Bose, D.; Wright, M.; Gökçen, T., Uncertainty and Sensitivity Analysis of Thermochemical Modeling for Titan Atmospheric Entry. *37th AIAA Thermophysics Conference* **2004**.
168. Raman, V.; Hassanaly, M., Emerging Trends in Numerical Simulations of Combustion Systems. *Proc. Combust. Inst.* **2019**, *37*, 2073–2089.
169. Zádor, J.; Zsély, I. G.; Turányi, T.; Ratto, M.; Tarantola, S.; Saltelli, A., Local and Global Uncertainty Analyses of a Methane Flame Model. *J. Phys. Chem. A* **2005**, *109*, 9795–9807.
170. Afeefy, H. Y.; Liebman, J. F.; Stein, S. E., Neutral Thermochemical Data. In *NIST Chemistry WebBook, NIST Standard Reference Database Number 69*, Linstrom, P. J.; Mallard, W. G., Eds. National Institute of Standards and Technology, Gaithersburg MD, 20899, (retrieved August 14, 2019).
171. Wadsö, I., Heats of Vaporization for a Number of Organic Compounds at 25 ºC. *Acta Chemica Scandinavica* **1966**, *20*, 544–552.
172. Pedley, J. B., *Thermochemical Data and Structures of Organic Compounds*. CRC Press: 1994; Vol. 1.
173. Rosenstock, H. M.; Draxl, K.; Steiner, B. W.; Herron, J. T., *Energetics of Gaseous Ions*. National Standard Reference Data System: 1977; p 783.
174. Yaws, C. L., *Yaws' Handbook of Thermodynamic and Physical Properties of Chemical Compounds*. Gulf Publishing Company: 2006; p 776.
175. Connett, J. E., Chemical Equilibria 6. Measurement of Equilibrium Constants for the Dehydrogenation of 2-Methylpropan-1-ol by a Vapour-Flow Technique. *J. Chem. Thermodynam.* **1975**, *7*, 1159–1162.
176. Voronova, K.; Ervin, K. M.; Torma, K. G.; Hemberger, P.; Bodi, A.; Gerber, T.; Osborn, D. L.; Sztáray, B., Radical Thermometers, Thermochemistry, and Photoelectron Spectra: A Photoelectron Photoion Coincidence Spectroscopy Study of the Methyl Peroxy Radical. *J. Phys. Chem. Lett.* **2018**, *9*, 534–539.
177. Covert, K. J.; Voronova, K.; Torma, K. G.; Bodi, A.; Zádor, J.; Sztáray, B., Thermochemistry of the Smallest QOOH Radical from the Roaming Fragmentation of Energy Selected Methyl Hydroperoxide Ions. *Phys. Chem. Chem. Phys.* **2018**, *20*, 21085–21094.
178. Xie, M.; Zhou, Z.; Wang, Z.; Chen, D.; Qi, F., Determination of Absolute Photoionization Cross-Sections of Oxygenated Hydrocarbons. *Int. J. Mass Spectrom.* **2010**, *293*, 28–33.
179. Bowen, R. D.; Maccoll, A., Low Energy, Low Temperature Mass Spectra 2—Low Energy, Low Temperature Mass Spectra of Some Small Saturated Alcohols and Ethers. *Org. Mass Spectrom.* **1984**, *19*, 379–384.
180. Lambdin, W. J.; Tuffly, B. L.; Yarborough, V. A., Appearance Potentials as Obtained with an Analytical Mass Spectrometer. *Appl. Spectrosc.* **1959**, *13*, 71–74.

181. Selim, E. T. M.; Helal, A. I., Heat of Formation of $CH_2=OH^+$ Fragment Ion. *Indian J. Pure Appl. Phys.* **1981**, *19*, 977–982.

182. Benson, S. W., *Thermochemical Kinetics: Methods for the Estimation of Thermochemical Data and Rate Parameters*. 2nd Edition ed.; John Wiley & Sons, Inc.: New York, 1976.

183. Beyer, T.; Swinehart, D. F., AlgorithM 448: Number of Multiply-Restricted Partitions. *Commun. ACM* **1973**, *16*, 379.

184. Li, Y.; Baer, T., Ethylene Glycol Ions Dissociate by Tunneling through an H-Atom Transfer Barrier: A DFT and TPEPICO Study. *J. Phys. Chem. A* **2002**, *106*, 8658–8666.

185. Torma, K. G.; Voronova, K.; Sztáray, B.; Bodi, A., Dissociative Photoionization of the C_7H_8 Isomers Cycloheptatriene and Toluene: Looking at Two Sides of the Same Coin Simultaneously. *J. Phys. Chem. A* **2019**, *123*, 3454–3463.

186. Muller, G.; Voronova, K.; Sztáray, B.; Meloni, G., Rotamers and Migration: Investigating the Dissociative Photoionization of Ethylenediamine. *J. Phys. Chem. A* **2016**, *120*, 3906–3916.

187. Xiao, W.; Hu, Y.; Li, W.; Guan, J.; Liu, F.; Shan, X.; Sheng, L., Unexpected Methyl Migrations of Ethanol Dimer under Synchrotron VUV Radiation. *J. Chem. Phys.* **2015**, *142*, 024306.

188. Dyakov, Y. A.; Ni, C. K.; Lin, S. H.; Lee, Y. T.; Mebel, A. M., *Ab Initio* and RRKM Study of Photodissociation of Azulene Cation. *Phys. Chem. Chem. Phys.* **2006**, *8*, 1404–1415.

189. Jobst, K. J.; Jogee, S.; Bowen, R. D.; Terlouw, J. K., A Mechanistic Study of the Prominent Loss of H_2O from Ionized 2-Hydroxyaminoethanol. *Int. J. Mass Spectrom.* **2011**, *306*, 138–149.

190. Daly, S.; Powis, I.; Tia, M.; Garcia, G. A.; Nahon, L., Dissociative VUV Photoionization of Butanediol Isomers. *Int. J. Mass Spectrom.* **2015**, *376*, 46–53.

191. Holmes, J. L.; Burgers, P. C.; Mollah, Y. A., Alkane Elimination from Ionized Alkanols. *Org. Mass Spectrom.* **1982**, *17*, 127–130.

192. Cocksey, B. J.; Eland, J. H. D.; Danby, C. J., The Effect of Alkyl Substitution on Ionisation Potential. *J. Chem. Soc. B: Phys. Org.* **1971**, 790–792.

193. Watanabe, K.; Nakayama, T.; Mottl, J., Ionization Potentials of Some Molecules. *J. Quant. Spectrosc. Rad. Trans.* **1962**, *2*, 369–382.

194. McLafferty, F. W., Mass Spectrometric Analysis Broad Applicability to Chemical Research. *Anal. Chem.* **1956**, *28*, 306–316.

195. Ruscic, B.; Bross, D. H. *Active Thermochemical Tables (ATcT)* values based on ver. 1.122e of the Thermochemical Network. available at ATcT.anl.gov.

196. Shuman, N. S.; Zhao, L. Y.; Boles, M.; Baer, T.; Sztáray, B., Heats of Formation of $HCCl_3$, $HCCl_2Br$, $HCClBr_2$, $HCBr_3$, and Their Fragment Ions Studied by Threshold Photoelectron Photoion Coincidence. *J. Phys. Chem. A* **2008**, *112*, 10533–10538.

197. Bodi, A.; Kercher, J. P.; Bond, C.; Meteesatien, P.; Sztáray, B.; Baer, T., Photoion Photoelectron Coincidence Spectroscopy of Primary Amines RCH_2NH_2 (R = H, CH_3, C_2H_5, C_3H_7, *i*-C_3H_7): Alkylamine and Alkyl Radical Heats of Formation by Isodesmic Reaction Networks. *J. Phys. Chem. A* **2006**, *110*, 13425–13433.